

ABSTRACT

Title of Dissertation:

TROPOSPHERIC OZONE AND ITS
RADIATIVE EFFECTS DUE TO
ANTHROPOGENIC AND LIGHTNING
EMISSIONS: GLOBAL AND REGIONAL
MODELING

Matus Novak Martini, Doctor of Philosophy,
2012

Directed By:

Drs. Dale J. Allen and Russell R. Dickerson
Department of Atmospheric and Oceanic Science

We analyze the contribution of North American (NA) lightning and anthropogenic emissions to summertime ozone concentrations, radiative forcing, and exports from North America using the global University of Maryland chemistry transport model (UMD-CTM) and the regional scale Weather Research and Forecasting model with chemistry (WRF-Chem). Lightning NO contributes by 15–20 ppbv to upper tropospheric ozone concentrations over the United States with the effects of NA lightning on ozone seen as far east as North Africa and Europe. Using the UMD-CTM, we compare changes in surface and column ozone amounts due to the NO_x State Implementation Plan (SIP) Call with the natural variability in ozone due to changes in meteorology and lightning. Comparing early summer 2004 with 2002, surface ozone decreased by up to 5 ppbv due to the NO_x SIP Call while changes in meteorology and lightning resulted in a 0.3–1.4 ppbv increase in surface

ozone. Ozone column variability was driven primarily by changes in lightning NO emissions, especially over the North Atlantic. As part of our WRF-Chem analysis, we modify the radiation schemes to use model-calculated ozone (interactive ozone) instead of climatological ozone profiles and conduct multiple 4-day simulations of July 2007. We found that interactive ozone increased the outgoing longwave radiation (OLR) by 3 W m^{-2} decreasing the bias with respect to remotely sensed OLR. The improvement is due to a high bias in the climatological ozone profiles. The interactive ozone had a small impact on mean upper troposphere temperature (-0.15°C). The UMD-CTM simulations indicate that NA anthropogenic emissions are responsible for more ozone export but less ozone radiative forcing than lightning NO emissions. Over the North Atlantic, NA anthropogenic emissions contributed $0.15\text{--}0.30 \text{ W m}^{-2}$ to the net downward radiative flux at the tropopause while NA lightning contributed $0.30\text{--}0.50 \text{ W m}^{-2}$. The ozone export from anthropogenic emissions was almost twice as large as that from lightning emissions. The WRF-Chem simulations show that the export of reactive nitrogen was 23%–28% of the boundary layer emissions and 26%–38% of the total emissions including lightning NO.

RADIATIVE EFFECTS DUE TO NORTH AMERICAN ANTHROPOGENIC AND
LIGHTNING EMISSIONS: GLOBAL AND REGIONAL MODELING

By

Matus Novak Martini

Dissertation submitted to the Faculty of the Graduate School of the
University of Maryland, College Park, in partial fulfillment
of the requirements for the degree of
Doctor of Philosophy
2012

Advisory Committee:

Professor Russell R. Dickerson, Co-Chair
Associate Research Scientist, Dale J. Allen, Co-Chair
Adjunct Professor Kenneth E. Pickering, Co-Advisor
Professor Ross J. Salawitch
Professor Robert Hudson
Professor Michael N. Evans

UMI Number: 3557670

All rights reserved

INFORMATION TO ALL USERS

The quality of this reproduction is dependent upon the quality of the copy submitted.

In the unlikely event that the author did not send a complete manuscript and there are missing pages, these will be noted. Also, if material had to be removed, a note will indicate the deletion.



UMI 3557670

Published by ProQuest LLC (2013). Copyright in the Dissertation held by the Author.

Microform Edition © ProQuest LLC.

All rights reserved. This work is protected against unauthorized copying under Title 17, United States Code



ProQuest LLC.
789 East Eisenhower Parkway
P.O. Box 1346
Ann Arbor, MI 48106 - 1346

© Copyright by
Matus Novak Martini
2012

Acknowledgements

I would like to thank my advisors, Dale Allen and Kenneth Pickering, for their support, inspiring ideas, direction, and mentoring. I would also like to thank Ross Salawitch and Tim Carty for their insights and their support from the beginning and also committee members Russ Dickerson, Robert Hudson, and Michael Evans for their great suggestions and guidance.

In addition, I would like to acknowledge Georgiy Stenchikov, Andreas Richter, Edward Hyer, Hugo Berbery, Xin-Zhong Liang, and Eugenia Kalnay for their insightful comments and help. I thank Owen Cooper for the IC(CG ratios prepared by Dennis Boccippio. I also appreciate the helpful comments and revisions of Arlene Fiore. There are also many other individuals I would like to recognize for their support and stimulating discussions: Chris Loughner, Amanda Hansen, Eric Nussbaumer, Barry Baker, Elena Yegorova, Steven Greybush, Dave Kuhl, Debra Baker, Anthony Santorelli, and Edward Nowottnick.

This work was funded under NASA grants NNG04GD32G and NNG06GE01G (Interdisciplinary Science Investigation) and under NASA grant NNG06GB52G from the Tropospheric Chemistry Program. Model simulations were conducted at NCCS at NASA Goddard Space Flight Center. I thank the INTEX-A science team for the aircraft measurements and Anne Thompson for IONS measurements. The NLDN data were collected by Vaisala, Inc. and archived by NASA Marshall Space Flight Center. OTD/LIS data were processed by NASA/Marshall. Support for the Pinnacle State Park measurements program was provided by the New York State Energy Research and Development Authority (NYSERDA)

And finally, I am grateful to all my teachers and mentors, especially those from Slovakia, my family and my wife Amanda, who corrected all my the's and a's, for their love and constant support.

Table of Contents

Acknowledgements.....	ii
Table of Contents	iii
List of Tables	v
List of Figures	vi
1 Introduction.....	1
2 Background	4
2.1 Tropospheric Ozone Production	4
2.2 Upper Tropospheric NO _x and LNO _x – Lessons From INTEX-A Campaign	6
2.3 Radiative Forcing of Tropospheric Ozone.....	8
3 Global Modeling	11
3.1 Introduction.....	11
3.2 Model Description	13
3.2.1 Anthropogenic Emissions	15
3.2.2 Lightning.....	17
3.2.3 Biogenic Emissions.....	23
3.2.4 Biomass Burning.....	25
3.2.5 Radiative Forcing Calculation	26
3.3 Results.....	27
3.3.1 Differences Between Summers 2002 and 2004	27
3.3.2 UMD-CTM Comparison With Observations.....	35
3.3.2.1 Comparison With DC-8 in Situ Measurements During INTEX-A....	35
3.3.2.2 Comparison With IONS Ozone Soundings	40
3.3.2.3 Comparison With SCIAMACHY NO ₂ Columns	42
3.3.2.4 Comparison With Ozone Observations From Ground-Based AQS Sites.....	46
3.3.3 Ozone Enhancements From NA Anthropogenic Emissions and Lightning	48
3.3.4 Import and Export Fluxes	62
3.4 Summary	67
4 Regional Modeling.....	71
4.1 Introduction.....	71
4.2 Model Description	73

4.2.1 Meteorological and Chemical Initial and Boundary Conditions	75
4.2.2 Emissions	79
4.2.3 Lightning.....	79
4.2.4 Radiation Schemes in WRF	87
4.3 Single Column Experiments With the Offline RRTM Longwave Model	90
4.4 WRF-Chem Results	93
4.4.1 Comparison With Surface NO _x and NO _y Measurements at Pinnacle State Park Research Site	94
4.4.2 Comparison With OMI NO ₂ Columns.....	96
4.4.3 Comparison With Ozonesonde Soundings	99
4.4.3.1 Uncertainty Analysis.....	101
4.4.4 Ozone Enhancements From Lightning and Impact on Surface Ozone...	105
4.4.5 Impact on OLR and Radiative Effects	108
4.4.6 Impact on Daily Fields.....	116
4.4.7 Export of Reactive Nitrogen From the Contiguous United States.....	122
4.5 Summary and Conclusions	126
5 Summary and Future Work.....	129
5.1 Summary of Global Modeling With the UMD-CTM	129
5.2 Summary of Regional Modeling With the WRF-Chem	130
5.3 Future Work.....	131
5.3.1 Offline Calculations of Radiative Forcing	131
5.3.2 Short Term Impacts of Interactive Ozone.....	132
5.3.3 Temperature Response of Ozone due to LNO _x in Climate Simulations.	133
5.3.4 Wind Shear Climatology and New Lightning Scheme.....	134
5.3.5 Impact of Boundary Conditions on Surface Layer	134
Acronyms and Abbreviations	136
Bibliography	138

List of Tables

Table 1. The UMD-CTM Simulations With Different Sources of NO _x Emissions....	15
Table 2. The Lightning Sources Used in This Study and Other Studies	22
Table 3. Selected WRF-Chem Configuration Options	74
Table 4. The WRF-Chem Sensitivity Simulations	75
Table 5. Cloud statistics between the simulation with interactive ozone and the standard simulation (noninteractive ozone) at the 90-hour simulation times ...	119
Table 6. NO _y Import and Export Fluxes From the Contiguous United States (Gmol d ⁻¹)	125

List of Figures

Figure 1. Radiative forcing (RF) of climate between 1750 and 2005 as estimated by the IPCC. Estimates of RF are accompanied by both an uncertainty range and a level of scientific understanding (LOSU). The value uncertainties represent the 5 to 95% (90%) confidence range, and are based on available published studies; the LOSU is a subjective measure of structural uncertainty and represents how well understood the underlying processes are [IPCC, 2007].....	10
Figure 2. Surface NO _x emission change from summer 2002 to 2004 at the 2° × 2.5° resolution as represented in the UMD-CTM standard simulations. Negative values indicate ANO _x emission decreases from 2002 to 2004.....	17
Figure 3. Surface temperatures in summer 2002, 2003 and 2004 (from www.ncdc.noaa.gov/oa/climate/research/2004/CMB_prod_us_2004.html). Changes in GEOS-4 CERES temperatures, used in the UMD-CTM simulations, from summer 2002 to 2004 are smaller than the observed temperature changes shown in this figure. The mean GEOS-4 CERES temperature change from summer 2002 to 2004 over the region of high isoprene emissions (28°N–40°N and 74°W–96°W) is −1.5°C. Isoprene emissions used in the UMD-CTM simulations are from summer 2003.	24
Figure 4. Total (IC + CG) lightning flash rates for the summers 2002 (blue) and 2004 (red) over the CONUS derived from the NLDN-observed CG flashes (adjusted by the IC(CG ratios). Flash rates are smoothed with a 7 day moving average.....	30
Figure 5. Convective mass fluxes (mean from the surface to 700 hPa) averaged for (a) 1 June to 17 July 2004 and (c) 18 July to 31 August 2004 and the relative change (%) between 2002 and 2004 averaged for (b) early and (d) late summer. Warm (cold) colors indicate more (less) vertical mixing by convection in 2004 than in 2002. Convective mass fluxes are calculated as the sum of deep convection and shallow convection fields from the GEOS-4 CERES reanalysis.	31
Figure 6. Mean GEOS-4 CERES surface temperatures and winds at ~5.5 km above the local surface for the period of (a) 1 June to 17 July 2004 and (c) 18 July to 31 August 2004 and the differences relative to 2002 for (b) early and (d) late summer.	32
Figure 7. The NLDN-based total (IC + CG) lightning flash rates from (left) 2002 and (right) 2004 over the CONUS during early summer (1 June to 17 July).	

For comparison with the UMD-CTM flash rates for early summer 2004, see
Figure 9 33

Figure 8. Total (IC + CG) lightning flash rates derived from NLDN ground and LIS spaceborne observations over the CONUS (land only) south of 35°N during 2002–2005. CG flash rates detected by the NLDN network (adjusted by the IC(CG ratios) are smoothed spatially (7.5° boxcar) and temporally (98 day window) and averaged for each month (indicated by the asterisks). Monthly LIS observations (LRMTS) were also smoothed with 98 day and 7.5° moving average. 33

Figure 9. Early summer (1 June to 17 July) 2004 model flash rates. (left) Flash rates are adjusted to match OTD/LIS Low Resolution Time Series flash rates in simulation L0. (right) Flash rates are adjusted to match the NLDN-based total IC + CG flash rates over the CONUS (land only) in simulation L1. The NLDN-based model flash rates for early summer 2004 differ slightly from the NLDN-based observed flash rates (right panel in Figure 7) because the scaling is done on a month by month basis while this figure depicts a 1.5 month period (1 June to 17 July). 34

Figure 10. Mean vertical profiles of NO, O₃, CO, HNO₃, NO_x, OH, PAN and NO_y. Measurements from the DC-8 aircraft (blue) are compared to UMD-CTM results from the L0 (black), L1 (red) and L2 (dashed red) simulations. The 1 min average measurements are compared to hourly UMD-CTM output sampled along the flight tracks. NO_y is estimated as the sum of its main oxidation products (NO_x, PAN, and HNO₃). We use here HNO₃ data obtained by science team from California Institute of Technology. Horizontal bars indicate standard deviations on the observations in each 50-hPa bin. The number of filtered observations above 500 hPa is listed in the upper-right corner of each plot. The absolute values of the bias (model minus observation) averaged from 50-hPa bins above 500 hPa are listed in the middle right part of each plot: L0 bias (top value), L1 bias (center value), and L2 bias (bottom value). Note the logarithmic scale for NO and NO_x. 39

Figure 11. Mean profiles as observed from IONS ozonesondes (blue) and simulated with the UMD-CTM for July and August 2004. Results from the standard simulation (L1: red) and the simulation with doubled lightning NO per flash (L2: red dashed) UMD-CTM simulations are shown. Horizontal bars indicate standard deviations in each 50-hPa bin. The explained variances (r^2) between observed and simulated O₃ from one sounding to the next and the absolute values of the bias (model minus observation) averaged from 50-hPa bins above 500 hPa are listed in the bottom right corner of each plot. 41

Figure 12. Comparison between (a, b) SCIAMACHY-retrieved and (d, e) UMD-CTM-simulated mean tropospheric NO₂ vertical columns (10^{15} molecules

$\text{NO}_2 \text{ cm}^{-2}$) composited from all overpasses with cloud fraction < 0.3 over the eastern United States in (left) August 2002 and (middle) August 2004. The UMD-CTM is sampled at each SCIAMACHY pixel. Both observed (Figures 12a and 12b) and modeled (Figures 12d and 11e) columns are composited to a $0.54^\circ \times 0.70^\circ$ (about $60 \times 60 \text{ km}^2$) grid which is close to the native resolution of SCIAMACHY. In the ORV region (indicated by the larger box on the left), SCIAMACHY observed reduction from 4.27 to 3.32 on average between 2002 and 2004, whereas simulated columns were reduced from 4.24 to 3.43 (all values in units of $10^{15} \text{ NO}_2 \text{ molecules cm}^{-2}$). (c, f) Relative change (%) between 2002 and 2004 but at the $2^\circ \times 2.5^\circ$ resolution..... 45

Figure 13. The 8 h O_3 time series constructed from 155 AQS sites located in the ORV region (indicated by the larger box in Figure 12a) in summer (left) 2002 and (right) 2004. The shaded area around the mean AQS-measured values (red and blue solid lines) indicates the standard deviation. The number of current NAAQS exceedances ($8 \text{ h } \text{O}_3 > 75 \text{ ppbv}$) for each month is in the top right corner of each plot. The UMD-CTM (dotted lines) is sampled at the locations of the AQS sites. The 8 h O_3 from the sensitivity simulation with the anthropogenic emissions from North America turned off (Table 1) is indicated by black dotted lines. The UMD-CTM bias is listed in the bottom left corner of each plot. The explained variance r^2 between time series of observed and simulated O_3 is in the bottom right corner of each plot. 48

Figure 14. Early summer (1 June to 17 July) O_3 enhancements from North American (a, d) anthropogenic and (b, e) lightning emissions as diagnosed by simulation L1 and the sensitivity simulations with the respective sources turned off (Table 1). (c, f) Difference between 2004 and 2002 due to North American lightning. The values are averaged in (top) the lower troposphere (from the surface to 800 hPa) and (bottom) the upper troposphere (400–200 hPa). Minima, averages and maxima are listed in the title of each plot. 56

Figure 15. (a, d) Tropospheric O_3 columns and their enhancements due to North American (b, e) anthropogenic emissions and (c, f) lightning as diagnosed by simulation L1 and the sensitivity simulations with respective sources turned off (Table 1). The values are (top) early summer (1 June to 17 July) mean, and (bottom) late summer (18 July to 31 August) mean for 2004. Minima, averages and maxima are listed in the title of each plot. Corresponding NO_2 columns are in Figures 18a–17c and 18e–18g. 57

Figure 16. (left) The impact of changes (2004 minus 2002 difference) in North American lightning and meteorology and (right) the impact of NO_x SIP Call reductions on tropospheric O_3 columns as diagnosed by simulation L1 and three sensitivity simulations (Table 1), two with the LNO_x source turned off (one for each year) and one with 2002 power plant NO_x emissions and 2004 flash rates and meteorology. The values are (top) early summer (1 June to

17 July) mean and (bottom) late summer (18 July to 31 August) mean.
Minima, averages and maxima are listed in the title of each plot..... 58

Figure 17. (left) The impact of changes (2004 minus 2002) in North American lightning and meteorology and (right) the impact of NO_x SIP Call reductions on surface layer O₃ concentration. The increase in left figure is diagnosed by simulation L1 and two sensitivity simulations with the LNO_x source turned off (Table 1). The decrease in right figure is diagnosed by simulation L1 and sensitivity simulation with 2002 power plant NO_x emissions and 2004 flash rates and meteorology (Table 1). The values are averaged for early summer (1 June to 17 July) at 18 UTC..... 59

Figure 18. (a, e) Tropospheric NO₂ columns and their enhancements due to North American (b, f) anthropogenic emissions and (c, g) lightning as diagnosed by simulation L1 and the sensitivity simulations with respective sources turned off (Table 1) for 2004. (d, h) Difference between 2004 and 2002 due to North American lightning. The values are averages for (top) early summer (1 June to 17 July), and (bottom) late summer (18 July to 31 August). Minima, averages and maxima are listed in the title of each plot..... 60

Figure 19. RF (calculated as described in section 3.2.5) for 2004 due to North American (a, d) anthropogenic emissions and (b, e) lightning as diagnosed by simulation L1 and the sensitivity simulations with respective sources turned off (Table 1). (c, f) Difference between 2004 and 2002 due to North American lightning. The values are (top) early summer (1 June to 17 July) mean and (bottom) late summer (18 July to 31 August) mean. Minima, averages and maxima are listed in the title of each plot. Note a factor of 10 smaller units for RF in Figures 19c and 19f. 61

Figure 20. Early summer 2004 (1 June to 17 July) ratio RF_{LNO_x}/RF_{anthro} as diagnosed by the standard simulation and sensitivity simulations with respective sources turned off (Table 1)..... 62

Figure 21. Early summer (1 June to 17 July) fluxes of NO_x, NO_y, CO and O₃ across the western and eastern boundaries of North America (summed between 25°N and 60°N) at 130°W (imports) and 65°W (exports) from simulation L1 for (a) 2004 exports (red solid), 2004 imports (red dashed), 2002 exports (blue solid) and 2002 imports (blue dashed) and (b) 2004 (red) and 2002 (blue) net exports. Vertically averaged fluxes (from the surface to 100 hPa) are listed in the bottom right corner of each plot. Fluxes across the northern and southern boundaries of North America are small and are not shown. 66

Figure 22. Same as Figure 21 except that exports due to North American anthropogenic (solid) and lightning (dashed) emissions are shown as diagnosed by sensitivity simulations with respective sources turned off (Table 1). Exports in 2004 are red and exports in 2002 are blue. 67

Figure 23. 6 hour precipitation totals ending (top) July 7, 2007 18 UTC and (bottom) July 8, 2007 06 UTC as (left) observed by radar and rain gauges (NCEP Stage IV), (middle) predicted by WRF driven by NARR and (right) predicted by WRF driven by MERRA. Radars operated by National Weather Service have an observation range of 460 km, so Stage IV data does not include rain over oceans beyond this range, although the WRF simulations do..... 78

Figure 24. (a) Mean flash rate distribution during July 2007 as estimated by multiplying the NLDN CG flash rate by $Z + 1$, where Z is the smoothed climatological IC(CG) ratio. (b) Convective precipitation (3 hour totals) as predicted by WRF. Model flash rate (c) based on look up table [Hansen, 2012] and (d) based on convective precipitation [Allen et al., 2012]. Model flash rates in Figures 24c and 24d are scaled so the monthly sum over the CONUS matches the NLDN-based sum in Figure 24b. All flash rates are in units of flash s^{-1} per 36-km grid box. Detection efficiency for NLDN observed flashes falls off rapidly with distance from coast. Therefore NLDN flash rates do not represent actual flash rates for locations with distance > 300 km from the coast. Model flash rates outside of the CONUS are decreased by a factor $f = \exp(-d / 1000)$, where d is the distance from the coast in km..... 84

Figure 25. Same as Figures 24a, 24c and 24d except the histogram depicting the distributions of 1 h flash rates over the CONUS is shown. The histogram of NLDN-based total flash rates is indicated by the blue shaded area, histogram of model flash rates based on Hansen [2012] is the blue line and histogram of model flash rates based on Allen et al. [2012] is the red line..... 85

Figure 26. Time series of daily flash rates summed over the continental United States (land only) during July 2007. NLDN-based estimate obtained by multiplying NLDN CG flash rate by $Z + 1$, where Z is the smoothed climatological IC(CG) ratio, depicted by black line. Model flash rates based on convective precipitation [Allen et al., 2012] (red) and model flash rate based on convective precipitation and mixed phase depth [Hansen, 2012] (blue) are both scaled to match total monthly NLDN (IC + CG) flash rate. Correlation between time series of observed and model flash rates (r) is top right..... 85

Figure 27. (a) Vertical distribution of lightning NO production (mass-like units) assumed in WRF-Chem simulations for locations with the height of -15°C isotherm (Z_{-15}) greater (red) and less (blue) than 6.7 km. These profiles were derived from the vertical distribution of VHF sources in the vicinity of the North Alabama lightning mapping array during the summers 2006 and 2007. Plus signs indicate the centers of the WRF-Chem layers. (b) Spatial mask for grid points with mean $Z_{-15} > 6.7$ km (red) and with $Z_{-15} < 6.7$ km (blue). (c) The histogram depicting the distribution of WRF-calculated Z_{-15} per 0.1 km bin over the modeling domain during July 2007 constructed from

the grid boxes with deep convection. Corresponding parts of the distribution are color-coded.....	86
Figure 28. Mean vertical distribution of ozone during July 2007 averaged over the eastern two-thirds of the United States (110°W – 70°W , 25°N – 45°N) as calculated by WRF-Chem (solid blue) LNO _x simulation (Table 4). Mean profile from the sensitivity simulation with no LNO _x source averaged over the same area and time period is shown in black, and lightning enhancement is indicated by blue shaded area. Standard midlatitude summer (red), standard midlatitude winter (brown) and standard tropical (green) vertical profiles assumed in radiation schemes are shown as dashed lines. Please see text in section 4.2.4 for more details regarding these profiles.....	89
Figure 29. (a) Longwave radiative heating rates for the $9.6\ \mu\text{m}$ ozone band (980 – $1080\ \text{cm}^{-1}$), and (b) radiative heating rate sensitivity to changes in vertical ozone distribution for the standard midlatitude summer (green) and tropical (brown) ozone profiles from Figure 28. For vertical sensitivity in Figure 29b, 40-ppbv ozone increments were added to each atmospheric layer (layer centers are indicated by plus signs in the right panel), and the peak increase in heating rate (from the $9.6\ \mu\text{m}$ ozone band) is then normalized to 1 Dobson unit ozone increment.....	92
Figure 30. Mean (a, c) NO _x and (b, d) O ₃ concentrations over the CONUS from standard simulation LNO _x (Table 4) averaged from 2 July to 30 July, 2007 at (top) 300 hPa and (bottom) surface. The average and the mean standard deviation (σ) of hourly time series over the eastern two thirds of the United States are indicated in the title of each plot.....	94
Figure 31. Time series of 1 h NO _y and NO _x as observed at Pinnacle State Park, New York, research site (blue line) and simulated with the WRF-Chem (red line) for July 2007. Measurements of NO _x between 19 and 24 July are missing. Missing data between 9 and 10 July are due to failure of air conditioning in the instrument unit.....	95
Figure 32. Mean tropospheric NO ₂ column from 2 July to 30 July, 2007. (a) The mean version 2.0 DOMINO column on $0.5^{\circ} \times 0.5^{\circ}$ grid, (b) the mean WRF-Chem tropospheric column from the standard simulation LNO _x on the native 36-km grid. The mean WRF-Chem tropospheric column from the (c) standard LNO _x and (d) low LNO _x simulation on the $0.5^{\circ} \times 0.5^{\circ}$ grid after processing by the OMI averaging kernel.....	99
Figure 33. Mean profiles as observed from ozonesondes (blue) and simulated with WRF-Chem at (left) Beltsville, Maryland (left), Huntsville, Alabama (middle) and Wallops Island, Virginia (right) during July 2007. WRF-Chem simulation noL (LNO _x) is shown in black (red). Horizontal bars around the mean ozonesonde-measured values indicate standard deviations (σ) in each model layer for Beltsville and in each 50-hPa bin for Huntsville and	

Wallops. Numbers in the lower right corner show the number of soundings available, the lightning NO contribution to upper tropospheric (500–200 hPa) ozone (LO_3), the upper tropospheric absolute values of the bias (model minus measurement), and the mean measured upper tropospheric ozone.....	104
Figure 34. Decrease in anthropogenic NO_x emissions from the United States between summer 2005 and 2007 as derived from OMI observations of NO_2 columns and using the GEOS-Chem model [Lamsal <i>et al.</i> , 2011].....	105
Figure 35. Mean ozone enhancements at 300 hPa for July 2007 from LNO_x source as diagnosed by (left) global GMI-CTM over the North America and downwind and as diagnosed by (right) WRF-Chem over the United States and western North Atlantic. GMI-CTM provided initial and boundary conditions of longer-lived trace gases for WRF-Chem simulations.....	107
Figure 36. Increase in 8 h O_3 due to LNO_x averaged over July 2007 at surface as diagnosed from the difference between standard LNO_x simulation and sensitivity simulation with LNO_x source turned off.....	108
Figure 37. (a) Mean OLR over the United States from 2 July to 30 July, 2007 observed by the NOAA-18 satellite and (b) WRF-Chem standard simulation with noninteractive ozone (Table 4). (c) Difference between the WRF-Chem standard simulation with noninteractive ozone (NIO) and NOAA-18 OLR mapped at $2.5^\circ \times 2.5^\circ$ resolution. (d) Difference between the WRF-Chem standard simulation with interactive ozone (IO) and NOAA-18 OLR mapped at $2.5^\circ \times 2.5^\circ$ resolution. The value in the title of each plot is the average from the eastern two thirds of the United States indicated by the black box in Figure 37a.....	113
Figure 38. Same as Figure 37 except the impact of interactive O_3 on the OLR (the difference between simulation with and without interactive ozone) is shown.....	114
Figure 39. Comparison between (a) MODIS-retrieved and (b) WRF-calculated mean high-cloud frequency (the number of days with cloud top pressure < 440 hPa during the period 2 July to 30 July, 2007) constructed from all Aqua daytime overpasses over the CONUS. WRF is sampled at each MODIS pixel. Observed tops are composited onto a 0.3905° longitude \times 0.3237° latitude grid, which is close to the native resolution of WRF ($36 \times 36 \text{ km}^2$). Each grid box in Figure 38a includes on average 19 level 2 MODIS pixels. The value in the title of each plot is the mean over the eastern two thirds of the CONUS (indicated by the box).....	114
Figure 40. Difference between predicted OLR from WRF-Chem simulation with interactive O_3 and from WRF-Chem simulation with climatological O_3 in longwave radiation scheme. The values are averaged between 2 July and 30	

July, 2007 for (a) all sky and (b) clear sky conditions and smoothed spatially (360-km boxcar). The mean value over the eastern two thirds of the United States (indicated by the box in Figure 39a) for each plot is top right... 115

Figure 41. Same as Figure 39 except OLR change due to O₃ produced from LNO_x is shown (the difference between LNO_x-IO simulation and noL-IO simulation) 115

Figure 42. The impact of (a) interactive ozone and (b) ozone due to LNO_x on temperature at 200 hPa for early afternoon (17 UTC) averaged from 29 daily values between 2 July to 30 July 2007. The average and the mean standard deviation (σ) of daily time series at each grid box averaged over the eastern two thirds of the United States (depicted by the box) is top right. 116

Figure 43. The impact of interactive ozone on OLR (the difference between the simulations with and without interactive ozone) after a 42-hour simulation on July 17 (top left), July 20 (top right), July 23 (bottom left), and July 26 (bottom right). The average and the standard deviation from the eastern two thirds of the United States (depicted by the box) are above. 120

Figure 44. Same as Figure 42 except after a 90-hour simulation on July 19 (top left), July 22 (top right), July 25 (bottom left), and July 28 (bottom right) are shown. 120

Figure 45. The impact of interactive ozone on temperature at 200 hPa (the difference between the simulations with and without interactive ozone) after a 90-hour simulation on July 17 (top left), July 20 (top right), July 23 (bottom left), and July 26 (bottom right). The average and the standard deviation from the eastern two thirds of the United States (depicted by the box) are above. 121

Figure 46. Same as Figure 44 except interactive ozone is only included in the longwave radiation scheme, whereas Figure 44 shows the impact of interactive ozone from both longwave and shortwave radiation. 121

Figure 47. Same as Figure 44 except the impact of ozone due to LNO_x is shown... 122

Figure 48. Vertical cross section of NO_y fluxes across the eastern boundary of the contiguous United States (the boundary follows the United States coast and is located 250 km east of the coastline) as a function of latitude during July 2007. Fluxes from the simulation without LNO_x source are shown on the left, fluxes from the simulation with LNO_x source are shown on the right. Positive values indicate eastward fluxes. 125

1 Introduction

North America is a major source of anthropogenic and naturally-generated trace gases, and North American (NA) emissions affect trace gas mixing ratios over the North Atlantic, Europe and North Africa [Li *et al.*, 2002]. A key trace gas for both chemistry and radiative balance of the troposphere is ozone (O_3). According to IPCC [2007], tropospheric O_3 is the third most important climate gas. Major precursors of tropospheric O_3 are nitrogen oxides ($NO_x = NO + NO_2$) from fuel combustion, soils and lightning. Surface precursors are rapidly transported upward via convection [Dickerson *et al.*, 1987; Pickering *et al.*, 1992, 1995] and detrained into the upper troposphere [Bertram *et al.*, 2007] where concurrent lightning greatly enhances NO_x [DeCaria *et al.*, 2000, 2005; Zhang *et al.*, 2003; Hudman *et al.*, 2007]. The importance of the vertical distribution of O_3 and its precursors is emphasized by the fact that midtropospheric and upper tropospheric O_3 has a larger radiative forcing efficiency [Lacis *et al.*, 1990] than O_3 in the lower troposphere. Therefore, O_3 resulting from lightning NO_x and NO_x transported upward in deep convection has the greatest consequences for the greenhouse effect [IPCC, 2007].

While the IPCC definition of radiative forcing only considers anthropogenic changes, in general, both anthropogenic and natural O_3 contribute to radiative forcing (i.e., reduction in the outgoing longwave radiation). In our study, the radiative forcing of O_3 produced from anthropogenic emissions and lightning NO emissions is considered separately. Although a number of studies analyzed the impact of lightning NO_x (L NO_x) and anthropogenic NO_x (A NO_x) emissions on the amounts of

tropospheric NO_x and O₃ [e.g., *Zhang et al.*, 2003; *Hudman et al.*, 2007, 2009; *Allen et al.*, 2010, 2012], the radiative effects due to O₃ production from these sources have been investigated in relatively few studies. These studies include *Dahlmann et al.* [2011], who conducted multi-decadal simulations using a global chemistry climate model, and *Choi et al.* [2009], who conducted multi-month simulations using a regional chemical transport model.

The first part of the current study focuses on estimating both anthropogenic and lightning contributions to radiative forcing using the coarse global chemical transport model University of Maryland Chemical Transport Model (UMD-CTM) [*Park et al.*, 2004a] with offline radiative forcing calculation. The specific objectives are:

- Compare impacts of anthropogenic and lightning NO emissions on long-range transport of trace gases from North America.
- Quantify the North American anthropogenic and lightning contributions to tropospheric ozone and its climate forcing.
- Analyze the impact of the North American Monsoon and reduced power plant emissions between summers 2002 and 2004 (the NO_x SIP Call) on the radiative forcing of tropospheric ozone.

The second part of the current study uses the regional scale model WRF-Chem [*Grell et al.*, 2005], in which chemistry is fully coupled with meteorology and radiation, to better account for the highly variable regional character of ozone. We incorporate model ozone in the radiation schemes, which we refer to as interactive

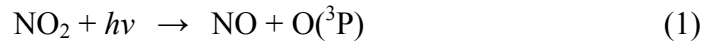
ozone, thus allowing heating rates from ozone to affect the simulated meteorological and chemical quantities. The specific objectives are:

- Test the performance of a new lightning parameterization scheme which uses convective precipitation and mixed phase depth as predictors [*Hansen*, 2012].
- Quantify the impact of interactive ozone on outgoing longwave radiation. Test whether the inclusion of model ozone in radiation schemes improves the accuracy of radiative flux calculations.
- Quantify the instantaneous radiative forcing due to lightning NO_x, which has received little attention on a regional scale.

2 Background

2.1 Tropospheric Ozone Production

In the clean troposphere, ozone is produced and removed primarily through the following reactions:



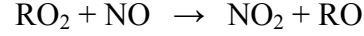
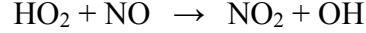
Last two reactions are relatively fast. Therefore, the slower photolysis reaction 1 is usually rate-limiting for this photochemical cycle and the reason why ozone concentrations are high during summer when temperatures are high and solar radiation is intense. The cycle time for these three reactions is only a few minutes. The ozone concentration at steady state is given by the so-called photostationary state equation:

$$[\text{O}_3] = j_{\text{NO}_2} [\text{NO}_2] / (k_{\text{NO}+\text{O}_3} [\text{NO}])$$

where j_{NO_2} is the photolysis rate of NO_2 and $k_{\text{NO}+\text{O}_3}$ is the rate constant for reaction 3. The net effect is neither to generate nor destroy ozone.

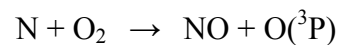
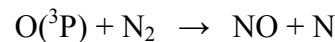
Ozone is also photolyzed to form excited atomic oxygen $\text{O}({}^1\text{D})$, which combines with water to produce the OH radical. The OH radical is important for the oxidation of CO and volatile organic compounds (VOCs) in the polluted troposphere,

producing HO₂ and RO₂, respectively. HO₂ and RO₂ react with NO to create NO₂ without consuming an ozone molecule:



Ozone production efficiency, the total number of ozone molecules formed per molecule of NO_x consumed, depends nonlinearly on the abundance of both NO_x and VOCs. The degree of nonlinearity depends on the VOC/NO_x concentration ratio, as well as the types of VOC species [Liu *et al.*, 1987; Lin *et al.*, 1988]. In the NO_x-sensitive regime (with relatively low NO_x and high VOC), ozone increases with increasing NO_x and changes little in response to increasing VOC. In the NO_x-saturated or VOC-sensitive regime, ozone decreases with increasing NO_x and increases with increasing VOC [Sillman, 1999].

Major sources of NO_x in the troposphere, in order from largest to smallest, are: fossil fuel combustion, biomass burning, lightning and soil release. While the two largest sources are emitted at the surface, lightning NO_x is produced largely in the middle to upper troposphere where it is relatively long-lived and more efficient at producing ozone. The high temperature in the lightning channel (~30,000 K) causes molecular nitrogen (N₂) and oxygen (O₂) in the atmosphere to dissociate into their atomic states. The formation of NO following a lightning flash is described by the Zel'dovich mechanism [Zel'dovich and Razier, 1967]:



NO is further oxidized to NO₂; however, during daytime conditions, NO₂ is also quickly photodissociated to NO, and an equilibrium between NO and NO₂ is reached within minutes. Therefore, it is useful to consider the sum of NO and NO₂ (NO_x).

Tropospheric O₃ has an average lifetime on the order of weeks. This relatively short lifetime compared to the long-lived and well-mixed greenhouse gases (CO₂, CH₄, halocarbons, and N₂O) implies that the distribution of tropospheric ozone is highly variable in space and time. The longer chemical lifetimes and greater wind speeds aloft can then lead to significant long-range transport of NO_x during which photochemical O₃ production occurs. On the other hand, the vertical mixing that occurs during convection over unpolluted regions can decrease the tropospheric O₃ column as high O₃ air from the upper troposphere (UT) is transported downwards to levels where it is destroyed more quickly, and low O₃ air that originated near the surface is deposited in the UT [*Lelieveld and Crutzen, 1994*].

2.2 Upper Tropospheric NO_x and LNO_x – Lessons From INTEX-A Campaign

Measurements from the INTEX-A (Intercontinental Chemical Transport Experiment–Phase A) aircraft campaign over the contiguous United States (CONUS) and adjacent areas [*Singh et al., 2006*] and from coordinated IONS (INTEX Ozonesonde Network Study) ozonesondes launches [*Thompson et al., 2007a, 2007b*] showed that the North American upper troposphere was greatly influenced by both LNO_x and surface pollution, lofted via convection, that contained elevated concentrations of peroxyacetyl nitrate (PAN), O₃, hydrocarbons and NO_x [*Cooper et*

al., 2006; *Singh et al.*, 2007]. These measurements indicated large amounts of NO_x in the upper troposphere and suggested that the lightning NO_x source is far larger than anticipated [*Singh et al.*, 2007]. Further studies from the same campaign found that lightning NO was responsible for 60%–80% of upper tropospheric NO_x and 15%–20% of upper tropospheric ozone over the eastern United States during the summertime [*Hudman et al.*, 2007, 2009; *Pfister et al.*, 2008; *Cooper et al.*, 2009, *Allen et al.*, 2010, 2012].

Hudman et al. [2009] found that during the INTEX-A period the hemispheric tropospheric O₃ burden was enhanced with comparable contributions from anthropogenic and lightning NO emissions over North America. Modeling of the horizontal and vertical distribution of LNO_x is highly uncertain. In the study by *Hudman et al.* [2007], the GEOS-Chem standard simulation greatly underestimated NO_x in the UT. After increasing the lightning NO production to 500 mol flash⁻¹, GEOS-Chem simulated NO_x was still low biased. Similarly, *Bousserez et al.* [2007], *Pierce et al.* [2007], *Fang et al.* [2010], and *Allen et al.* [2010] underestimated upper tropospheric NO_x using the MOCAGE, RAQMS, MOZART and GMI chemical transport models (CTMs) (all with different lightning schemes), respectively. Using a completely different approach, *Ott et al.* [2010] found that using a 500 mol flash⁻¹ LNO_x source produced the best comparison between NO_x in cloud-resolved model simulations and storm anvil observations in the midlatitudes and subtropics.

2.3 Radiative Forcing of Tropospheric Ozone

Ramaswamy et al. [2001] defines radiative forcing for tropospheric O₃ as the net downward flux (both the longwave and the much smaller shortwave contribution) at the tropopause due to the anthropogenic increase in tropospheric O₃ from preindustrial times. The global annual average present-day radiative forcing (stratospheric adjusted) due to tropospheric O₃ is +0.35 [0.25 to 0.65] W m⁻² as estimated by climate simulations (Figure 1). If the stratospheric temperatures are not readjusted to radiative equilibrium, then the forcing is called the instantaneous radiative forcing. Other studies [e.g., *Ramanathan et al.*, 1989; *Aghedo et al.*, 2011] use a more fundamental definition of radiative forcing, which is defined as the change in the radiative fluxes at the top of the atmosphere.

Through production of tropospheric O₃, NO_x emissions lead to a positive radiative forcing of climate (warming), but by increasing the concentration of OH, they reduce the levels of CH₄, providing a negative forcing (cooling) that partly offsets the O₃ forcing [*Derwent et al.*, 2008]. Because of the long lifetime of CH₄ (~10 years) relative to the length of our simulations, the cooling effect of CH₄ is neglected in our study.

As discussed in several previous studies [e.g., *Lacis et al.*, 1990; *Gauss et al.*, 2003] estimation of radiative forcing of tropospheric O₃ depends on the spatial and, most importantly, the vertical distribution of O₃ within the entire troposphere and lower stratosphere. Ozone increases (in terms of molecules added) near the tropopause are radiatively most efficient. *Aghedo et al.* [2011], using direct observations of infrared radiance at high spectral resolution by the Tropospheric

Emission Spectrometer (TES) instrument, derived a satellite-based estimate of the outgoing longwave radiation (OLR) sensitivity to ozone variations, the so-called instantaneous radiative forcing (IRF) kernels. These IRF kernels represent the sensitivity of OLR to the vertical and spatial distribution of ozone under all sky conditions [Worden *et al.*, 2011]. Their results indicate that OLR is most sensitive to changes in middle tropospheric ozone (near 400 hPa) over the tropics and midlatitudes with large values of IRF kernel ($0.5 \text{ mW m}^{-2} \text{ ppbv}^{-1}$) located between 650–200 hPa, which corresponds to a region of lightning enhanced ozone. This midtropospheric sensitivity is a consequence of change in volume mixing ratio concentrations having a larger effect on total column in the middle troposphere than at the upper troposphere [Aghedo *et al.*, 2011]. Choi *et al.* [2009] showed that this midtropospheric and upper tropospheric enhancement of ozone due to LNO_x has a greater impact on radiative fluxes than the lower tropospheric enhancement due to anthropogenic NO_x over North America and western North Atlantic.

RADIATIVE FORCING COMPONENTS

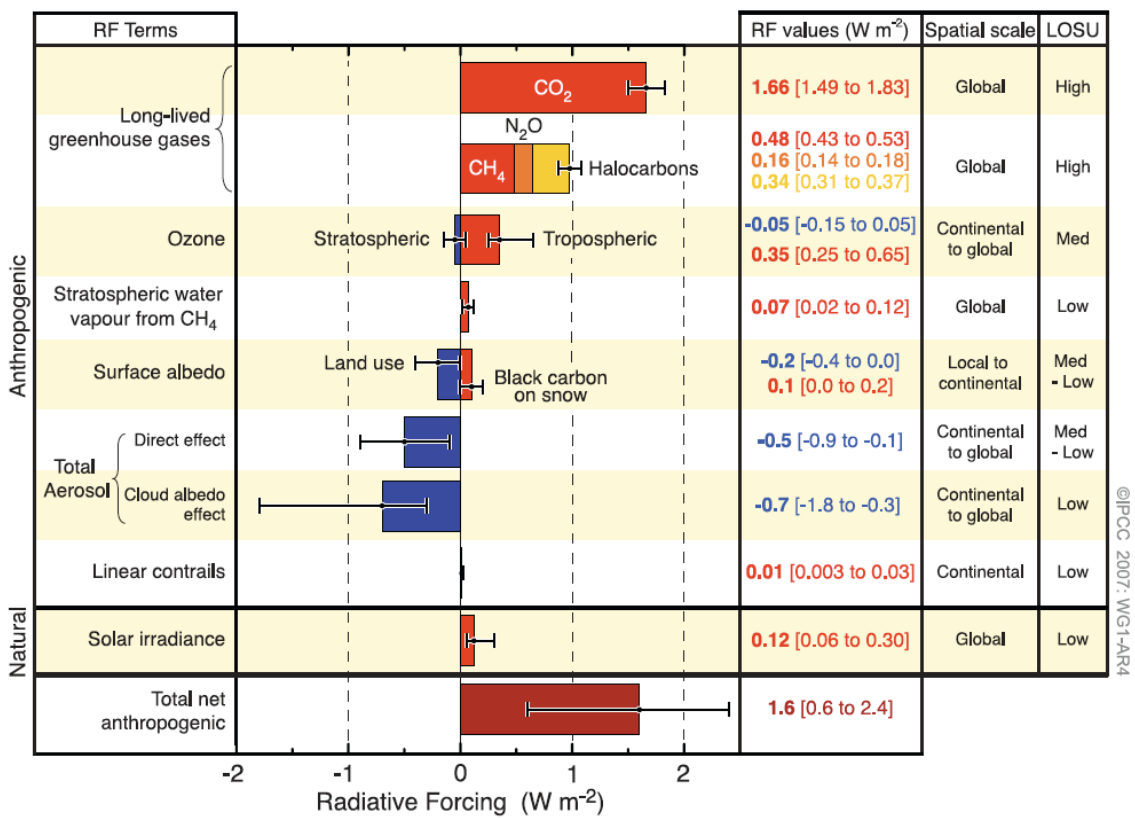


Figure 1. Radiative forcing (RF) of climate between 1750 and 2005 as estimated by the IPCC. Estimates of RF are accompanied by both an uncertainty range and a level of scientific understanding (LOSU). The value uncertainties represent the 5 to 95% (90%) confidence range, and are based on available published studies; the LOSU is a subjective measure of structural uncertainty and represents how well understood the underlying processes are [IPCC, 2007].

3 Global Modeling

3.1 Introduction

We extend previous work focused on NO_y export from North America during the INTEX-A period in summer 2004 by estimating the climate implications (radiative effects). The summer 2004 is compared to a meteorologically different summer (2002) using the University of Maryland Chemistry and Transport Model (UMD-CTM) [Park *et al.*, 2004a, 2004b]. Godowitch *et al.* [2008], using the Community Multiscale Air-Quality (CMAQ) model, showed that reduced NO_x emissions from power plants [Frost *et al.*, 2006; Kim *et al.*, 2006] caused substantial decreases in NO_x concentrations aloft (300–1100 m) and in ground level daily 8 h O₃ maxima between the summers 2002 and 2004. Sites downwind of the emission-rich Ohio River Valley (ORV) region (i.e., Pennsylvania, Ohio, West Virginia, Kentucky, Indiana and Illinois) experienced the greatest decreases in daily 8 h O₃ maxima between 2002 and 2004. Interestingly, Godowitch *et al.* [2008] found that meteorological effects had greater impact on O₃ than those from emission changes over the region north of the Ohio River (Illinois, Indiana, Ohio, Wisconsin and Michigan). In particular, temperature and moisture parameters were considerably different in summer 2004 than 2002. Average maximum temperatures were substantially cooler in the northeastern United States (U.S.), by as much as 3°C–5°C, during summer 2004 [Godowitch *et al.*, 2008]. Meteorology over northeastern NA during summer 2004 was dominated by persistent low pressure, and there were increased synoptic disturbances relative to summer 2002 [Thompson *et al.*, 2007a, 2007b; Büker *et al.*,

2008]. The number of cold frontal passages over the northeastern United States was above average in summer 2004 [Fuelberg *et al.*, 2007]. As we estimate later the increase in LNO_x emissions (due to more frequent lightning in summer 2004 than in 2002) is at least a factor of 2 larger than the decrease in ANO_x emissions (due to power plant NO_x reductions).

In addition, we analyze the impact of the North American Monsoon. The monsoon region of the southwestern United States and northwestern Mexico does not have large ANO_x emissions but has a large increase in LNO_x emissions after the onset of the monsoon [Ridley *et al.*, 1994]. Much of the LNO_x becomes trapped in the UT above the Gulf of Mexico, the southern United States and Mexico—the major NA lightning region [Li *et al.*, 2005; Cooper *et al.*, 2006]—where conditions are favorable for O₃ production. On the basis of rainfall statistics over the southwestern United States (Arizona and New Mexico) and northwestern Mexico, 2004 is considered a weak monsoon year and 2002 is a near-normal or slightly weak monsoon year (daily climatology available at <ftp://ftp.cpc.ncep.noaa.gov/precip/wd52ws/us-mex/>).

For both summers, we quantify the NA contribution to tropospheric O₃ by conducting sensitivity simulations with either anthropogenic or lightning emissions over North America shut off. In section 3.2, we describe the updated UMD-CTM, which has undergone major revision since Park *et al.* [2004a] and lightning simulations performed for this study. Section 3.3 includes model comparisons with aircraft, ozonesonde, satellite and ground-based measurements. We determine the model biases for O₃, NO_x and other trace gases. We then discuss the summer-to-

summer variability of lightning and the radiative impact of O₃ produced from NA anthropogenic and lightning emissions in the outflow region. The results are summarized in section 3.4.

3.2 Model Description

The UMD-CTM was described in detail in *Park et al.* [2004a]; here we describe it briefly in terms of the experimental design. The horizontal resolution of the model is 2° × 2.5°. From the surface to 9.3 hPa, there are 14 sigma layers and 17 constant pressure layers with a sigma-pressure transition (at 177 hPa) near the tropopause. The UMD-CTM is driven by assimilated meteorological fields from version 4 of the Goddard Earth Observing System (GEOS-4) of the NASA Global Modeling and Assimilation Office. Specifically, we use the GEOS-4 CERES (Clouds and the Earth's Radiant Energy System) reanalysis (http://gmao.gsfc.nasa.gov/research/merra/sci_archive/climate.php). Convection in GEOS-4 [*Bloom et al.*, 2005] is represented by two parameterizations: deep convection follows *Zhang and McFarlane* [1995], while shallow convection is based on work by *Hack* [1994]. Moist convective transport in the UMD-CTM is parameterized using updraft, downdraft, entrainment and detrainment fields from the GEOS-4 CERES reanalysis. Turbulent mixing is calculated through a fractional mixing scheme [*Allen et al.*, 1996]: during a CTM time step (15 min) 20% of the mass in each model layer within the BL is mixed completely throughout the BL. Stratospheric O₃ flux into the troposphere is controlled through the synthetic O₃ (Synoz) scheme [*McLinden et al.*,

2000] as in work by *Park et al.* [2004a]. The Synoz-based flux is set to 475 Tg O₃ yr⁻¹ for both years following *McLinden et al.* [2000].

We use the same chemical mechanism as in the work by *Park et al.* [2004a] but with updated rate constants based on work by the *Jet Propulsion Laboratory* [2006]. We implemented the parameterization of quantum yields to update the photolysis rates for acetone on the basis of work by *Blitz et al.* [2004]. The wet deposition scheme [*Liu et al.*, 2001] includes contributions from scavenging in convective updrafts and rainout and washout from convective anvils and large-scale precipitation, and it allows for reevaporation.

Table 1 identifies the modeling scenarios used to isolate the impacts of anthropogenic emissions, lightning and their summer-to-summer variability on O₃ concentrations. Initial conditions for O₃ were obtained from NASA's Global Modeling Initiative Chemistry and Transport Model (GMI CTM) [*Douglass et al.*, 2004] driven by meteorological input from the Finite Volume General Circulation Model (FVGCM) with several-year spin-up. Initial conditions for other species were obtained from a reduced 4° × 5° simulation of 1985 with the UMD-CTM by *Park et al.* [2004a] in the troposphere and from the GMI CTM in the stratosphere. The meteorological fields from the FVGCM do not correspond to a particular year.

Table 1. The UMD-CTM Simulations With Different Sources of NO_x Emissions

Simulation Name	Anthropogenic NO _x ^a	Lightning NO _x ^b	Period Simulated
L0	CEMS 2004	OTD/LIS (240)	May–Aug 2004
L1 (standard)	CEMS 2002	NLDN-based (240)	May–Aug 2002
L1 (standard)	CEMS 2004	NLDN-based (240)	May–Aug 2004
L2 (doubled lightning)	CEMS 2004	NLDN-based (480)	May–Aug 2004
noAnthro-NA ^c	none	NLDN-based (240)	May–Aug 2002
noAnthro-NA ^c	none	NLDN-based (240)	May–Aug 2004
noL-NA ^c	CEMS 2002	none	May–Aug 2002
noL-NA ^c	CEMS 2004	none	May–Aug 2004
no NO _x SIP Call	CEMS 2002	NLDN-based (240)	May–Aug 2004

^a Emission inventory used for the power plant sector for the contiguous United States (CONUS).

^b Observed flash rates used to adjust the model flash rates over the CONUS; lightning NO mol flash⁻¹ over the CONUS are in parentheses.

^c North America is defined as Canada, the CONUS, Mexico, and the Gulf of Mexico.

3.2.1 Anthropogenic Emissions

In 1998, the U.S. Environmental Protection Agency (EPA) issued a regulation to reduce the interstate transport of NO_x and ground level O₃ in the eastern United States [Environmental Protection Agency, 2005]. This rule, commonly known as the NO_x State Implementation Plan (SIP) Call, started to be implemented in 2003 and required substantial power plant NO_x emission reductions in 22 eastern states [Frost *et al.*, 2006] with full implementation of controls to be completed by the summer 2004 O₃ season. In 2000, according to EPA's National Emission Inventory (NEI) and

the Emission Database for Global Atmospheric Research (EDGAR), U.S. power generation accounted for one quarter (1.5 Tg N) of national ANO_x emissions (5.9 Tg N). Other major sources included road transport (1.9 Tg N), international shipping (0.6 Tg N) and air transport (0.3 Tg N).

Global anthropogenic emissions in the model are as described by *Park et al.* [2004a] unless otherwise specified. Monthly power plant NO_x emissions from the United States are taken from Continuous Emission Monitoring System (CEMS). These direct measurements represent one of the most accurate parts of the U.S. emission database (<http://www.epa.gov/airmarkets/emissions>). All other anthropogenic emissions are from EDGAR 3.2 Fast Track 2000 (available at http://themasites.pbl.nl/tridion/en/themasites/edgar/emission_data/edgar_32ft2000/documentation/index-2.html) [*Olivier and Berdowski*, 2001; *Olivier et al.*, 2005]. Because of EPA's SIP Call, NO_x emitted from ORV power plants decreased on average by 50% between the summers 2002 and 2004. Overall, the NO_x SIP Call resulted in a 10% reduction in total ANO_x emissions from the CONUS.

The power plant NO_x emissions are released from tall stacks (average stack height is 76 m) in plumes with considerable buoyancy (average release temperature is 117°C). Stack emissions of NO_x are injected into the second lowest model layer. All other anthropogenic emissions are injected into the lowest model layer. In the UMD-CTM, the lowest levels are centered at approximately 50, 250, 600, 1100 and 1900 m above the local surface.

We increase ANO_x emissions in eastern China by 15% above the 2000 EDGAR NO_x emissions for both summers since a large positive trend of tropospheric

NO_2 was reported by *Richter et al.* [2005] and *van der A et al.* [2006] over the industrial areas in China. It should be noted that we hold all nonpower plant U.S. NO_x emissions constant between 2002 and 2004; we also hold non-U.S. ANO_x emissions of any type constant between the 2 years. The spatial distribution of the changes in surface NO_x emissions from summer 2002 to 2004 over the United States used in the UMD-CTM simulations is shown in Figure 2.

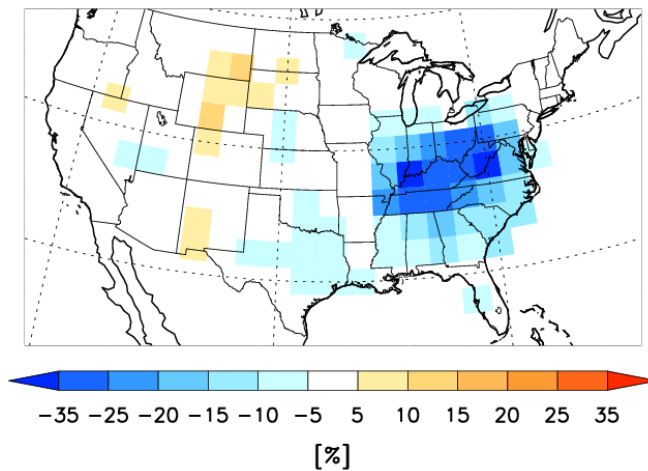


Figure 2. Surface NO_x emission change from summer 2002 to 2004 at the $2^\circ \times 2.5^\circ$ resolution as represented in the UMD-CTM standard simulations. Negative values indicate ANO_x emission decreases from 2002 to 2004.

3.2.2 Lightning

The annual global LNO_x production is set to 5 Tg N yr^{-1} , which is in the center of the currently accepted range of $2\text{--}8 \text{ Tg N yr}^{-1}$ [*Schumann and Huntrieser*, 2007]. The lightning scheme follows *Allen et al.* [2010]. The LNO_x production is assumed to be directly proportional to lightning flash rate FR as:

$$FR = G \times L \times (zmmu - zmmu_0)^k,$$

where $zmmu$ is GEOS-4 CERES upward cloud mass flux (at ~ 430 hPa). The lightning is thus colocated with the convective transport in the CTM. FR is set to zero for $zmmu < zmmu_0$. We use $zmmu_0 = 0.57 \text{ kg m}^{-2} \text{ min}^{-1}$ as in the work by *Allen et al.* [2010] with $k = 2$, thus assuming that the FR is a quadratic function of $zmmu$; $k = 2$ gives more realistic day-to-day variability in model flash rates, decreases biases and improves correlations with respect to observed flash rates than $k = 1$. Using observations from the spaceborne Optical Transient Detector/Lightning Imaging Sensor (OTD/LIS) [*Boccippio et al.*, 2002; *Christian et al.*, 2003; *Mach et al.*, 2007] and from the ground-based National Lightning Detection Network (NLDN) [*Cummins et al.*, 1998; *Orville and Huffines*, 2001], we scale lightning flash rates (FR) globally (G) and locally (L) so the model flash rates per grid box match the NLDN and/or OTD/LIS observed data sets on a monthly basis (details in the work by *Allen et al.* [2010], who scaled FR to match the global OTD/LIS v2.2 climatology). In the vertical, we partition lightning NO emissions on the basis of the modeling studies of *Pickering et al.* [1998].

Table 1 shows three lightning simulations with the UMD-CTM.

In L0, total flash rates (FR) derived from convective mass fluxes are adjusted to match the flash rates observed by OTD/LIS from space. We use Low Resolution Monthly Time Series (LRMTS) in the region between 35°S and 35°N and Low Resolution Annual Climatology (LRAC) elsewhere (available at <http://thunder.msfc.nasa.gov/data>). Since month-specific LIS observations are

available only south of 35°N, simulation L0 does not account for summer-to-summer variability of NA lightning poleward of 35°N.

In L1, in addition to the L0 approach, over the CONUS, the flash rates derived from convective mass fluxes are adjusted to match the monthly average NLDN-based IC (intra-cloud) + CG (cloud-to-ground) flash rates (details are below). L1 is called “standard simulation.”

In L2, in addition to the L1 approach, NO production per flash over the NA midlatitudes (25°N–50°N) is increased by a factor of 2 to 480 mol flash⁻¹, which nearly matches the estimates of *Ott et al.* [2010] derived from cloud-resolved modeling and of *Hudman et al.* [2007] used in their improved GEOS-Chem simulation of the INTEX-A period.

When determining the NLDN-based IC + CG flash rates (simulations L1 and L2), we remove NLDN flashes with peak currents between 0 and 20 kA, since they are assumed to be IC in character [*Biagi et al.*, 2007]. We only use data over the CONUS for scaling as the NLDN detection efficiency drops off rapidly beyond 300 km from shore. The NLDN underwent a system-wide upgrade during 2002 [*Cummins et al.*, 2006]. The mean preupgrade detection efficiency over the CONUS was ~85%. After this upgrade, which began in spring 2002, the NLDN had a detection efficiency of 90%–95% over the CONUS. For summer 2004, we thus use a detection efficiency of 93%. In order to estimate the detection efficiency for summer 2002, we average the preupgrade value derived from *Cummins et al.* [1998, Figure 9] and postupgrade value of 93%. To obtain the total IC + CG flash rates, we multiply the detection efficiency-adjusted NLDN CG flashes by $Z + 1$, where Z is the IC/CG

ratio. *Boccippio et al.* [2001] constructed a $0.5^\circ \times 0.5^\circ$ daily climatology of Z ratios (not year specific), by using observations of NLDN CG flashes and OTD/LIS total (IC + CG) flashes. In our study, we smooth their Z composite with a 7.5° moving boxcar, calculate the monthly averages and interpolate onto the $2^\circ \times 2.5^\circ$ UMD-CTM grid. Before smoothing, we exclude grid boxes with $Z > 12$ as these values are anomalous [*Boccippio et al.*, 2001].

To compare the lightning sources in our simulations with other investigators, we summarize the lightning NO emissions over the CONUS and adjacent coastal areas during INTEX-A (1 July to 15 August 2004) in Table 2. Simulations L0, L1 and L2 yield LNO_x emissions of 0.16 Tg N, 0.25 Tg N and 0.50 Tg N, respectively. *Hudman et al.* [2007, 2009], using a cloud top height-based flash rate scheme and assuming 500 NO mol flash $^{-1}$, obtained a LNO_x emission of 0.27 Tg N over the same areas for that period. They noted that their flash rates were biased low with respect to NLDN-based flash rates (assuming an IC/CG ratio of 3). Adjusting for this bias, they obtained a best estimate of 0.45 Tg N for the lightning NO source; however, they did not use this in their model simulations. *Jourdain et al.* [2010], with their GEOS-Chem simulation with NLDN-based flashes and an assumed production of 520 NO mol flash $^{-1}$, obtained a source of 0.28 Tg N for July 2006. Extrapolating to 1.5 months gives 0.42 Tg N, which is close to the bias-adjusted estimate by *Hudman et al.* [2007] for 2004. *Allen et al.* [2010], using the GMI CTM, reported 0.17 Tg N in their standard simulation and 0.34 Tg N in their simulation with doubled lightning NO production (480 mol flash $^{-1}$). They scaled to OTD/LIS climatology rather than NLDN-based flash rates. The magnitude of lightning source in our standard

simulation (L1) nearly matches the one used by *Hudman et al.*, while the L2 source (0.50 Tg N) is close to their NLDN-based estimate of the source.

It is noteworthy that the 50% increase in CONUS LNO_x emissions between 2002 and 2004 more than offsets the ANO_x emission decreases due to the NO_x SIP Call. By applying this 50% increase to L1 and L2 sources above, we obtain estimates of 0.13 and 0.25 Tg N, respectively, for the LNO_x emission changes from the same areas and time period as above. These estimated LNO_x emission increases are at least a factor of 2 larger than the corresponding decrease of 0.06 Tg N in ANO_x emissions due to the NO_x SIP Call (the ANO_x emissions from the CONUS were reduced from 0.57 Tg N to 0.51 Tg N) during the same time period. Of course the impact of the ANO_x emissions changes is most noticed near the surface while the impact of the LNO_x emissions changes is most important in the UT.

Table 2. The Lightning Sources Used in This Study and Other Studies

Reference	Scaling ^a	LNO _x Source ^b	Period Simulated
This study, simulation L0	OTD/LIS	0.16 (240)	1 Jul to 15 Aug 2004
This study, simulation L1	NLDN	0.25 (240)	1 Jul to 15 Aug 2004
This study, simulation L2	NLDN	0.50 (480)	1 Jul to 15 Aug 2004
<i>Hudman et al. [2007, 2009]</i>	no scaling	0.27 (500)	1 Jul to 15 Aug 2004
<i>Jourdain et al. [2010] (base)^c</i>	OTD/LIS	0.15 (260)	1 Jul to 15 Aug 2006
<i>Jourdain et al. [2010] (NLDN)^c</i>	NLDN	0.21 (260)	1 Jul to 15 Aug 2006
<i>Jourdain et al. [2010] (ligh×2)^c</i>	NLDN	0.42 (520)	1 Jul to 15 Aug 2006
<i>Allen et al. [2010] (low NO_x)</i>	OTD/LIS	0.17 (240)	1 Jul to 15 Aug 2004
<i>Allen et al. [2010] (high NO_x)</i>	OTD/LIS	0.34 (480)	1 Jul to 15 Aug 2004

^a Observed flash rates used to adjust the model (different models and lightning schemes) flash rates.

^b The lightning NO_x source in Tg N from the contiguous United States and adjacent coastal areas; lightning NO mol produced per flash are in parentheses.

^c Please note a different year (2006). The lightning sources for the period of 1 July to 15 August are estimated by multiplying the lightning source values from July 2006 by a factor of 1.5.

3.2.3 Biogenic Emissions

Isoprene emissions used in the UMD-CTM simulations come from monthly average hourly emissions calculated by the Model of Emissions of Gases and Aerosols from Nature (MEGAN) from standard case for summer 2003 [Guenther *et al.*, 2006]. One of the most important meteorological factors in determining the isoprene emissions is the temperature. *Pacifico et al.* [2009, Figure 4] shows that a 1°C temperature change can increase isoprene emissions by 15% for standard conditions (25°C–35°C). Temperatures in the region of high isoprene emissions were similar during summers 2002, 2003 and 2004 (Figure 3). Outside this region, maximum temperatures in 2002 exceeded maximum temperatures in 2004 by 1°C–5°C likely leading to more emissions in 2002 than in 2004. *Hogrefe et al.* [2004], in an isoprene sensitivity simulation with CMAQ, showed that summertime 8 h O₃ changed by <3 ppbv at locations within the domain (the eastern and central part of the United States) when isoprene emissions were increased by 20%–50% corresponding to maximum temperature increases of 1.5°C–3.5°C. *Nolte et al.* [2008], in another isoprene sensitivity simulation with CMAQ, showed that summertime 8 h O₃ increased by 1 ppbv or less over most of the CONUS, when isoprene emissions were increased by 25%. Therefore, the use of the same isoprene emissions for 2002 and 2004 is likely to have only a minor impact on conclusions from this study.

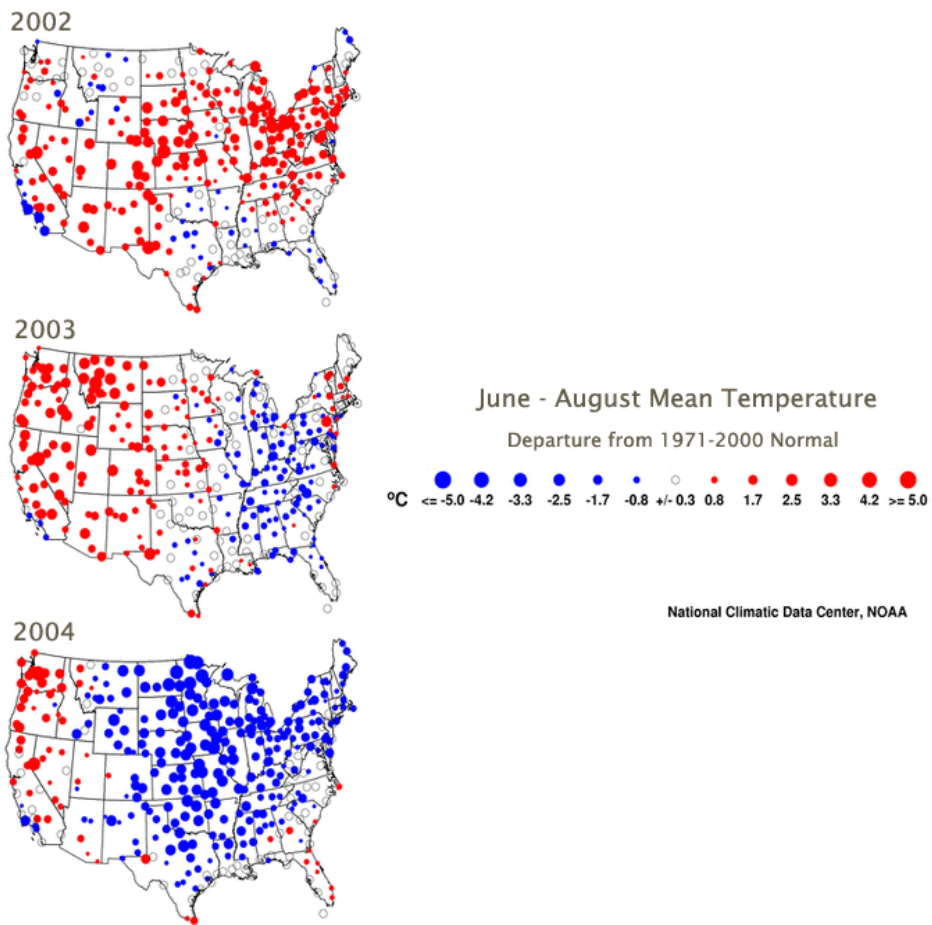


Figure 3. Surface temperatures in summer 2002, 2003 and 2004 (from www.ncdc.noaa.gov/oa/climate/research/2004/CMB_prod_us_2004.html).

Changes in GEOS-4 CERES temperatures, used in the UMD-CTM simulations, from summer 2002 to 2004 are smaller than the observed temperature changes shown in this figure. The mean GEOS-4 CERES temperature change from summer 2002 to 2004 over the region of high isoprene emissions (28°N - 40°N and 74°W - 96°W) is -1.5°C . Isoprene emissions used in the UMD-CTM simulations are from summer 2003.

3.2.4 Biomass Burning

Biomass burning emissions south of 48°N were derived from the Global Fire Emissions Database Version 2 (GFEDv2) [*van der Werf et al.*, 2006]. This data set prescribes emissions of total carbon as well as CO, CH₄ and NO_x. For other species, the total carbon emissions are converted to dry matter burned assuming a biomass carbon fraction of 0.45. Emission factors from *Andreae and Merlet* [2001] are then applied to estimate nonmethane hydrocarbon emissions. Factors are provided separately for savannah/grassland, tropical forest, extratropical forest and agricultural burning. Poleward of 48°N, we use emissions derived from Boreal Wildfire Emissions Model (BWEM) [*Kasischke et al.*, 2005] for summer 2002 and GFEDv2 emissions for summer 2004 (BWEM emissions for 2004 are unavailable). Land cover classification is derived from MODIS data [*Hansen et al.*, 2000; *Friedl et al.*, 2002].

The GFEDv2 database uses the CASA model to estimate fuel loads [*van der Werf et al.*, 2003] and a burned area database derived from MODIS observations [*Giglio et al.*, 2006] to estimate monthly biomass burning emissions on a 1° × 1° grid. For this study, MODIS active fire data [*Justice et al.*, 2002] are used to calculate a daily perturbation for each 1° × 1° grid cell. This perturbation function is then applied to GFEDv2 emissions to obtain daily estimated emissions without altering monthly emissions, similar to the approach used by *Heald et al.* [2003]. This approach has been demonstrated to improve the accuracy of atmospheric simulations as opposed to using monthly-averaged emissions [*Hyer et al.*, 2007; *Roy et al.*, 2007]. Biomass burning data at 1° × 1° resolution are smoothed with a 7 day moving average to reduce the effect of a periodic bias associated with the polar orbit of MODIS [*Heald*

et al., 2003] and are regredded onto the $2^\circ \times 2.5^\circ$ UMD-CTM grid. Biomass burning emissions are injected below 1.5 km outside the tropics and below 0.5 km within the tropics (in vertical, both uniformly distributed by mass).

3.2.5 Radiative Forcing Calculation

IPCC [2007] defines radiative forcing for tropospheric O₃ as the change in net downward flux (both the longwave and the much smaller shortwave contribution) at the tropopause due to the anthropogenic increase in tropospheric O₃ from preindustrial times. While the IPCC definition only considers anthropogenic changes, in general, both anthropogenic and natural O₃ contribute to instantaneous radiative forcing (i.e., reduction in the outgoing longwave radiation). In our study, we consider the instantaneous radiative forcing of O₃ produced from anthropogenic emissions and lightning NO emissions separately and compare their relative effects during long-range transport of trace gases from North America.

We calculate the longwave (980–1100 cm⁻¹ band) contribution of the net downward Radiative Flux at the tropopause for clear sky conditions (for brevity we refer to this as RF) from O₃ enhanced by anthropogenic emissions and lightning. RF serves as a measure of the extra heat (in W m⁻²) input into the troposphere due to changes in O₃ (before stratospheric temperatures are adjusted to the radiative equilibrium). We use the radiative transfer model from Chou *et al.* [2001]. Thermal infrared radiatively active constituents include N₂O, CH₄, CFC11, CFC12, CFC22, H₂O, CO₂, O₃ and background aerosol. Vertical distributions of O₃ are calculated by the UMD-CTM. Distributions of the other optically active constituents are held

constant with respect to time. Water vapor and temperature profiles and skin temperatures are prescribed from the GEOS-4 CERES reanalysis.

3.3 Results

In North America, O₃ concentrations and outflow are affected by both emission reductions and changes in meteorology [Godowitch *et al.*, 2008]. To quantify the impact of changes in meteorology and associated lightning, we use the UMD-CTM to simulate the summers of 2002 and 2004. Because of the wide availability of observations (INTEX-A), we use the summer 2004 as a reference year to evaluate the model performance with regard to lightning and implementation of pollution controls (NO_x SIP Call). We conduct three lightning simulations L0, L1 and L2 (Table 1) to account for current uncertainty in the simulation of lightning NO emissions and its relative role in the long-range transport of trace gases with respect to anthropogenic emissions.

3.3.1 Differences Between Summers 2002 and 2004

Large summertime flash rates over the CONUS enhance the NA upper troposphere and outflow region with NO_x. Figure 4 shows the time series of NLDN-based total lightning over the CONUS in summer 2002 and 2004. Because of numerous thunderstorms in early summer 2004 (1 June to 17 July), lightning flash rates over the CONUS were about 50% higher compared to early summer 2002. In late summer (18 July to 31 August), total flash rates over the CONUS in 2004 were similar to those in 2002. Additionally, the onset of the North American Monsoon over

the southwestern United States and northwestern Mexico for both years occurred in mid-July [Li *et al.*, 2004; Gao *et al.*, 2007]. Finally, there were contrasting patterns of vertical transport in early and late summer in the BL (Figure 5). In early summer, there was 10%–40% more convective lofting in 2004 than in 2002 over the ORV and much of the eastern, central and southern United States, with less lofting over New England. In late summer, there was less lofting over the central and southern United States in 2004, with more lofting over New England. Therefore, we break our analysis into two periods: early summer (1 June to 17 July) and late summer (18 July to 31 August).

Figure 6 shows GEOS-4 surface temperatures and winds at ~5.5 km above the local surface. A prominent feature of the circulation over the United States is the strong low-level jet transporting air and moisture from the Gulf of Mexico to the central United States up to ~45°N (not shown). At ~5.5 km, a strong anticyclone dominates the south-central and southwestern United States, consistent with 4 year climatology shown in the work by Li *et al.* [2005]. The anticyclonic circulation has important implications for the fate of convective outflow over the United States, as we discuss later. In addition to the upper-level anticyclone, the northward expansion of the subtropical Bermuda High in the late summer influences the winds along the east coast of the United States. In 2004, especially during early summer, enhanced westerlies over the eastern United States (Figure 6b), in combination with enhanced BL lofting (Figure 5b), promoted outflow of anthropogenic pollution from North America.

Figure 7 shows the spatial pattern of NLDN-based IC + CG flashes during early summer 2002 and 2004. Higher flash rates were detected over most of the U.S in early summer 2004 compared to 2002: a factor of 2–4 increase over the Plains (Colorado, Nebraska, Kansas, Oklahoma and northern Texas) and a factor of 1.5–2 increase over the southern United States and parts of the ORV (southern Illinois, Indiana and Kentucky). The mean IC + CG flash rates over the CONUS were $8.30 \text{ flash s}^{-1}$ and $12.94 \text{ flash s}^{-1}$ in early summer 2002 and 2004, respectively.

In order to compare lightning flash rates (IC + CG) observed from space and detected from the NLDN, we construct the time series shown in Figure 8. This comparison presents the sums over the CONUS south of 35°N as derived from NLDN and LIS observations. Both the NLDN- and LIS-time series agree that June and July of 2004 had increased flash rates with respect to 2002 in this region. However, we find that more lightning was observed by the NLDN network (after adjustment by the IC/CG ratios) than by the LIS sensor during summers 2002–2005. Similarly, *Jourdain et al.* [2010] found that NLDN-based flash rates (assuming an IC/CG ratio of 3) over the CONUS (25°N – 50°N) in July 2006 were about 40% higher than OTD/LIS flash rates. Over the CONUS south of 35°N , the summertime IC/CG ratios average 3.17 (when the grid boxes are weighted by the CG flash rates during 2002–2004). While we do not have a reason to believe that IC/CG ratios are overestimated, if we decrease this mean summertime IC/CG ratio from 3.17 to 1.41, then the mean combined flash rates (IC + CG) derived from the NLDN would be consistent with the ones derived from the LIS. In our analysis, we exclude weak positive flashes (peak current $< 20 \text{ kA}$) from the NLDN data. It should be noted that

removing only 0–10 kA flashes, as done by *Boccippio et al.* [2001], would require the summertime IC/CG ratios in this region to be decreased even more (to IC/CG = 1.24) for an agreement between NLDN- and OTD/LIS-based estimates of total flash rate. Therefore, model flash rates from simulation L1 (adjusted to NLDN data) exceed model flash rates from simulation L0 (adjusted to OTD/LIS) as shown in Figure 9 for early summer 2004.

To summarize, the LIS-derived flash rates are nearly a factor of 2 lower than NLDN-based IC + CG flash rates south of 35°N, suggesting either (1) a fraction of NLDN flashes with negative peak currents are actually IC flashes, (2) the climatological IC/CG ratios are overestimated, or (3) LIS flash rates are underestimated. The latter two possibilities could be caused by uncertainties resulting from temporal and spatial undersampling by LIS [*Boccippio et al.*, 2001]. The uncertainties of lightning detection by LIS are discussed in *Boccippio et al.* [2002].

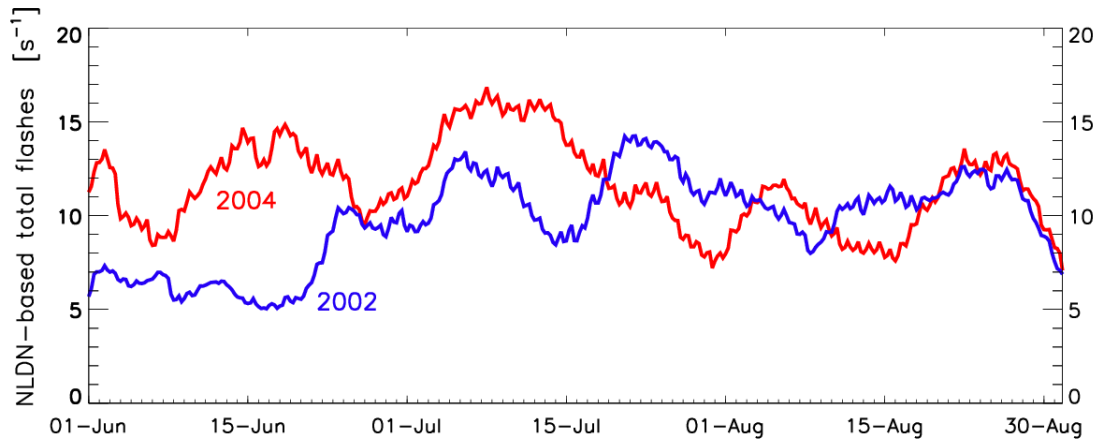


Figure 4. Total (IC + CG) lightning flash rates for the summers 2002 (blue) and 2004 (red) over the CONUS derived from the NLDN-observed CG flashes (adjusted by the IC/CG ratios). Flash rates are smoothed with a 7 day moving average.

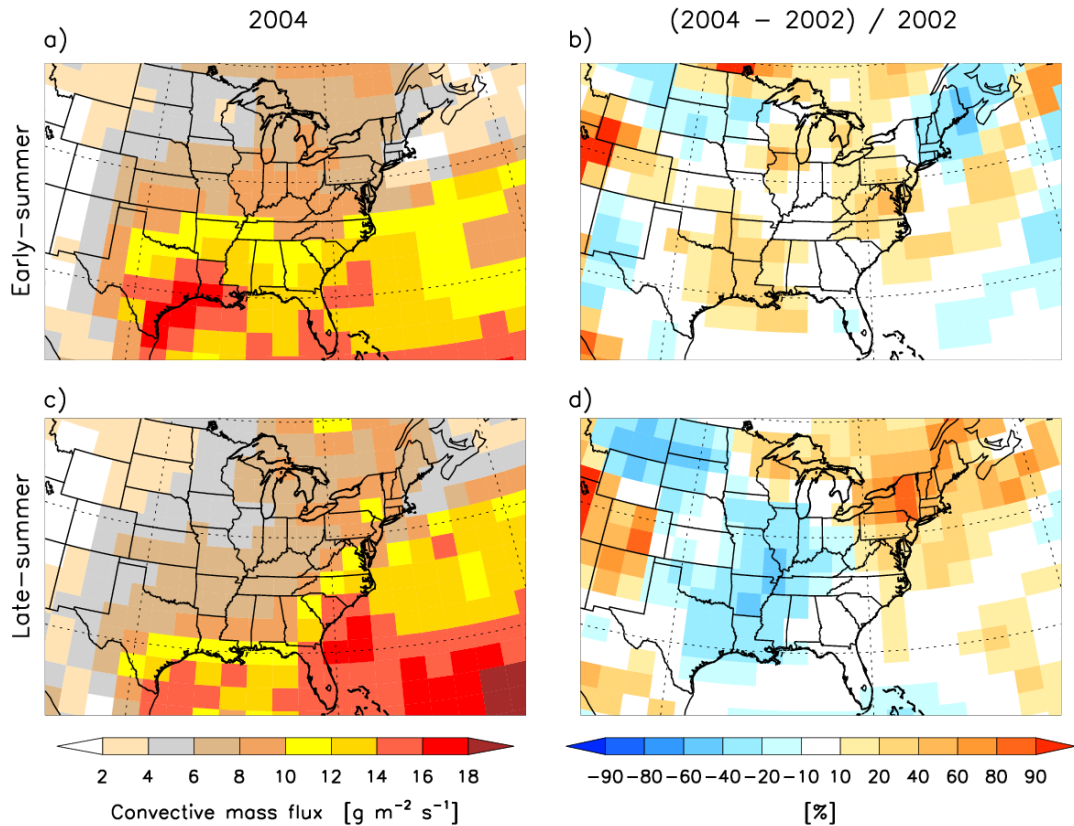


Figure 5. Convective mass fluxes (mean from the surface to 700 hPa) averaged for (a) 1 June to 17 July 2004 and (c) 18 July to 31 August 2004 and the relative change (%) between 2002 and 2004 averaged for (b) early and (d) late summer. Warm (cold) colors indicate more (less) vertical mixing by convection in 2004 than in 2002. Convective mass fluxes are calculated as the sum of deep convection and shallow convection fields from the GEOS-4 CERES reanalysis.

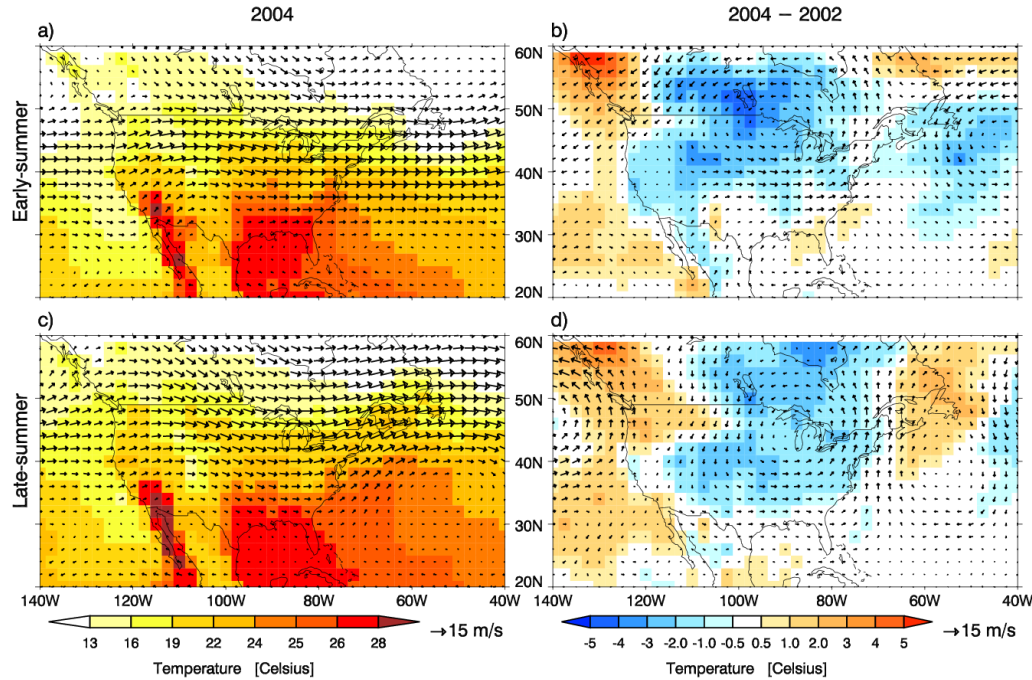


Figure 6. Mean GEOS-4 CERES surface temperatures and winds at ~ 5.5 km above the local surface for the period of (a) 1 June to 17 July 2004 and (c) 18 July to 31 August 2004 and the differences relative to 2002 for (b) early and (d) late summer.

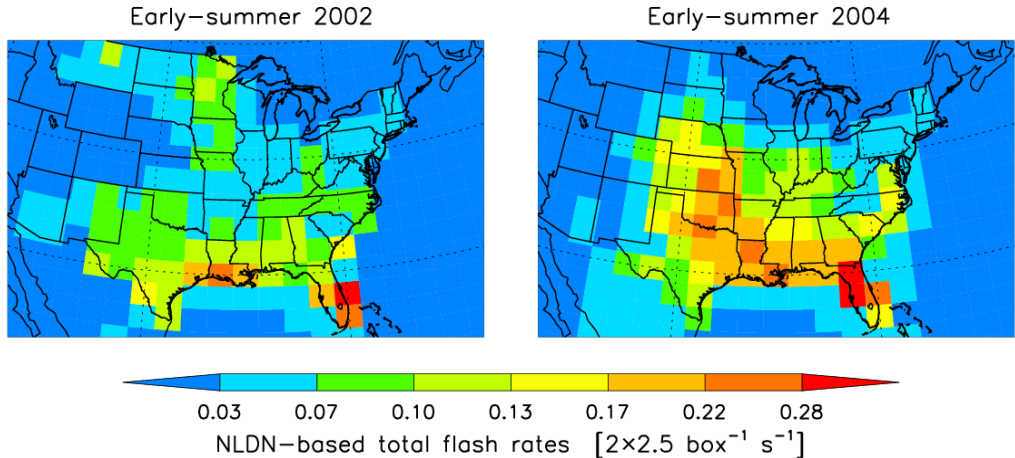


Figure 7. The NLDN-based total (IC + CG) lightning flash rates from (left) 2002 and (right) 2004 over the CONUS during early summer (1 June to 17 July). For comparison with the UMD-CTM flash rates for early summer 2004, see Figure 9.

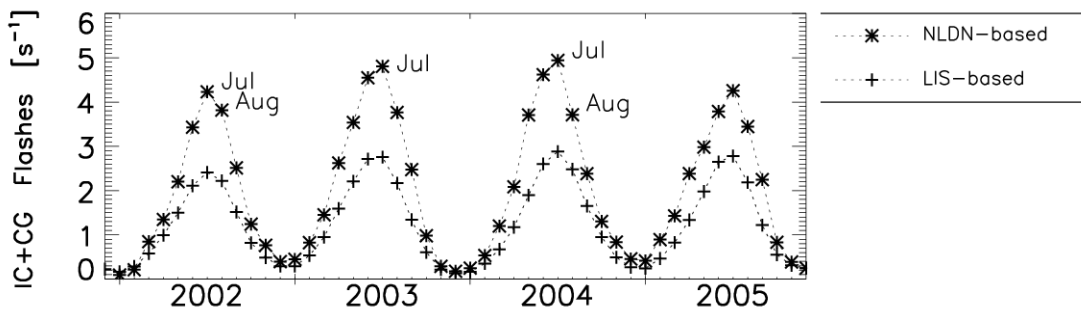


Figure 8. Total (IC + CG) lightning flash rates derived from NLDN ground and LIS spaceborne observations over the CONUS (land only) south of 35°N during 2002–2005. CG flash rates detected by the NLDN network (adjusted by the IC(CG ratios) are smoothed spatially (7.5° boxcar) and temporally (98 day window) and averaged for each month (indicated by the asterisks). Monthly LIS observations (LRMTS) were also smoothed with 98 day and 7.5° moving average.

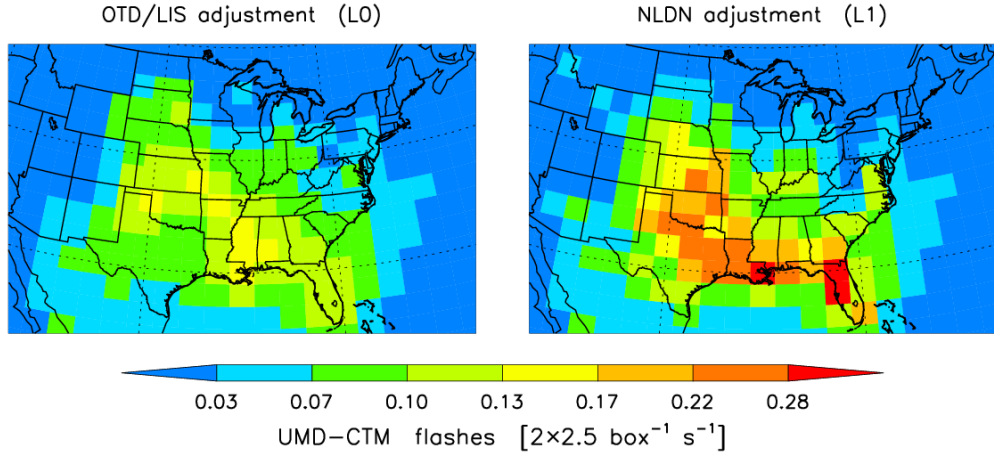


Figure 9. Early summer (1 June to 17 July) 2004 model flash rates. (left) Flash rates are adjusted to match OTD/LIS Low Resolution Time Series flash rates in simulation L0. (right) Flash rates are adjusted to match the NLDN-based total IC + CG flash rates over the CONUS (land only) in simulation L1. The NLDN-based model flash rates for early summer 2004 differ slightly from the NLDN-based observed flash rates (right panel in Figure 7) because the scaling is done on a month by month basis while this figure depicts a 1.5 month period (1 June to 17 July).

3.3.2 UMD-CTM Comparison With Observations

3.3.2.1 Comparison With DC-8 in Situ Measurements During INTEX-A

The INTEX-A field mission was conducted in summer 2004 (1 July to 15 August 2004) and focused on quantifying and characterizing the summertime inflow and outflow of pollution over North America and the western Atlantic [Singh *et al.*, 2006]. INTEX-A was an important component of the coordinated multiplatform atmospheric chemistry field program called ICARTT [Fehsenfeld *et al.*, 2006]. Here we use observations from NASA's DC-8 aircraft.

Regional lightning is the dominant source of upper tropospheric NO_x and can lead to O₃ increases of 10 ppbv or more in the UT [e.g., DeCaria *et al.*, 2005]. Deep convection and lightning were important factors during INTEX-A [Bouscerez *et al.*, 2007; Hudman *et al.*, 2007; Singh *et al.*, 2007]. Backward trajectories [Fuelberg *et al.*, 2007] indicated that the DC-8 often sampled lightning-influenced air, which makes summer 2004 an ideal test bed for the lightning parameterization schemes.

We use aircraft (DC-8) observations from all INTEX-A flights (with the exception of Flight 3 over the eastern Pacific) to determine the model biases for the three lightning simulations L0, L1 and L2. The individual flight track profiles are mostly stair step ascents and descents covering large horizontal regions. Details on flight paths are available in work by Singh *et al.* [2006]. Approximately half of the DC-8 samples were taken above 500 hPa (i.e., pressures < 500 hPa). We compare simulated vertical profiles output hourly from the UMD-CTM to 1 min merge aircraft measurements with a focus on the UT model biases. Following the correction

reported by *Ren et al.* [2008], observed OH values are scaled up by a factor of 1.64. To ensure a regionally representative signal, we remove biomass burning plumes ($\text{HCN} > 500 \text{ pptv}$, $\text{CH}_3\text{CN} > 225 \text{ pptv}$, or $\text{CO} > 99\text{th percentile}$), stratospheric air ($\text{O}_3/\text{CO} > 1.25 \text{ mol mol}^{-1}$) and fresh pollution plumes ($\text{NO}_x/\text{NO}_y > 0.4 \text{ mol mol}^{-1}$, or if NO_y is not available, $\text{NO}_2 > 4 \text{ ppbv}$ and height $< 3 \text{ km}$) from observations [*Hudman et al.*, 2007]. This filtering excludes 8% (fresh pollution), 7% (biomass burning) and 3% (stratospheric air) of the DC-8 data, including some samples with a strong lightning NO signal. While the stratospheric filter only removes 3% of samples, it has the largest impact on UT O_3 biases. We sample the UMD-CTM at the locations and times of DC-8 filtered measurements using nearest neighbor values and interpolating to DC-8 heights.

Figure 10 compares simulated and measured mean vertical distributions of NO , O_3 , CO , HNO_3 , NO_x , OH , PAN and NO_y . First, we analyze the UMD-CTM biases from the standard simulation (L1). Simulated NO and NO_x profiles are C-shaped, reflecting the partitioning of LNO_x in the vertical [Pickering *et al.*, 1998] and the anthropogenic source near the surface. Biases are largest in the UT. NO is underestimated throughout the column (30%–60% too low at 500–300 hPa and 80% too low above 300 hPa). NO_x is underestimated by 20%–50% at 500–300 hPa and by 80% above 300 hPa. The simulation with doubled lightning NO production per flash (L2) decreases biases for both NO and NO_x to 10%–30% at 500–300 hPa and to 60% above 300 hPa; NO_x agrees well with measurements below 300 hPa.

O_3 is overestimated in the lower troposphere by 15 ppbv, but this bias drops to 9.6 ppbv above 500 hPa. Doubling the lightning NO source (simulation L2) increases

the bias to 12.3 ppbv. A 2–3 ppbv increase in upper tropospheric O₃ resulting from a doubling of the source is also seen at IONS sites (Figure 11). The largest impact is seen near (Houston, Texas, and Huntsville, Alabama) and downwind (Wallop Island, Virginia, and Sable Island, Nova Scotia) of frequent thunderstorms. The UMD-CTM also shows a considerable low bias of 20% for CO throughout the column compared to aircraft measurements. CO is not sensitive to different LNO_x sources. Upper tropospheric OH is highly sensitive to LNO_x, which can be seen in the clear separation of the L0, L1 and L2 profiles. Observations indicate that OH concentrations increase with altitude; this slope is best captured in the L2 simulation. Mean absolute values of bias above 500 hPa are 0.11 pptv and 0.07 pptv for L1 and L2, respectively.

HNO₃ during INTEX-A was measured by the California Institute of Technology (CIT) and the University of New Hampshire (UNH). HNO₃ is often depleted in the free troposphere because of scavenging during convection but can increase downwind of convection due to oxidation of NO₂. HNO₃ is highly sensitive to lightning; we see a larger change from L1 to L2 simulated profile than for PAN, consistent with *Hudman et al. [2007]* and *Labrador et al. [2005]*. Variability of HNO₃ in the lower troposphere is larger than in the UT and is associated with variability of NO_x. The simulated HNO₃ is generally overestimated with respect to both the CIT (Figure 10) and UNH (not shown) data sets. The CIT observed about 40% more HNO₃ above 500 hPa than the UNH, leading to better agreement with the model. HNO₃ is overestimated likely because of NO_x oxidation being too rapid or wet removal being insufficient in the model or both. Overall, despite NO_x

underprediction, NO_y is overpredicted below 300 hPa because both PAN and HNO_3 are overestimated with respect to the in-situ measurements. Most of NO_y high bias above 500 hPa is due to PAN overestimation (by up to 0.2 ppbv and 0.3 ppbv in the L1 and L2 simulations, respectively). NO_x underestimation and NO_y overestimation could indicate a fundamental problem with the UT NO_y chemistry. *Henderson et al.* [2010] evaluated seven different chemical mechanisms. They found that each mechanism overestimates the rate at which NO_x is converted to NO_z ($\text{NO}_y - \text{NO}_x$), i.e., the rate at which NO_x ages. They also suggested several updates and fixes to various mechanisms to slow down this conversion rate.

In summary, doubling the lightning NO production per flash reduces NO , NO_x and OH biases in the UT. However, it increases the biases for O_3 and PAN slightly (by factors of 1.3 and 1.2, respectively) and for HNO_3 and NO_y substantially (factors of 2.8 and 2.0, respectively). In spite of increased O_3 biases (by 2.7 ppbv above 500 hPa, L1 versus L2), the NO_x profile from the L2 simulation agrees well with DC-8 measurements below 300 hPa but is low biased by 60% above 300 hPa. Because the lightning sources in L1 and L2 simulations bracket the emissions of other investigators (Table 2) and because of the mixed results from comparison with aircraft measurements during INTEX-A (NO_x underestimated; NO_y and O_3 overestimated) as to which lightning source is most realistic, we complement the L1 results by examining the impact of doubled lightning NO production per flash (L2).

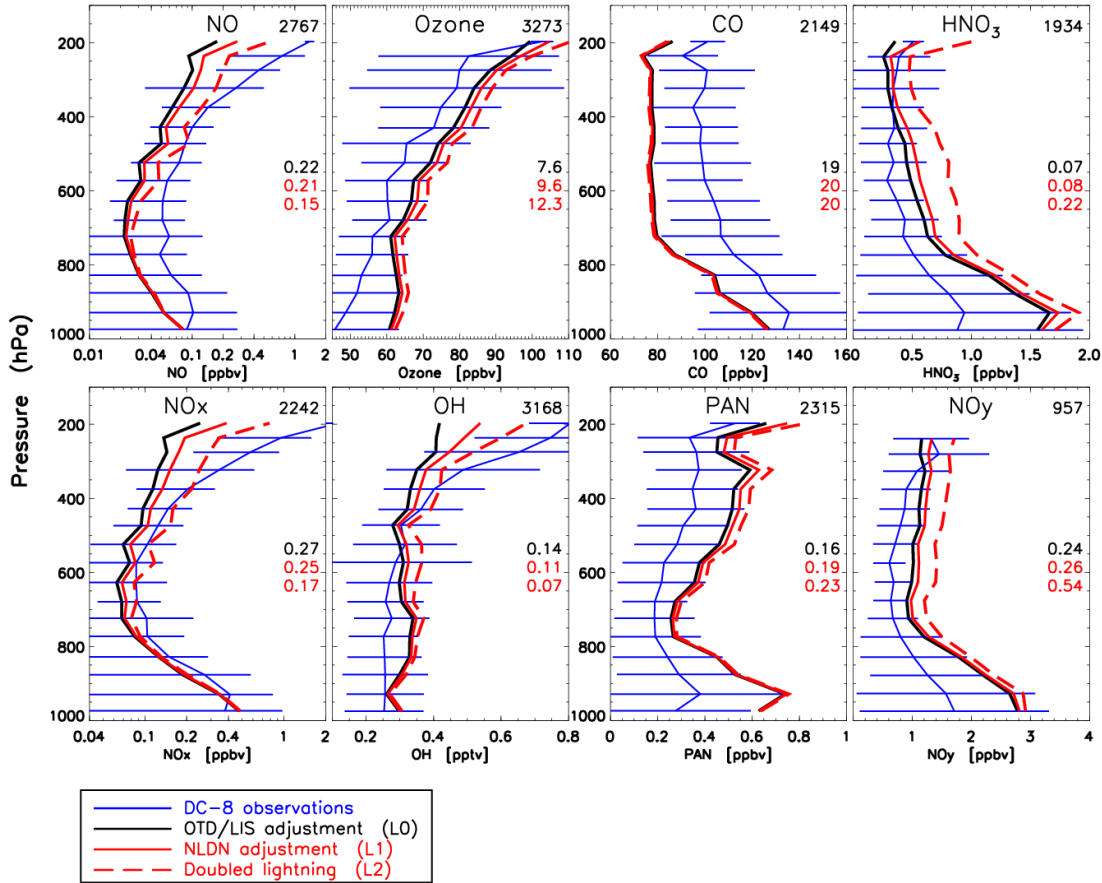


Figure 10. Mean vertical profiles of NO, O₃, CO, HNO₃, NO_x, OH, PAN and NO_y. Measurements from the DC-8 aircraft (blue) are compared to UMD-CTM results from the L0 (black), L1 (red) and L2 (dashed red) simulations. The 1 min average measurements are compared to hourly UMD-CTM output sampled along the flight tracks. NO_y is estimated as the sum of its main oxidation products (NO_x, PAN, and HNO₃). We use here HNO₃ data obtained by science team from California Institute of Technology. Horizontal bars indicate standard deviations on the observations in each 50-hPa bin. The number of filtered observations above 500 hPa is listed in the upper-right corner of each plot. The absolute values of the bias (model minus observation) averaged from 50-hPa bins above 500 hPa are listed in the middle right part of each plot: L0 bias (top value), L1 bias (center value), and L2 bias (bottom value). Note the logarithmic scale for NO and NO_x.

3.3.2.2 Comparison With IONS Ozone Soundings

The INTEX Ozonesonde Network Study [*Thompson et al.*, 2007b] provided several hundred ozonesonde launches throughout the continental United States and Canada during the INTEX-A period. In this section, we analyze the IONS soundings from the INTEX-A period. At IONS sites (Trinidad Head, Houston and the R/V R. H. Brown), soundings were made daily between noon and 1400 local time to capture overpasses of the Aqua and Aura satellites. The remaining stations launched midday 1–3 times per week, except for Sable Island with 1900 local time launches [*Thompson et al.*, 2007b]. In our analysis, we filter out mixing ratios > 200 ppbv in the measurements and model results to minimize the effects of extreme values, which are likely of stratospheric origin [*Choi et al.*, 2008].

Figure 11 shows the mean vertical profiles of O_3 as measured by IONS and calculated from L1 and L2 hourly output for July and August 2004. In general, the UMD-CTM overestimates the O_3 concentration measurements. However, in the UT, the mean UMD-CTM profiles agree well (the best agreement is for Beltsville and R/V R. H. Brown) and are within one standard deviation of the mean ozonesonde soundings. Largest biases (9.8–11.6 ppbv above 500 hPa) are seen at Boulder, Sable Island and Wallops Island. Sounding-to-sounding variations in UT O_3 are not well captured. The explained variance varies from near zero at Houston to 46% off the east coast, as indicated in Figure 11.

The simulation with doubled lightning NO production per flash (L2) produces more O_3 in the free troposphere. O_3 biases are therefore increased in the L2 simulation by up to 3.0 ppbv (above 500 hPa), depending on the site. The largest

impact is seen at the locations that had frequent thunderstorms (Houston and Huntsville) as well as in aged thunderstorm outflow (Wallops Island and Sable Island), whereas at Trinidad Head and Boulder, the doubling of lightning source has very little impact.

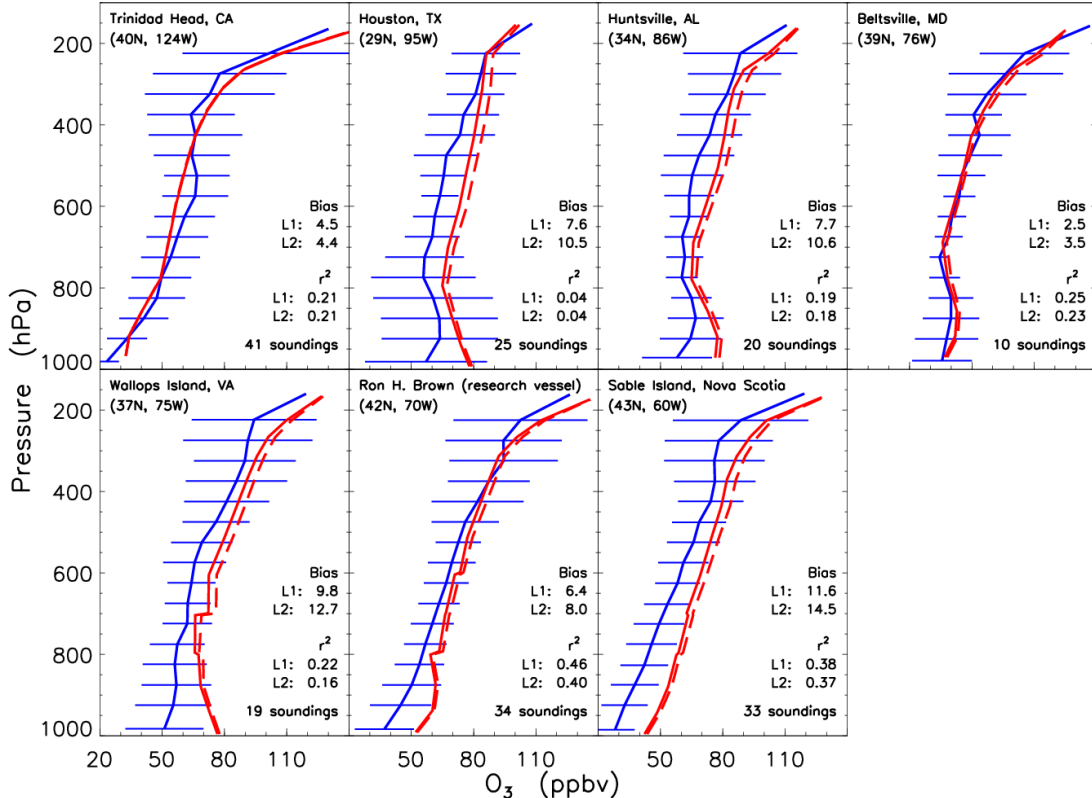


Figure 11. Mean profiles as observed from IONS ozonesondes (blue) and simulated with the UMD-CTM for July and August 2004. Results from the standard simulation (L1: red) and the simulation with doubled lightning NO per flash (L2: red dashed) UMD-CTM simulations are shown. Horizontal bars indicate standard deviations in each 50-hPa bin. The explained variances (r^2) between observed and simulated O₃ from one sounding to the next and the absolute values of the bias (model minus observation) averaged from 50-hPa bins above 500 hPa are listed in the bottom right corner of each plot.

3.3.2.3 Comparison With SCIAMACHY NO₂ Columns

The impact of reduced NO_x emissions on NO₂ columns in the ORV (the region dominated by power plants that had implemented controls) is evident from space [Kim *et al.*, 2006]. Data from the high resolution ($30 \times 60 \text{ km}^2$) SCIAMACHY instrument (Scanning imaging absorption spectrometer for atmospheric chartography), onboard ENVISAT, became available in August 2002. It detects the sunlight reflected from the Earth or scattered in the atmosphere [Richter *et al.*, 2005]. In nadir mode, SCIAMACHY observes the total NO₂ column from which the stratospheric column, as derived over the Pacific sector, is subtracted to get the tropospheric column. The measurements were screened to use only pixels with less than 30% cloud fraction.

In Figure 12, we determine whether changes in satellite-observed and model-calculated NO₂ columns (L1 simulation) are consistent with the updated emission inventories. We sample the UMD-CTM by following daily satellite tracks (ENVISAT overpasses the ORV at 0930–1000 local standard time). The UMD-CTM tropospheric NO₂ columns are calculated by integrating the columns from the surface to the GEOS-4 CERES tropopause. The UMD-CTM columns are interpolated in space and time to the SCIAMACHY pixels and times using the outputs at 1200 and 1800 UTC. We composite the observed and simulated columns onto a $0.54^\circ \times 0.70^\circ$ grid, corresponding to approximately $60 \times 60 \text{ km}^2$ (Figures 12a, 12b, 12d, and 12e). By temporally averaging the UMD-CTM output at this resolution (each grid box includes ~8 clear sky days during August 2002 and ~6 clear sky days during August 2004) we are able to obtain more detail than can be obtained from $2^\circ \times 2.5^\circ$ UMD-CTM.

However, the UMD-CTM even when averaged in this fashion is unable to resolve the maxima observed by SCIAMACHY over polluted urban areas (e.g., Chicago).

The observations from SCIAMACHY show that major NO₂ plumes over the northeastern United States are of substantially smaller magnitude in 2004 than 2002, consistent with the emission reductions due to the NO_x SIP Call. In August 2002, nearly one third of U.S. power plant NO_x emissions were from the ORV region (larger box in Figure 12a), while in August 2004 they comprised less than one fifth due to implemented emission controls. CEMS data show that power plant NO_x emissions from this region were reduced by ~50% between August 2002 and 2004. The observed NO₂ columns over the ORV were reduced by 22% on average from 2002 to 2004. A smaller observed reduction is expected because of transport from regions where emissions reductions were smaller and because SCIAMACHY detects all types of NO₂, not just that resulting from power plant emissions. Similar reductions of 19% are seen in the UMD-CTM (Figures 12d and 12e). Reductions in observed columns were also seen over the northeastern United States (smaller box in Figure 12a), which is downwind of the ORV power plants. The modeled reductions in this region were 11%, while observed reductions were 20%. The difference in reductions between SCIAMACHY and the model in this region could indicate that NO_x emissions from other sources also decreased between 2002 and 2004; however, this difference may also indicate that the medium-range transport of NO₂ is underpredicted by the UMD-CTM. *Gilliland et al.* [2008] noted that CMAQ underestimated the response of O₃ to changes in emissions partly because the transport of O₃ and its precursors was underestimated. *Godowitch et al.* [2008] in a simulation

with CMAQ also underestimated the improvement in air quality between summers 2002 and 2004. In 2002, there was a 2 ppbv low bias whereas 2004 had a 4 ppbv high bias in 8 h O₃.

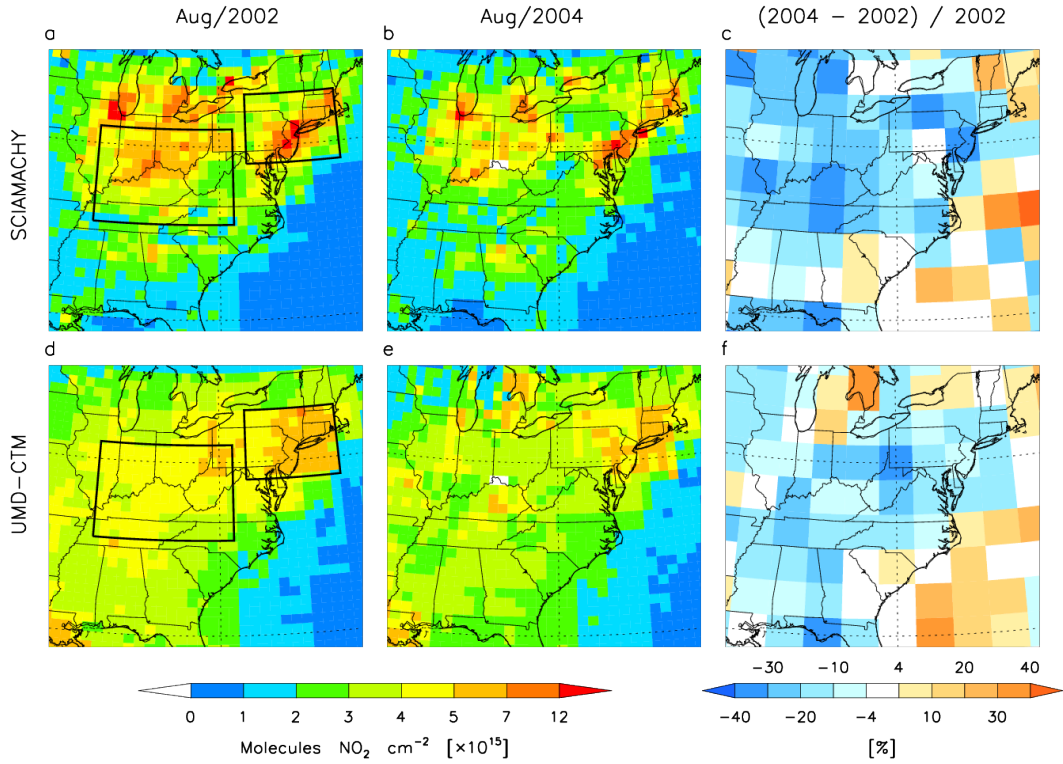


Figure 12. Comparison between (a, b) SCIAMACHY-retrieved and (d, e) UMD-CTM-simulated mean tropospheric NO_2 vertical columns (10^{15} molecules $\text{NO}_2 \text{ cm}^{-2}$) composited from all overpasses with cloud fraction < 0.3 over the eastern United States in (left) August 2002 and (middle) August 2004. The UMD-CTM is sampled at each SCIAMACHY pixel. Both observed (Figures 12a and 12b) and modeled (Figures 12d and 11e) columns are composited to a $0.54^\circ \times 0.70^\circ$ (about $60 \times 60 \text{ km}^2$) grid which is close to the native resolution of SCIAMACHY. In the ORV region (indicated by the larger box on the left), SCIAMACHY observed reduction from 4.27 to 3.32 on average between 2002 and 2004, whereas simulated columns were reduced from 4.24 to 3.43 (all values in units of $10^{15} \text{ NO}_2 \text{ molecules cm}^{-2}$). (c, f) Relative change (%) between 2002 and 2004 but at the $2^\circ \times 2.5^\circ$ resolution.

3.3.2.4 Comparison With Ozone Observations From Ground-Based AQS Sites

The AQS (Air Quality System) is an EPA database (<http://www.epa.gov/ttn/airs/airsaqs>) that provides ambient concentrations of air pollutants at monitoring sites, primarily in cities and towns. We use daily maximum 8 h O₃ (8 h O₃) as the metric for our comparisons, since it is important from a regulatory perspective. The 2008 National Ambient Air Quality Standard (NAAQS) for 8 h O₃ is 75 ppbv.

Figure 13 shows time series of 8 h O₃ from the ORV region. We see that the UMD-CTM captures well the periods with large day-to-day variability. Most of the variance ($r^2 > 0.5$) in summer 2002 and in late summer 2004 is explained by the model. In early summer 2004, observed day-to-day variability is smaller, and the UMD-CTM is unable to capture these subtle changes in surface O₃. It is likely that the correlation between simulated and observed 8 h O₃ might be improved if daily CEMS data were used in the model instead of monthly CEMS data. In the ORV, 8 h O₃ is simulated with mean high biases of 16.5 ppbv and 24.0 ppbv in summer 2002 and 2004, respectively. The difference between these biases is likely to decrease by up to 3 ppbv (see section 3.2.3) if isoprene emissions are allowed to respond to temperature variations. Despite this mean high bias, O₃ concentrations at numerous AQS sites were slightly underpredicted during the highest O₃ episodes that occurred in summer 2002. Similarly, in the rest of the eastern United States (not shown), the UMD-CTM captures the O₃ variations reasonably well ($r^2 > 0.5$) with biases of 10–20 ppbv seen over the Great Lakes (Wisconsin and Michigan), New York State and New England and with 20–30 ppbv biases seen in the southern United States. Overprediction of surface O₃ in the eastern United States during summer is common

in many CTMs. *Reidmiller et al.* [2009], as part of the Hemispheric Transport of Air Pollution project, 2007 (<http://htap.org>), showed that the mean multimodel (16 CTMs) bias was 10–20 ppbv. Some of the bias is due to the spatial averaging of emissions in a model grid box; dilution of NO_x emissions to a 2° × 2.5° grid leads to greater O₃ production than at finer resolutions [*Sillman et al.*, 1990; *Park et al.*, 2004b]. Additional uncertainty is introduced by the treatment of isoprene emissions (BEIS versus MEGAN) and isoprene-nitrate chemistry in chemical mechanisms.

Overall, the combined effects of changes in meteorology and emissions had a great impact on 8 h O₃ concentrations in the northeastern United States. Observed 8 h O₃ concentrations were reduced by 14 ppbv in the ORV on average from summer 2002 to 2004. Reductions of 7 ppbv were seen in the UMD-CTM (sampled at the locations of the AQS sites).

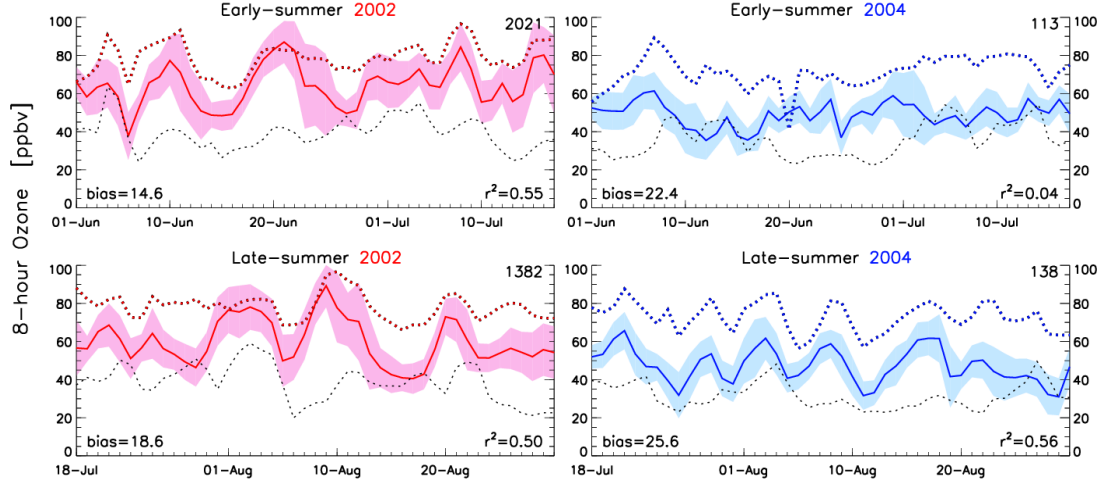


Figure 13. The 8 h O₃ time series constructed from 155 AQS sites located in the ORV region (indicated by the larger box in Figure 12a) in summer (left) 2002 and (right) 2004. The shaded area around the mean AQS-measured values (red and blue solid lines) indicates the standard deviation. The number of current NAAQS exceedances (8 h O₃ > 75 ppbv) for each month is in the top right corner of each plot. The UMD-CTM (dotted lines) is sampled at the locations of the AQS sites. The 8 h O₃ from the sensitivity simulation with the anthropogenic emissions from North America turned off (Table 1) is indicated by black dotted lines. The UMD-CTM bias is listed in the bottom left corner of each plot. The explained variance r^2 between time series of observed and simulated O₃ is in the bottom right corner of each plot.

3.3.3 Ozone Enhancements From NA Anthropogenic Emissions and Lightning

We compare the relative effects of modeled O₃ enhancements from NA anthropogenic emissions and NA lightning for summer 2004, focusing on long-range transport and continental outflow. Although not strictly true, because of the nonlinear response of O₃ to NO_x emissions, the lightning (anthropogenic) enhancement is

diagnosed as the difference between simulations with and without the LNO_x (ANO_x) source. These results are then compared to similar simulations for summer 2002, allowing us to quantify the impact of changes in meteorology and NA lightning between summers 2002 and 2004 on long-range transport and continental outflow as well as the relative radiative impact.

Figures 14a, 14b, 14d, and 14e show the O₃ enhancements from NA anthropogenic emissions and lightning in early summer 2004. Anthropogenic emissions produced the greatest O₃ enhancements near the surface (up to 35 ppbv over the eastern United States, as seen in Figure 14a), whereas lightning had the greatest impact in the UT (up to 16 ppbv over the Gulf Coast and the western North Atlantic, as seen in Figure 14e). *Hudman et al.* [2009], using the GEOS-Chem, compared the O₃ enhancements from NA anthropogenic emissions and lightning during INTEX-A. They also showed that the BL enhancements were mainly anthropogenic and that lightning had the greatest impact in the UT. Convectively lifted precursors and LNO_x enhanced the O₃ production, especially at higher altitudes. We see similar enhancements as *Hudman et al.* [2009] over North America and in the continental outflow, near-surface enhancements from anthropogenic emissions of 3–5 ppbv over western Europe, and UT (400–200 hPa) enhancements from lightning of 9–12 ppbv over the eastern subtropical Atlantic (with 9 ppbv contour reaching over Spain). In contrast with *Hudman et al.* [2009], we also examine the 2002 to 2004 variations in O₃ enhancements from lightning (Figures 14c and 14f). From 2002 to 2004, there is an increase in the contribution of lightning to eastern U.S. O₃, both near the surface (Figure 14c) and in the UT (Figure 14f).

Figure 15 shows the tropospheric O₃ columns during early and late summer 2004 and the enhancements from anthropogenic emissions and lightning NO emissions. In late summer 2004, the warm conveyor belt was especially active [Kiley and Fuelberg, 2006], enhancing the transport of anthropogenic O₃ along the U.S. east coast. In addition, stronger southerly winds relative to early summer (Figure 6c versus Figure 6a) pushed the anthropogenic and lightning plumes to more northern latitudes. Maximum anthropogenic enhancements were ~11 DU, which represented ~21% of the total tropospheric column. Maximum lightning enhancements were ~9 DU (Figures 15c and 15f), which represented ~18% of the total tropospheric column. Doubling the LNO_x source over North America in the UMD-CTM produces an additional 4 ppbv of O₃ in the UT (400–200 hPa) compared to lightning enhancements from L1 simulation, thus adding ~2 DU to the tropospheric column. Doubled lightning (L2) produces therefore ~11 DU, which is the same as produced from anthropogenic emissions. The relatively small increase from ~9 to ~11 DU, when going from 240 NO mol flash⁻¹ to 480 NO mol flash⁻¹ is due to the nonlinear response of O₃ enhancements to LNO_x emissions. Similarly, in downwind regions over the northern Atlantic and western Europe, the early summer O₃ enhancements in the L2 simulation exceed the L1 enhancements by only 33% despite a doubling of LNO_x emissions from North America. In contrast, Wu *et al.* [2009] found no significant nonlinearity of O₃ response to anthropogenic NO_x emissions in the downwind regions from North America.

Shifting our focus to the summer-to-summer change, Figures 16a and 16c indicate substantial differences between 2004 and 2002 in O₃ enhancements due to

lightning in the continental outflow, especially for early summer. Early summer 2004 lightning contributed to 2–6 ppbv more O₃ in the UT (400–200 hPa) over the subtropical North Atlantic, southern Europe and the Middle East when compared to 2002 (Figure 14f), enhancing the tropospheric column by 1.0–3.5 DU. Over the subtropical North Atlantic (20°N–45°N), increased NA lightning (and changes in meteorology) between early summer 2002 and 2004 explain about two thirds of the increase in tropospheric O₃ column between 2002 and 2004 (not shown). During late summer both years had similar lightning flash rates; however, meteorological conditions in 2004 were less favorable for O₃ formation [see also *Cooper et al.*, 2009; *Allen et al.*, 2010] and led to 1–4 ppbv less O₃ in the UT over the eastern United States than in 2002 (not shown). However, the tropospheric column over the eastern Atlantic, Europe and northern Africa had up to 1.2 DU more O₃ from lightning in 2004 than 2002 (Figure 16c), reflecting more efficient transport over the Atlantic in both early and late summer 2004. Later in the summer (both years), the LIS sensor observed enhanced flash rates over Mexico, indicating the increased lightning activity and deep convection associated with the North American Monsoon [*Li et al.*, 2004; *Gao et al.*, 2007]. Note the intensification of the O₃ enhancement over Mexico and the convective outflow over the Gulf of Mexico in late summer (Figure 15c versus Figure 15f).

To compare the impact of increased NA lightning (and changes in meteorology) between 2002 and 2004 with the impact of emission reductions resulting from the NO_x SIP Call, we did a sensitivity simulation with 2002 NO_x emissions (when power plant emissions were not as tightly regulated) and 2004

meteorology and lightning. While decreases in surface O₃ layer over the eastern United States due to the NO_x SIP Call were substantial, decreases in the tropospheric column were small (Figures 16b and 16d). Columns were reduced by < 0.5 DU due to the NO_x SIP Call over the North Atlantic in both early and late summer (with the -0.1 DU contour reaching Spain, Italy and southern France). During the early summer in the region where the emission reductions (between 2002 and 2004) had the largest impact on O₃ column over the North Atlantic (30°N–50°N), the increase in O₃ column due to changes in lightning and meteorology exceeded the decrease due to reduced anthropogenic emissions by a factor of 7. In late summer, differences in flash rates between 2002 and 2004 were much smaller. Consequently, the late summer changes in O₃ column due to changes in lightning and meteorology were also smaller in the second half of the summer, and the change in O₃ column due to lightning and meteorology was comparable to the change due to reduced anthropogenic emissions but opposite in sign. Comparing the changes in surface O₃ concentrations between early summer 2004 and 2002, we see that the reductions due to the NO_x SIP Call were up to 5 ppbv with decreases of 1–3 ppbv downwind of the ORV region, while increased NA lightning NO emissions resulted in a 0.3–1.4 ppbv increase in surface O₃ over the same regions (Figure 17). Unlike NA anthropogenic emissions, which continue to show a downward trend over recent years, there is no clear trend in lightning flash rate and the increases in Figure 17a are only a result of interannual variability.

Ozone enhancements can be found downwind of NO₂ enhancements: O₃ enhancements in Figures 15b, 15c, 15e, and 15f extend more eastward than

corresponding NO₂ enhancements in Figure 18. The same is true for the summer-to-summer changes (Figures 16a and 16c versus Figures 18d and 18h).

Lightning enhancements are primarily in the UT, where previous studies [e.g., *Lacis et al.*, 1990] have shown O₃ to be most effective as a greenhouse gas. *Choi et al.* [2009], using the regional chemistry transport model REAM for the period of June–July 2005, showed that in the immediate convective outflow, the radiative effects of O₃ produced from LNO_x were up to three times as large as those from anthropogenic emissions. In our analysis, we examine the larger-scale radiative impact (defined in section 3.2.5) due to O₃ produced from anthropogenic emissions (RF_{anthro}) and from lightning (RF_{LNOx}). Figure 19 shows that RF_{anthro} ranged from 0.15–0.30 W m⁻² in the continental outflow across the North Atlantic, whereas the RF_{LNOx} ranged from 0.20–0.40 W m⁻² (0.25–0.50 W m⁻² for doubled LNO_x source) over the same area in early and late summer 2004. The RF_{LNOx} also exceeded RF_{anthro} over southern Europe and northern Africa in both early and late summer 2004. We find that, in early summer 2004, the RF_{LNOx}/RF_{anthro} ratio ranged from 0.3 at higher latitudes of the North Atlantic to ~1.6 over the subtropical North Atlantic, with a maximum of 2.3 over the southern Gulf of Mexico (Figure 20). Doubling the LNO_x source has the greatest impact on this ratio over the western subtropical North Atlantic, where the RF_{LNOx}/RF_{ANTHRO} ratio increases from 1.6 to 2.1.

We see the largest impact from lightning after the onset of the North American Monsoon (Figure 19e), which is reinforced by the upper-level anticyclone centered over Mexico [*Cooper et al.* 2009, Figure 2]. Although the RF due to lightning is greater in late than early summer in the immediate convective outflow

over Mexico and the Gulf of Mexico, it is slightly less over Europe and northern Africa in late summer 2004. This indicates that the convective outflow recirculated in this upper level anticyclone centered over Mexico in late summer, allowing more O₃ production over the southern United States and the Gulf of Mexico, as discussed by *Li et al.* [2005], prior to transport across the Atlantic.

The spatial pattern of summer-to-summer changes in RF (Figures 19c and 19f) is similar to that of summer-to-summer changes in the tropospheric O₃ column. The 50% increase in flash rate between early summer 2002 and 2004 over the United States corresponds to 30% increase in RF due to LNO_x over the areas with enhancements exceeding 5 DU. The impact of power plant reductions on RF (diagnosed from the sensitivity simulation with 2002 NO_x emissions and 2004 meteorology and lightning) was much smaller than that seen in Figures 19c and 19f. The RF values over the North Atlantic decreased by <0.01 W m⁻² because of emissions reductions (not shown). Of course, the emission reductions were designed to address violations in ambient air quality and not to reduce tropospheric O₃ columns and resulting changes in RF.

In early summer 2004, mean normalized RF per unit of added O₃ column, over the areas with enhancements exceeding 5 DU, is 0.027 W m⁻² DU⁻¹ due to NA anthropogenic enhancements and 0.047 W m⁻² DU⁻¹ due to NA lightning enhancements (average from L1 and L2 simulations). For comparison with previous studies we use *Gauss et al.* [2003], who used 11 different climate models to estimate the (longwave, clear sky) normalized instantaneous radiative forcing. They gave a range of 0.042–0.052 W m⁻² DU⁻¹ for the global annual averages of normalized

radiative forcing due to changes in tropospheric O₃ between 2000 and 2100. The annual average of normalized radiative forcing due to increasing anthropogenic emissions over the next century is predicted to be greater than that due to present-day NA anthropogenic emissions and is comparable with RF due to NA lightning. Noteworthy is also *Worden et al.* [2008], who, using TES (Tropospheric Emission Spectrometer) measurements for cloud-free ocean conditions, obtained an estimate of 0.055 W m⁻² DU⁻¹ (annual mean from 45°S to 45°N) for the sensitivity to UT (500–200 hPa) O₃, thus providing an important observational constraint for both natural and anthropogenic O₃.

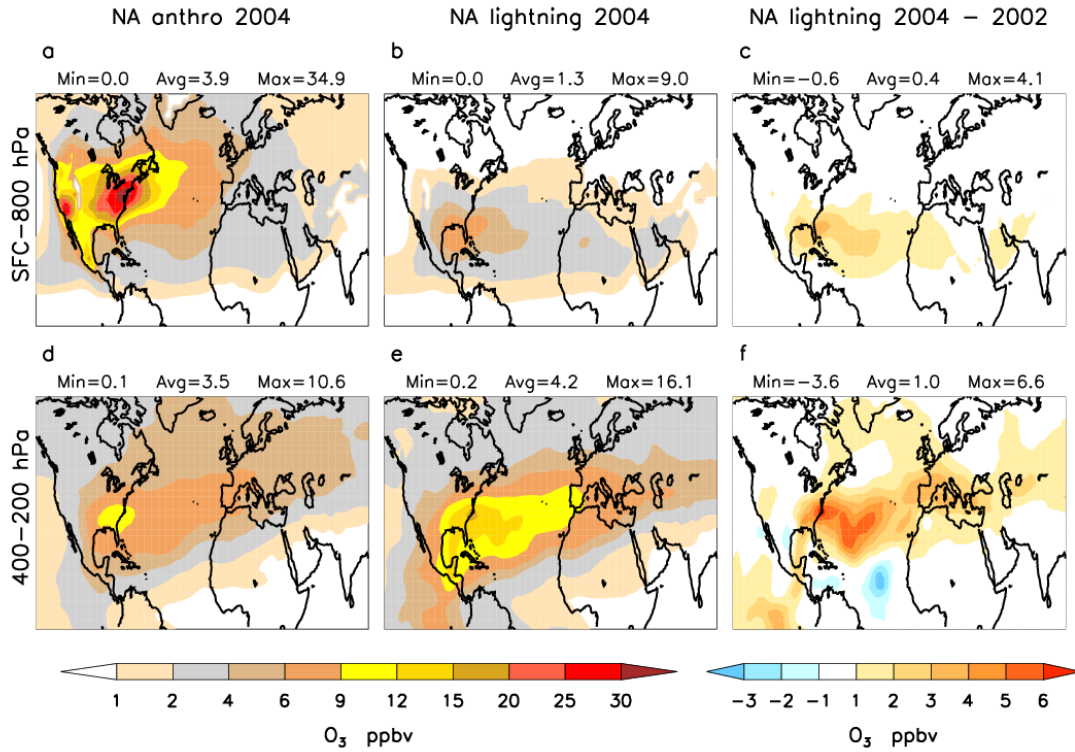


Figure 14. Early summer (1 June to 17 July) O₃ enhancements from North American (**a, d**) anthropogenic and (**b, e**) lightning emissions as diagnosed by simulation L1 and the sensitivity simulations with the respective sources turned off (Table 1). (**c, f**) Difference between 2004 and 2002 due to North American lightning. The values are averaged in (top) the lower troposphere (from the surface to 800 hPa) and (bottom) the upper troposphere (400–200 hPa). Minima, averages and maxima are listed in the title of each plot.

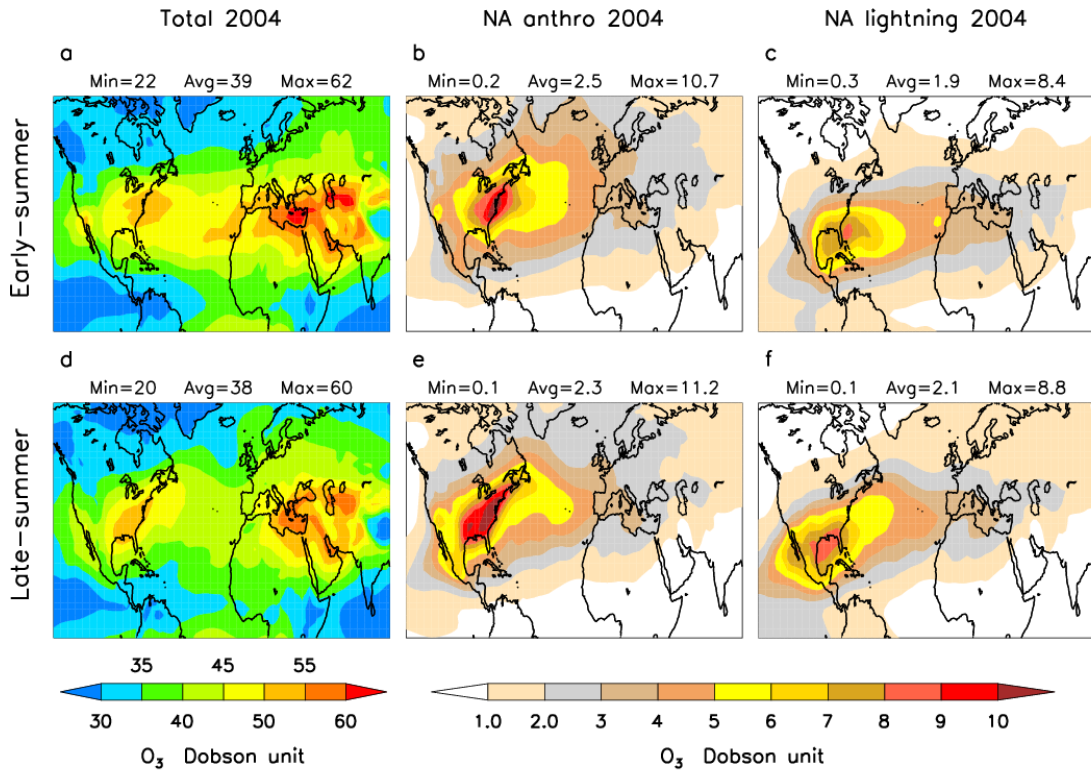


Figure 15. (a, d) Tropospheric O_3 columns and their enhancements due to North American (b, e) anthropogenic emissions and (c, f) lightning as diagnosed by simulation L1 and the sensitivity simulations with respective sources turned off (Table 1). The values are (top) early summer (1 June to 17 July) mean, and (bottom) late summer (18 July to 31 August) mean for 2004. Minima, averages and maxima are listed in the title of each plot. Corresponding NO_2 columns are in Figures 18a–17c and 18e–18g.

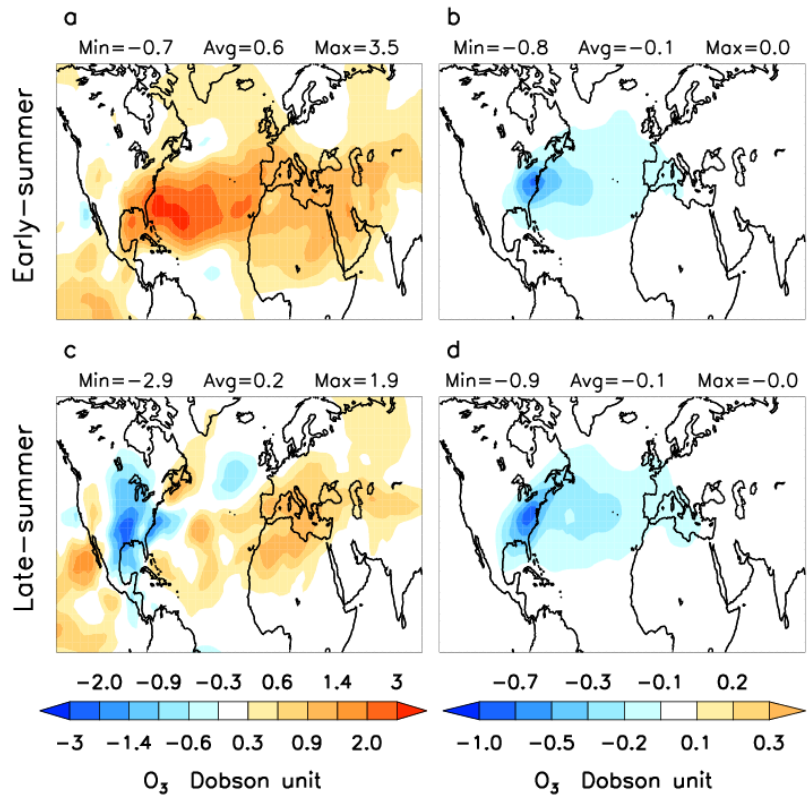


Figure 16. (left) The impact of changes (2004 minus 2002 difference) in North American lightning and meteorology and (right) the impact of NO_x SIP Call reductions on tropospheric O₃ columns as diagnosed by simulation L1 and three sensitivity simulations (Table 1), two with the LNO_x source turned off (one for each year) and one with 2002 power plant NO_x emissions and 2004 flash rates and meteorology. The values are (top) early summer (1 June to 17 July) mean and (bottom) late summer (18 July to 31 August) mean. Minima, averages and maxima are listed in the title of each plot.

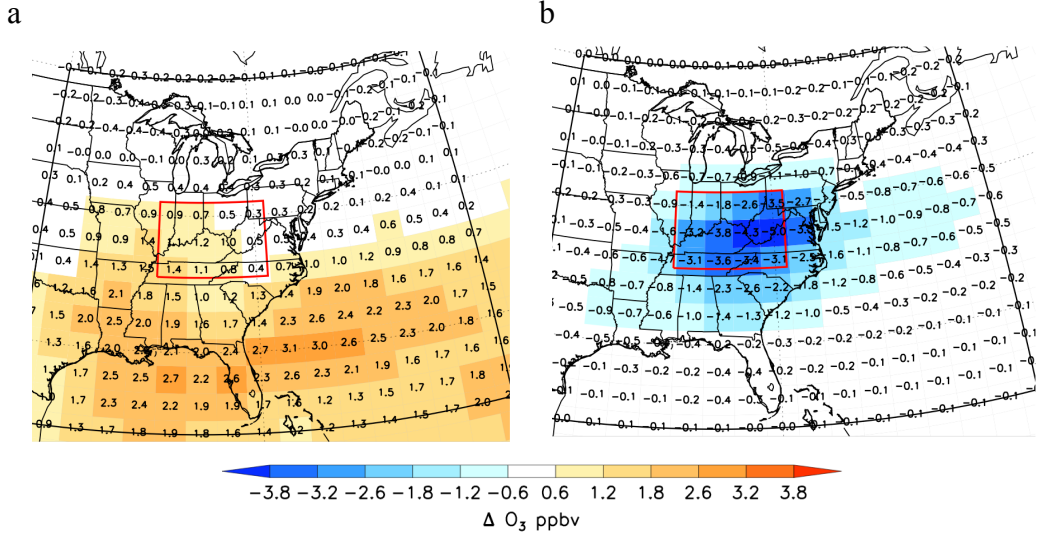


Figure 17. (left) The impact of changes (2004 minus 2002) in North American lightning and meteorology and (right) the impact of NO_x SIP Call reductions on surface layer O₃ concentration. The increase in left figure is diagnosed by simulation L1 and two sensitivity simulations with the LNO_x source turned off (Table 1). The decrease in right figure is diagnosed by simulation L1 and sensitivity simulation with 2002 power plant NO_x emissions and 2004 flash rates and meteorology (Table 1). The values are averaged for early summer (1 June to 17 July) at 18 UTC.

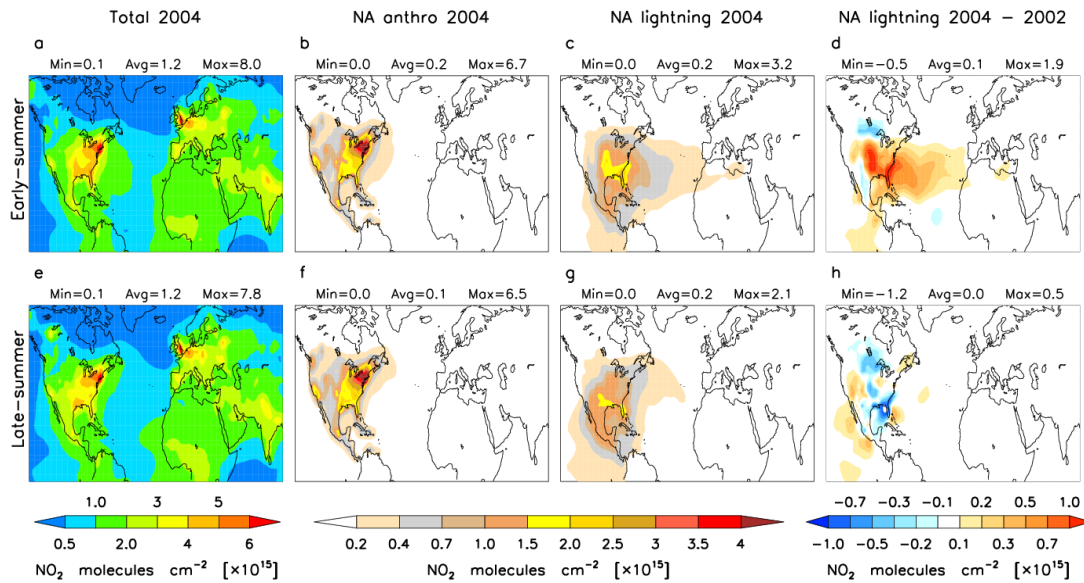


Figure 18. **(a, e)** Tropospheric NO_2 columns and their enhancements due to North American **(b, f)** anthropogenic emissions and **(c, g)** lightning as diagnosed by simulation L1 and the sensitivity simulations with respective sources turned off (Table 1) for 2004. **(d, h)** Difference between 2004 and 2002 due to North American lightning. The values are averages for (top) early summer (1 June to 17 July), and (bottom) late summer (18 July to 31 August). Minima, averages and maxima are listed in the title of each plot.

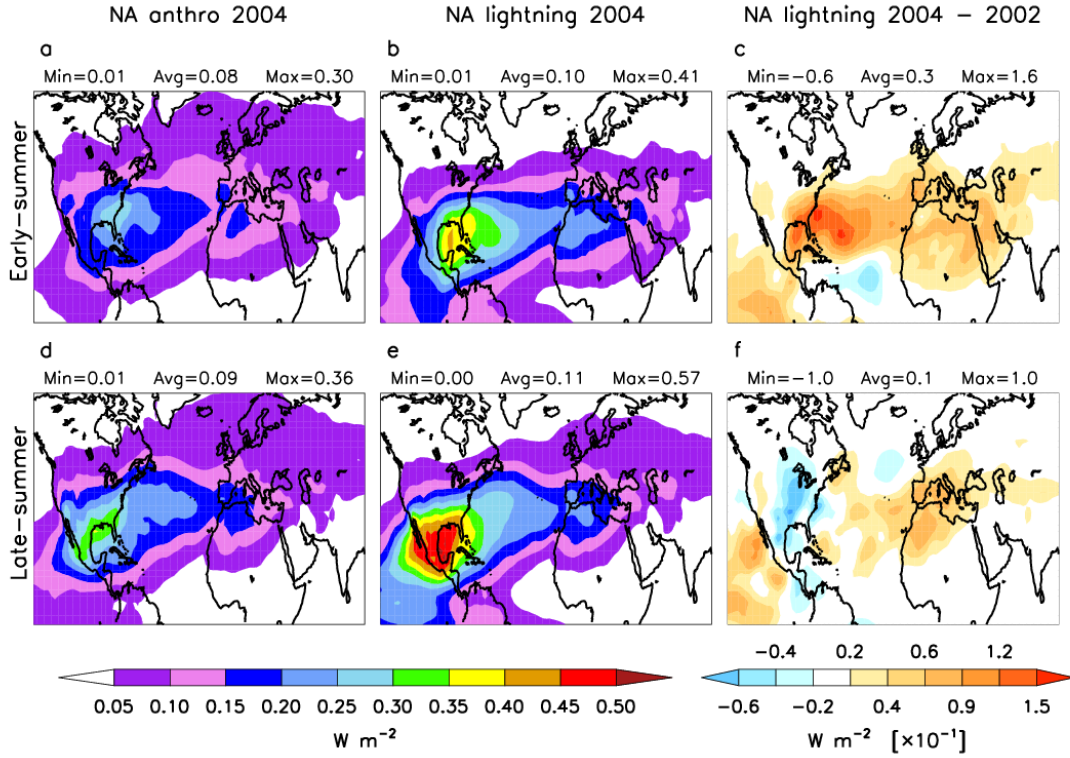


Figure 19. RF (calculated as described in section 3.2.5) for 2004 due to North American (**a**, **d**) anthropogenic emissions and (**b**, **e**) lightning as diagnosed by simulation L1 and the sensitivity simulations with respective sources turned off (Table 1). (**c**, **f**) Difference between 2004 and 2002 due to North American lightning. The values are (top) early summer (1 June to 17 July) mean and (bottom) late summer (18 July to 31 August) mean. Minima, averages and maxima are listed in the title of each plot. Note a factor of 10 smaller units for RF in Figures 19c and 19f.

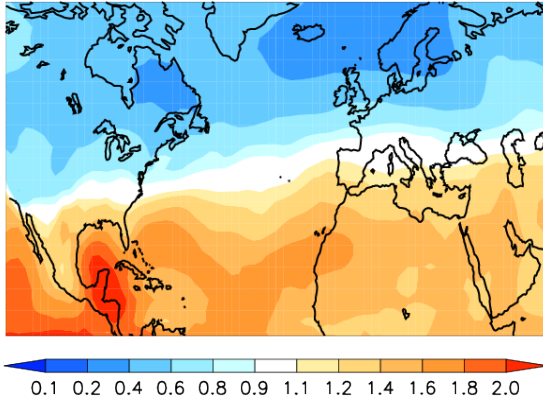


Figure 20. Early summer 2004 (1 June to 17 July) ratio RF_{LNO_x}/RF_{anthro} as diagnosed by the standard simulation and sensitivity simulations with respective sources turned off (Table 1).

3.3.4 Import and Export Fluxes

We calculate the fluxes of NO_x , NO_y , CO and O_3 across the western and eastern NA boundaries for early summer. These fluxes are summed along the longitudes $130^\circ W$ (imports) and $65^\circ W$ (exports) in the region between $25^\circ N$ and $60^\circ N$. We estimate NO_y as the sum of the following oxidation products: NO_x , NO_3 , N_2O_5 , $HONO$, HNO_3 , HO_2NO_2 , PAN and MPAN (methylperoxyacetyl nitrate).

Figure 21a shows vertical profiles of NO_x , NO_y , CO and O_3 fluxes averaged over early summer 2002 and 2004; 2002 imports exceeded 2004 imports for each species. Since we held the Asian anthropogenic emissions constant for both years, the decreased imports (by ~30%) in 2004 compared to 2002 were mainly due to the weaker jet stream over the Pacific. For example the peak zonal winds at 225 hPa were 36 m s^{-1} and 32 m s^{-1} in 2002 and 2004, respectively, although it should be noted that the peak zonal winds do not represent the integrated effect of the entire wind field

over the Pacific. The reduced imports seen in 2004 compared to 2002 motivate us to calculate the difference between exports and imports, hereafter referred to as the net exports. This method allows us to estimate the efficiency of photochemistry over North America by removing the differences in what is imported from what is photochemically produced or emitted over North America. O₃ soundings at the west-coast site of Trinidad Head, CA, indicate that O₃ imports are well simulated (Figure 11 shows a good agreement of ozonesonde-measured O₃ profiles with model-calculated O₃ profiles).

NO_x and NO_y fluxes in this study are similar to those from *Choi et al.* [2008], in which the authors estimated imports and exports from North America in spring 2000 using the regional chemistry transport model REAM. They reported that in May 2000, the NO_x exports peak at 4×10^7 mol d⁻¹. In our study, NO_x exports peak at 2.1– 2.5×10^7 mol d⁻¹ (in early summer 2002 or 2004, Figure 21a). This lower peak could be because of faster photochemical oxidation and slower wind speeds during summer. In addition, CEMS data show that NO_x emissions from the United States were greater in 2000 than 2002 or 2004. North America is a net source of pollution in summer (exports greater than imports throughout the troposphere); this is partially due to stronger westerlies over the western Atlantic than over the eastern Pacific (Figure 6). The total O₃ exports (summed from the surface to 100 hPa) were factors of 2 and 1.4 larger than the total O₃ imports in early summer 2004 and 2002, respectively, whereas in May 2000, the export-to-import ratio was close to 1 [*Choi et al.*, 2008].

Figure 21b indicates that the net exports were larger in early summer 2004 than in 2002. The areas to the left of the net export curves are proportional to the total

mass exported from North America. CO was exported at higher altitudes in 2004 (Figure 21b) which along with enhanced westerlies (Figure 6) led to greater net export than in 2002. In order to determine if differences in biomass burning between 2002 and 2004 had a substantial impact on net exports, we reran the UMD-CTM for early summer 2004 using 2002 biomass burning emissions. Net CO exports increased by 9%; the impact on other species was smaller. Because of stronger westerlies, enhanced lightning NO emissions over North America in summer 2004 than in 2002 and a possible increase in O₃ imported from stratosphere in 2004 (consistent with *Thompson et al. [2007a]*), net O₃ exports were greatly enhanced in the UT compared to 2002.

Despite reduced ANO_x emissions due to the NO_x SIP Call and cooler temperatures (Figure 6b) in 2004 relative to 2002, simulations with the UMD-CTM show greater anthropogenic exports in 2004 than in 2002 (Figure 22a). This was likely due to an efficient transport mechanism from North America: enhanced convective lofting over polluted areas (Figure 5b) and stronger westerlies (Figures 6b and 6d). Similarly, the exports of NO_x, NO_y and O₃ due to lightning NO emissions in 2004 greatly exceeded those seen in 2002 (Figure 22).

Due to lofted pollution from the BL, ANO_x exports peaked in the UT in both years. NO_y exports due to anthropogenic emissions peaked in the lower troposphere. Increased lightning activity and stronger UT westerlies over the CONUS in early summer 2004 resulted in a factor of 2 greater LNO_x exports than in 2002. In early summer 2004, anthropogenic emissions explain about 28% and 41% of the net NO_x and NO_y column exports, respectively, while lightning explains about 49%–67% and

34%–49% (the lower estimates corresponding to production of $240 \text{ NO mol flash}^{-1}$ and the upper estimates corresponding to production of $480 \text{ NO mol flash}^{-1}$). The remaining 5%–23% of the net NO_x , and 10%–25% of the net NO_y , is from other NO_x sources (biomass burning emissions and soil release) and the contribution from the north and south into NA. O_3 exports due to anthropogenic emissions were a factor of 1.6 larger than those due to lightning in 2004 ($54 \times 10^7 \text{ O}_3 \text{ mol d}^{-1}$ compared to $33 \times 10^7 \text{ O}_3 \text{ mol d}^{-1}$). However, in a sensitivity simulation with doubled LNO_x source, this ratio decreases to 1.2 (O_3 exports due to lightning increased by 33% to $44 \times 10^7 \text{ O}_3 \text{ mol d}^{-1}$). This is consistent with the earlier result where doubled LNO_x source over North America increased the lightning enhancements by ~33% in downwind regions compared to lightning enhancements from LNO_x source in the standard simulation. In 2002, anthropogenic emissions contributed twice as much to the net O_3 export as lightning.

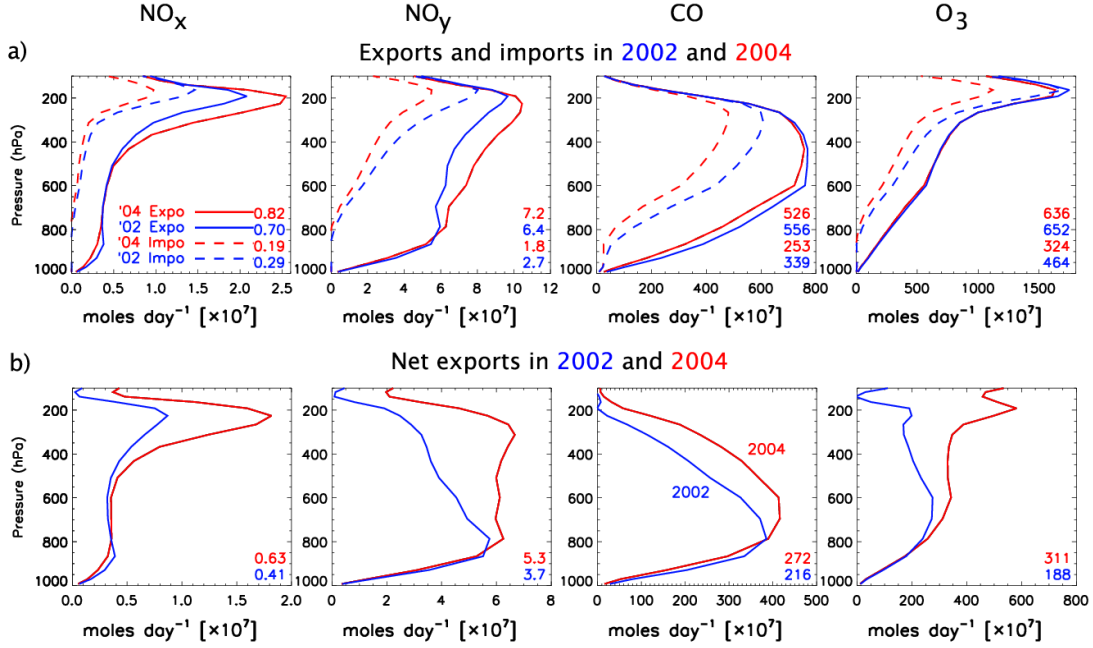


Figure 21. Early summer (1 June to 17 July) fluxes of NO_x, NO_y, CO and O₃ across the western and eastern boundaries of North America (summed between 25°N and 60°N) at 130°W (imports) and 65°W (exports) from simulation L1 for (a) 2004 exports (red solid), 2004 imports (red dashed), 2002 exports (blue solid) and 2002 imports (blue dashed) and (b) 2004 (red) and 2002 (blue) net exports. Vertically averaged fluxes (from the surface to 100 hPa) are listed in the bottom right corner of each plot. Fluxes across the northern and southern boundaries of North America are small and are not shown.

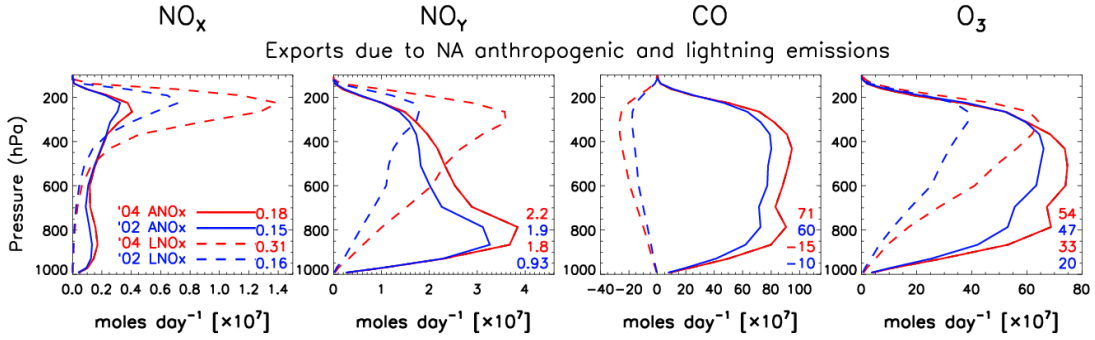


Figure 22. Same as Figure 21 except that exports due to North American anthropogenic (solid) and lightning (dashed) emissions are shown as diagnosed by sensitivity simulations with respective sources turned off (Table 1). Exports in 2004 are red and exports in 2002 are blue.

3.4 Summary

This study illustrates the importance of interannual variations in meteorology and associated lightning for the variability of long-range transport and continental outflow. We conducted several simulations of summers 2002 and 2004 with the UMD-CTM driven by meteorological fields from the GEOS-4 CERES reanalysis. Summer 2004 had reduced power plant NO_x emissions in the Ohio River Valley (resulting from the NO_x SIP Call), more lightning, relatively cool temperatures and frequent synoptic disturbances over the contiguous United States compared to summer 2002. We used 2004 as a reference year to evaluate the UMD-CTM due to the valuable measurements that were obtained over the eastern United States and western North Atlantic during the INTEX-A science mission. Summer 2004 revealed great decreases in observed surface O₃ concentrations over the northeastern United

States, especially downwind of the Ohio River Valley, the region with a high number of power plants that had implemented NO_x controls. The satellite observations from SCIAMACHY clearly detected NO₂ column decreases in this region.

We also conducted several lightning sensitivity simulations. We assumed the lightning flashes are proportional to the square of convective mass fluxes and constrained to match the observations from OTD/LIS and from the NLDN. We found an inconsistency between LIS- and NLDN-based total flash rates over the CONUS south of 35°N: more lightning was observed by the NLDN network (after adjustment by the IC/CG ratios) than by the LIS sensor. For agreement between these two data sets, the summertime IC/CG ratios over this region would have to be decreased by a factor of 2.

Like other global and regional CTMs, O₃ in the UMD-CTM is overestimated by 15–25 ppbv at the surface and by up to 12 ppbv in the upper troposphere (500–200 hPa) compared to aircraft and ozonesonde measurements. We found that the simulation with doubled lightning NO production (480 mol flash⁻¹) agrees best with observed NO_x; however, it increases the upper tropospheric high bias for O₃ by ~3 ppbv. Because of these mixed results, we complement the results from the standard simulation with the results from the simulation with doubled lightning NO production per flash. In the Ohio River Valley, the UMD-CTM showed similar reductions (19%) of tropospheric NO₂ column as observed by SCIAMACHY (22%) between August 2002 and 2004, consistent with the emission reductions due to the NO_x SIP Call. Simulations with the UMD-CTM showed reduced O₃ concentrations at

the surface between the summers 2002 and 2004; however, these reductions were 50% less than those seen in AQS observations.

Lightning over the United States greatly enhances the North American outflow of O₃. In early summer 2004, North American anthropogenic emissions produced the greatest O₃ enhancements near the surface (up to 35 ppbv over the eastern United States), whereas lightning had the greatest impact in the upper troposphere (up to 16 ppbv for the standard and 20 ppbv for doubled LNO_x source, over the Gulf Coast and the western North Atlantic). After the onset of the North American Monsoon, the impact of lightning was even greater (up to 18 ppbv for the standard and 22 ppbv for doubled LNO_x source). RF (defined as net downward radiative flux at the tropopause for clear sky conditions) of 0.15–0.30 W m⁻² due to O₃ produced from anthropogenic emissions was seen in the continental outflow across the North Atlantic, extending to Europe and northern Africa, while RF due to O₃ produced from lightning NO emissions was 0.20–0.40 W m⁻² (0.25–0.50 W m⁻² for doubled LNO_x source) over the same areas in early and late summer 2004. Lightning flash rates in early summer 2004 were 50% higher than in 2002 over the contiguous United States. RF due to lightning was nearly a factor of 2 larger in early summer 2004 than 2002 in the North American outflow region. The normalized RF per unit of added O₃ column was 0.027 W m⁻² DU⁻¹ for anthropogenic enhancements and 0.047 W m⁻² DU⁻¹ for lightning enhancements. This is because of stronger radiative forcing efficiency of an upper tropospheric perturbation.

Sensitivity simulation with reduced emissions due to the NO_x SIP Call showed that the impact of emission reductions (between 2002 and 2004) on O₃

column over the North Atlantic (30°N – 50°N) was a factor of 7 smaller than the impact of changes in lightning and meteorology in early summer. Late summer changes in lightning had much smaller impact on O_3 columns.

Large differences between the two summers in horizontal winds and convection greatly modulated the changes in O_3 concentrations. Simulations with the UMD-CTM show that despite reduced emissions due to the NO_x SIP Call and cooler temperatures in 2004 relative to 2002, more O_3 was exported from North America in 2004 due to anthropogenic emissions than in 2002 because of enhanced lofting of polluted air from the boundary layer (in early summer) followed by stronger westerly winds over the main NO_x source region in the eastern United States. O_3 exports across the eastern NA boundary due to anthropogenic emissions were factor of 1.6 larger than those due to lightning in 2004. However, the simulation with doubled lightning source reduces this ratio to only 1.2 indicating nonlinearity. Doubling the North American lightning NO source increased downwind ozone enhancements due to lightning NO emissions by one third.

4 Regional Modeling

4.1 Introduction

The findings from the previous chapter show that the O₃ generated from lightning NO_x is an important contributor to radiative forcing because of the upper tropospheric perturbation.

Traditionally, the ozone distributions required for radiative forcing calculations are determined by coarse global chemistry transport models. In this chapter, we simulate the spatial and vertical distributions of O₃ by using the regional air quality model WRF-Chem, in which chemistry is fully coupled with meteorology [Grell *et al.*, 2005] and includes an interactive treatment of aerosols [Fast *et al.*, 2006]. In general, regional air quality and chemical transport models assume climatological profiles of ozone in their radiation schemes throughout the atmospheric column. In this chapter, the model O₃ is incorporated into the radiation schemes, thus allowing heating rates from ozone to affect meteorological and chemical quantities, which we refer to as interactive ozone. We use the interactive ozone to investigate the magnitude of the radiative forcing due to lightning NO emissions in the WRF-Chem model. Our WRF-Chem simulations are driven by NASA's MERRA reanalysis [Rienecker *et al.*, 2011]. Initial and boundary conditions for chemical species are taken from NASA's global chemical transport model GMI with combined stratospheric and tropospheric chemistry [Duncan *et al.*, 2007, 2008]. To our knowledge, trace gases from GMI have not been used previously to drive regional air quality models before.

We use the lightning NO parameterization of *Hansen* [2011], which estimates total flash rates based on convective precipitation and mixed phase depth. This lightning scheme is expected to be available in the next annual release of WRF (2013) and is similar to the schemes of *Allen et al.* [2012] and *Koo et al.* [2010] in that it places lightning NO emissions at the locations of model convection. However, this lightning parameterization also accounts for the lapse rate of storms by using mixed phase depth as an additional predictor of flash frequency.

We conduct sensitivity simulations for July 2007 over the continental United States, a region with frequent summertime lightning. The simulations are performed with and without interactive O₃ and with and without lightning NO emissions in order to explore impacts of ozone perturbations on OLR. In section 4.2, we describe the experimental set-up and evaluate the flash rate parameterization. We hypothesize that incorporating O₃ into radiation schemes can improve the accuracy of radiative flux calculations. We focus on the longwave portion of the spectrum and conduct single column experiments for clear sky. In section 4.3, we explore this hypothesis with back of the envelope calculations with single column calculations for ozone perturbations in the upper troposphere. Section 4.4 includes WRF-Chem comparisons with ozonesonde and satellite measurements. We then discuss O₃ enhancements from lightning and the impact on surface ozone. We include a comparison with satellite-observed OLR, investigate the radiative effects of interactive O₃ and calculate the radiative forcing of O₃ generated from LNO_x. Lastly, we estimate the export of reactive nitrogen from the contiguous United States. The results are summarized in section 4.5.

4.2 Model Description

For the regional simulations we apply the Weather Research and Forecasting model with chemistry (WRF-Chem version 3.2.1) [Grell *et al.*, 2005]. WRF-Chem represents the first community online-coupled model in the United States and provides the capability to simulate chemistry and aerosols from cloud resolving scales to regional scales [Zhang, 2008]. The chemistry component of WRF-Chem is fully consistent with the meteorological component (WRF); both use the same transport scheme, grid (horizontal and vertical), and physics scheme. Gas-phase atmospheric chemistry in this study is based on the CBM-Z mechanism [Zaveri and Peters, 1999], which uses 67 prognostic species and 164 reactions. Rates for photolytic reactions within CBM-Z are computed by the Fast-J scheme [Wild *et al.*, 2000]. Aerosols are treated by the Model for Simulating Aerosol Interactions and Chemistry (MOSAIC) [Zaveri *et al.*, 2008] using 4 sectional bins. Table 3 summarizes the WRF-Chem configuration options used in this study.

Table 4 identifies the modeling scenarios used to isolate the impact of lightning NO emissions on O₃ concentrations, as well as the impact of interactive O₃ on radiative fluxes. WRF-Chem is run at 36 km with 40 vertical levels extending up to 50 hPa with increased resolution in the boundary layer (12 levels in the lowermost 1 km) and near the tropopause with a time step of 3 minutes. We composite a total of ten 90-hour forecasts that begin at 00 UTC 1 July and end at 18 UTC 31 July 2007. The model integrations are re-initialized at 00 UTC every third day, allowing an 18-hour period for model spin-up (i.e., the first 18 hours of model output is excluded from analysis).

Table 3. Selected WRF-Chem Configuration Options

Atmospheric Process	WRF-Chem Option	Reference
Longwave radiation	RRTM	<i>Mlawer et al.</i> [1997]
Shortwave radiation	Goddard	<i>Chou and Suarez</i> [1999]
Surface layer	Monin-Obukhov	<i>Foken</i> [2006]
Land surface model	Noah	<i>Chen and Dudhia</i> [2001]
Boundary layer	Yonsei University (YSU)	<i>Hong et al.</i> [2006]
Cumulus	Grell 3D ensemble	<i>Grell and Devenyi</i> [2002]
Cloud microphysics	Lin	<i>Chen and Sun</i> [2002]
Photolysis	Fast-J	<i>Wild et al.</i> [2002]
Meteorological IC/BC ^a	MERRA	<i>Rienecker et al.</i> [2011]
Chemical IC/BC ^a	GMI-CTM	<i>Duncan et al.</i> [2008]
Gas-phase chemistry	CBM-Z	<i>Zaveri and Peters</i> [1999]
Aerosol chemistry	MOSAIC 4 bins	<i>Zaveri et al.</i> [2008]

^a Initial and boundary conditions (IC/BC)

Table 4. The WRF-Chem Sensitivity Simulations

Simulation Name	Lightning NO _x ^a	O ₃ Profile in Radiation Scheme
noL	none	Climatology
LNO _x (standard)	NLDN-based (500)	Climatology
noL-IO	none	Interactive O ₃
LNO _x -IO	NLDN-based (500)	Interactive O ₃
Low LNO _x	NLDN-based (250)	Climatology

^a Observed flash rates used to adjust the model flash rates over the CONUS; lightning NO moles produced per flash are in parentheses.

4.2.1 Meteorological and Chemical Initial and Boundary Conditions

Meteorological initial and boundary conditions at 6 hour intervals were interpolated from NASA's reanalysis MERRA (Modern Era Retrospective-Analysis for Research and Applications, <https://gmao.gsfc.nasa.gov/merra/>) provided at $2/3^{\circ} \times 1/2^{\circ}$ resolution and 42 pressure levels by Global Modeling and Assimilation Office (GMAO) [Rienecker *et al.*, 2011]. MERRA was generated with the NASA Global Earth Observing System (GEOS) atmospheric model and data assimilation system (DAS), version 5.2.0 [Rienecker *et al.*, 2008]. Several studies have analyzed various aspects of the scientific quality of MERRA reanalysis, for example the work of Bosilovich *et al.* [2011], who evaluated MERRA from an energy and water budget perspective. To run WRF with the Noah land surface scheme requires at least four levels of soil moisture and soil temperature. The soil moisture and temperature came from NCEP's North American Regional Reanalysis (NARR), which is available at a

32-km resolution. The NARR data set is available at http://nomads.ncdc.noaa.gov/#narr_datasets and documented by *Mesinger et al.* [2006].

Chemical initial and boundary conditions for WRF-CHEM are interpolated from NASA's Global Modeling Initiative (GMI) CTM [*Duncan et al.*, 2007, 2008] driven by the same meteorology (MERRA reanalysis) as WRF-Chem. We ran the GMI-CTM at a horizontal resolution of $2^\circ \times 2.5^\circ$ with 72 vertical levels with a lid at 0.01 hPa. The GMI-CTM chemical mechanism includes 124 species, 322 chemical reactions and 81 photolysis reactions to simulate tropospheric and stratospheric chemistry. The tropospheric mechanism includes a detailed description of O₃-NO_x-hydrocarbon chemistry [*Bey et al.*, 2001] and has been updated with recent experimental data [*Tyndall et al.*, 2001; *Dunlea and Ravishankara*, 2004]. The chemical mass balance equations are integrated using the SMVGEAR II algorithm [*Jacobson*, 1995]. Photolysis rates are computed using the Fast-JX radiative transfer algorithm [*Bian and Prather*, 2002].

While we do not attempt to do a comprehensive evaluation of the impact of using different initial and boundary conditions, since NARR is routinely used by the WRF community, we perform a sensitivity simulation driven by the NARR reanalysis and compare the WRF results between this and the MERRA driven simulation at two snapshot times from July 7 and July 8, 2007 (Figure 23). Compared to the NCEP Stage IV precipitation analysis derived from combination of radar and rain gauges (<http://www.emc.ncep.noaa.gov/mmb/ylin/pcpanl/stage4/>), the convective system from July 7 at 18 UTC over the southeastern United States is better represented in the simulation driven by the MERRA reanalysis. Although the location of the system is

missed by 200 km, the peak precipitation totals are well captured. Comparing the 6 hour precipitation totals between the Stage IV estimates and amounts from simulations driven by WRF, we see that the areas where the amounts exceed 20 mm are approximately the same size ($27,000 \text{ km}^2$). The mean 6 hour accumulation from the simulation driven by MERRA is 35 mm over the regions where totals exceed 20 mm, while the accumulation from the Stage IV estimate is 29 mm. The simulation driven by NARR fails to capture amounts $> 20 \text{ mm}$. In addition, the convective system in the southwestern part of the WRF domain (northern Mexico) at 06 UTC on July 8 is captured only by the simulation driven by MERRA. Although this comparison includes only two snapshots, it shows the sensitivity of model convection to initial and boundary conditions.

The initial and boundary conditions for WRF-Chem simulations with no lightning NO are obtained from the GMI-CTM simulation with global LNO_x source turned off, and initial and boundary conditions for WRF-Chem simulations with lightning NO emissions are obtained from the GMI-CTM simulation with LNO_x source turned on. The lightning parameterization in GMI-CTM is based on convective mass fluxes; model-calculated flash rates are constrained to match the geographical distribution of flash rates observed by OTD/LIS [Allen *et al.*, 2010]. In the vertical, the lightning NO emissions are distributed on the basis of cloud resolved modeling studies of Ott *et al.* [2010].

The following species are obtained from the GMI-CTM: O₃, carbon monoxide (CO), nitrogen oxides (NO_x), NO₃, N₂O₅, HNO₃, HNO₄, peroxyacetyl nitrate (PAN), H₂O₂, formaldehyde, ethane, acetone, methanol, methylglyoxal and isoprene. Ethene,

toluene and cresol are not included in the GMI-CTM chemical mechanism. Initial and boundary conditions for these three species, as well as for SO₂ and aerosol species, are obtained from global chemical transport model MOZART-4 (Model for Ozone and Related Chemical Tracers) [Emmons *et al.*, 2010; Pfister *et al.*, 2011], driven by meteorological fields from the NASA GMAO GEOS-5 model (fields available at <http://www.acd.ucar.edu/wrf-chem/mozart.shtml>).

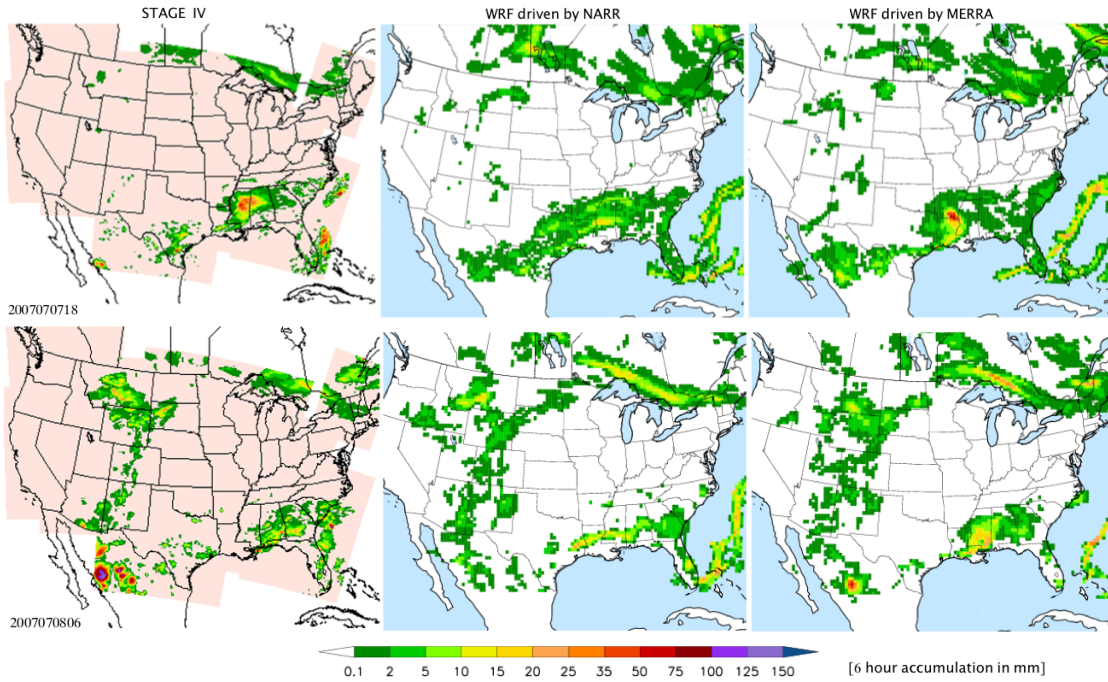


Figure 23. 6 hour precipitation totals ending (top) July 7, 2007 18 UTC and (bottom) July 8, 2007 06 UTC as (left) observed by radar and rain gauges (NCEP Stage IV), (middle) predicted by WRF driven by NARR and (right) predicted by WRF driven by MERRA. Radars operated by National Weather Service have an observation range of 460 km, so Stage IV data does not include rain over oceans beyond this range, although the WRF simulations do.

4.2.2 Emissions

The emission data sets were preprocessed by the Sparse Matrix Operator Kernel Emissions modeling system (SMOKE) version 2.7 [<http://www.smoke-model.org>; *SMOKE*, 2010]. In the first step we run WRF with no chemistry to prepare meteorological fields (e.g., surface temperature, radiation) required for emissions processing. These fields are then processed by SMOKE to create chemically speciated, and spatially allocated hourly emissions for WRF-Chem. We use the EPA 2005 National Emissions Inventory (NEI version 4.2) as input to SMOKE. A detailed description of the emissions inventory can be found at <http://www.epa.gov/ttnchie1/emch/index.html>. The NEI inventory includes onroad mobile source emissions estimated by the Motor Vehicle Emission Simulator [MOVES, 2010]. The SMOKE platform also includes the Biogenic Emissions Inventory System (BEIS version 3.14) used to generate meteorologically adjusted emissions from vegetation and soils.

4.2.3 Lightning

It is well known that lightning produces NO_x as a result of the high temperatures in discharge channels. Recent midlatitude and subtropical case studies involving cloud resolved modeling constrained by observed flash rates and anvil NO_x measurements from field experiments such as STERAO [*DeCaria et al.*, 2005], EULINOX [*Fehr et al.*, 2004; *Ott et al.*, 2007], and CRYSTAL-FACE [*Ott et al.*, 2010], have found that IC flashes dissipate nearly as much energy as CG flashes and that both CG and IC midlatitude flashes produce on average about 500 NO moles

flash^{-1} [e.g., *Ott et al.*, 2010]. In our WRF-Chem simulations, we assume all flashes produce 500 moles of NO. Our parameterization only injects lightning NO over grid boxes in which parameterized deep convection is active.

To specify flash frequency in each grid box, we use the look up table by *Hansen* [2012] who analyzed a relationship between convective precipitation and mixed phase depth (both from NARR reanalysis) and total lightning flash rate derived from NLDN observations. This new lightning parameterization technique is currently being implemented and is expected to be available to the community in the next annual WRF-Chem release. *Hansen* [2012] constructed two look up tables from summer 2004 NLDN observed flash rates and NARR fields over the continental United States, one for 36 km resolution (employed in this study) and the other for 12 km. The look up table contains NARR mixed phase depth (every 100m), 3 hour total precipitation (for every 1 mm), and the coinciding 3 hour flash rate. In WRF-Chem, the mixed phase depth is determined by the difference between the height of the freezing level and -40°C isotherm. One of the advantages of using the look up table parameterization is that the total flash rate can be diagnosed in each time step (i.e., no preprocessing is required). In our case, mean model flash rates using the look up table were overestimated with respect to monthly NLDN estimate (CG flashes adjusted by IC/CG ratio to obtain the sum of IC and CG flashes) over the CONUS and therefore required scaling by a factor of 0.77, which is applied to every grid box. This is likely because the Grell 3-D convective parameterization overestimated precipitation compared to the NARR data set.

In addition to the approach of *Allen et al.* [2012], who used only convective precipitation to estimate flash frequency, the *Hansen* [2012] approach also uses mixed phase depth, which is indicative of lapse rate. A shallow depth corresponds to a larger lapse rate, implying stronger updrafts and therefore more lightning than when the mixed phase depth is greater (i.e., a smaller lapse rate).

The mean NLDN (IC + CG) flash rate over the CONUS in July 2007 was 8.4 flash s^{-1} . Figure 24 shows that the geographical distributions of observed flash rates, model convective precipitation and model flash rates for both schemes are similar over the CONUS. The mean July 2007 observed flash rate peaked over Florida (Figure 24a), which corresponds to convective precipitation predicted by WRF for the same time period (Figure 24b). The distribution of model flash rate in Figure 24c derived from the look up table using convective precipitation and mixed phase depth [*Hansen*, 2012] is similar to the distribution of model flash rate in Figure 24d derived from just convective precipitation [*Allen et al.*, 2012]. The scheme with look up table [*Hansen*, 2012] captured the peak over Florida better because of its nonlinear response to increases in convective precipitation. The difference between model and observed flash rate over southern Texas is due to biases in model precipitation.

Next, we analyze model flash rate histograms. This analysis is needed because O_3 production is a nonlinear function of NO_x concentration with smaller flash rates producing O_3 more efficiently. Figure 25 compares the histograms of model flash rates for both approaches with the NLDN based estimate. The histograms are constructed from all grid boxes with nonzero flash rate. Both *Hansen* [2012] and *Allen et al.* [2012] agree with the histogram of observed flash rates with a slight

underestimation of grid boxes with very small flash rates. There are 16% of grid boxes with flash rate $< 0.5 \text{ flash}^{-1}$ for NLDN-based total, whereas *Hansen* [2012] and *Allen et al.* [2012] show 13% and 11%, respectively. We expect that this small underestimation has a minor impact on O₃ production.

Besides the similarities seen in mean horizontal flash rate distributions and histograms, both approaches yield similar day-to-day variations (Figure 26). Using the look up table gives slightly higher correlation between model and NLDN-based flash rates compared to the approach of *Allen et al.* [2012] (correlation of 0.51 versus 0.48). Model flash rates derived from the look up table by *Hansen* [2012] are highly correlated with model convective precipitation ($r = 0.93$), so there is little room to improve day-to-day variations if mixed phase depth is used in addition to convective precipitation.

We use the summer 2006–2007 segment altitude distributions (SADs) based on VHF sources from the North Alabama lightning mapping array (LMA) to distribute lightning NO in the vertical [*Koshak et al.*, 2010]. Total SADs (i.e., the sum of IC and CG flashes) are calculated by the Lightning Nitrogen Oxides Model (LNOM) [*Koshak and Peterson*, 2011], which uses the vertical distribution of flash channel segments that are constructed from the VHF source data. To obtain the NO_x profile, we force the lower negative charge layer (lower relative peak of SAD associated with CG flashes), or the so-called “N-region” altitude of the thundercloud, to be at the height of the -15°C isotherm (Z_{-15}). This is consistent with assumptions in the work of *Koshak and Peterson* [2011] and *Ott et al.* [2010].

Hansen et al. [2010] analyzed thunderstorms from two summers over the Kennedy Space Center, Florida and found that the vertical distribution of lightning sources varies between storms and depends on the storm top height. In order to better account for these variations, we apply two different profiles, as shown in Figure 27a, one for low elevations (the eastern United States and adjacent waters) and the other for high elevations (the northern latitudes and mountains), with a threshold of $Z_{-15} = 6.7$ km (Figure 27b). The histogram in Figure 27c shows how Z_{-15} is distributed for all cases with deep convection during the modeling period with the threshold of 6.7 km clearly separating the two scenarios. The difference between the two is that for low elevations and latitudes, the lower peak of SAD (associated with CG flashes) is at ~ 7.3 km above ground level (AGL), while it is at ~ 5.5 km AGL for high elevations and latitudes. The higher peak of SAD (associated with IC flashes) is at ~ 11 km AGL for low elevations and latitudes and at ~ 9 km AGL for high elevations and latitudes. This addresses the fact that storm top heights are higher AGL over the southern United States, where elevations are lower and convection is deeper. Therefore, the LNO_x is deposited 2 km higher compared to the rest of the domain.

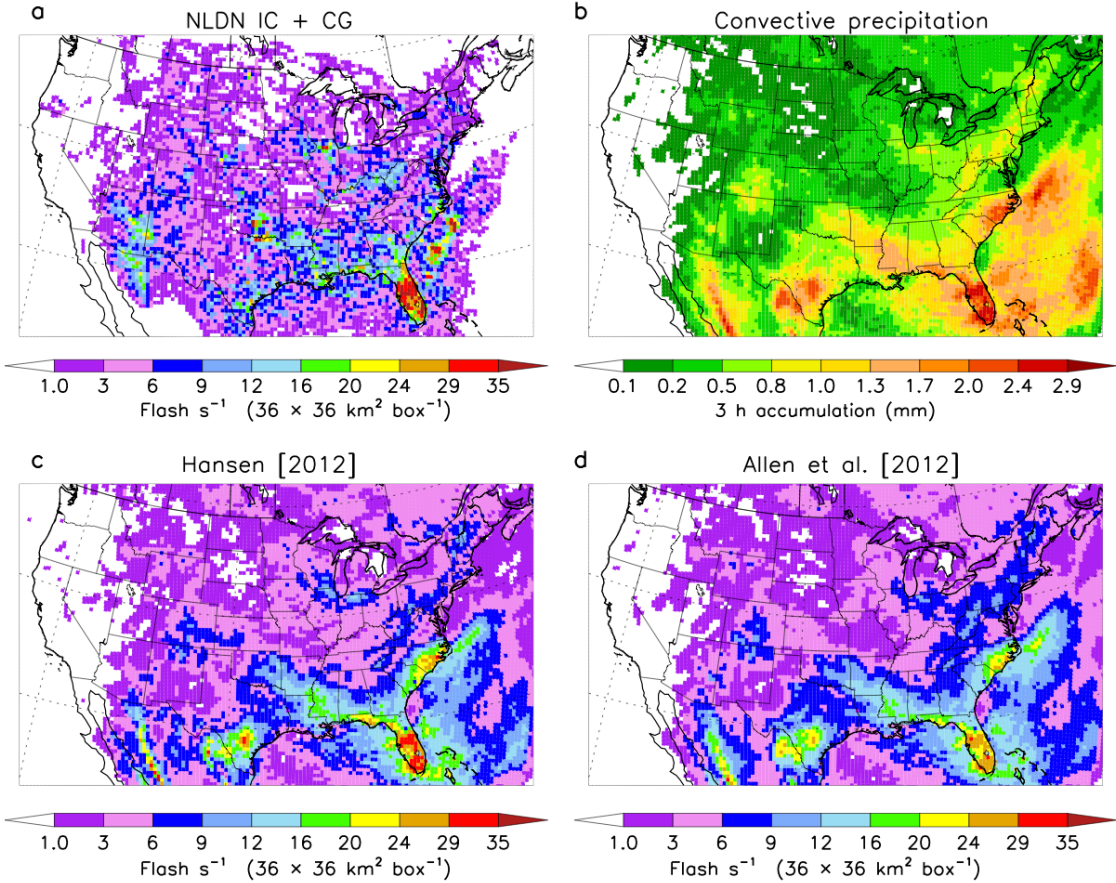


Figure 24. **(a)** Mean flash rate distribution during July 2007 as estimated by multiplying the NLDN CG flash rate by $Z+1$, where Z is the smoothed climatological IC/CG ratio. **(b)** Convective precipitation (3 hour totals) as predicted by WRF. Model flash rate **(c)** based on look up table [Hansen, 2012] and **(d)** based on convective precipitation [Allen *et al.*, 2012]. Model flash rates in Figures 24c and 24d are scaled so the monthly sum over the CONUS matches the NLDN-based sum in Figure 24b. All flash rates are in units of flash s^{-1} per 36-km grid box. Detection efficiency for NLDN observed flashes falls off rapidly with distance from coast. Therefore NLDN flash rates do not represent actual flash rates for locations with distance $> 300 \text{ km}$ from the coast. Model flash rates outside of the CONUS are decreased by a factor $f = \exp(-d / 1000)$, where d is the distance from the coast in km.

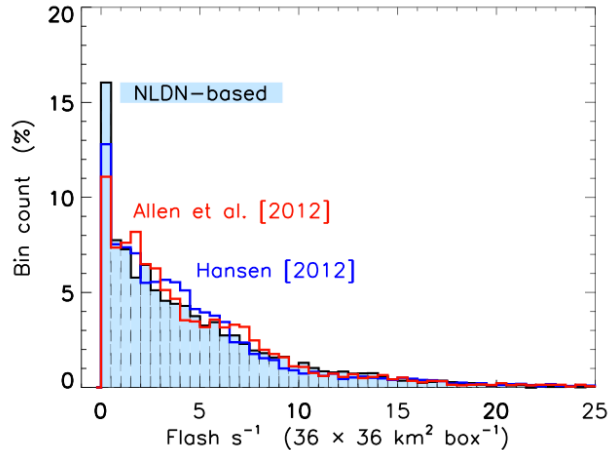


Figure 25. Same as Figures 24a, 24c and 24d except the histogram depicting the distributions of 1 h flash rates over the CONUS is shown. The histogram of NLDN-based total flash rates is indicated by the blue shaded area, histogram of model flash rates based on *Hansen* [2012] is the blue line and histogram of model flash rates based on *Allen et al.* [2012] is the red line.

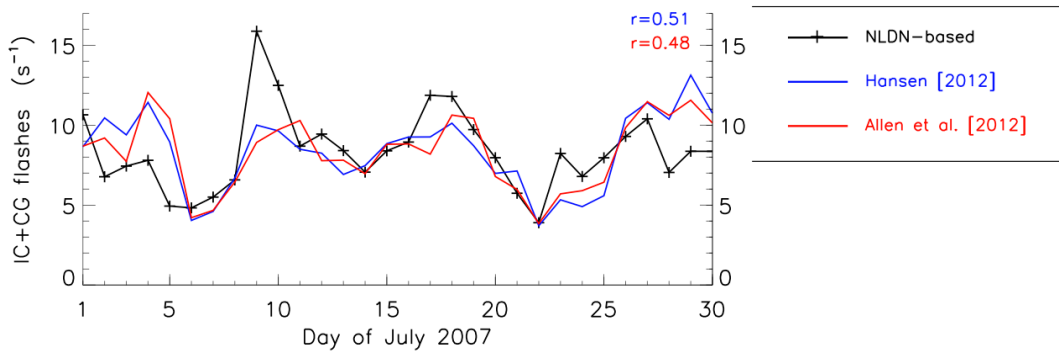


Figure 26. Time series of daily flash rates summed over the continental United States (land only) during July 2007. NLDN-based estimate obtained by multiplying NLDN CG flash rate by $Z + 1$, where Z is the smoothed climatological IC/CG ratio, depicted by black line. Model flash rates based on convective precipitation [*Allen et al.*, 2012] (red) and model flash rate based on convective precipitation and mixed phase depth [*Hansen*, 2012] (blue) are both scaled to match total monthly NLDN (IC + CG) flash rate. Correlation between time series of observed and model flash rates (r) is top right.

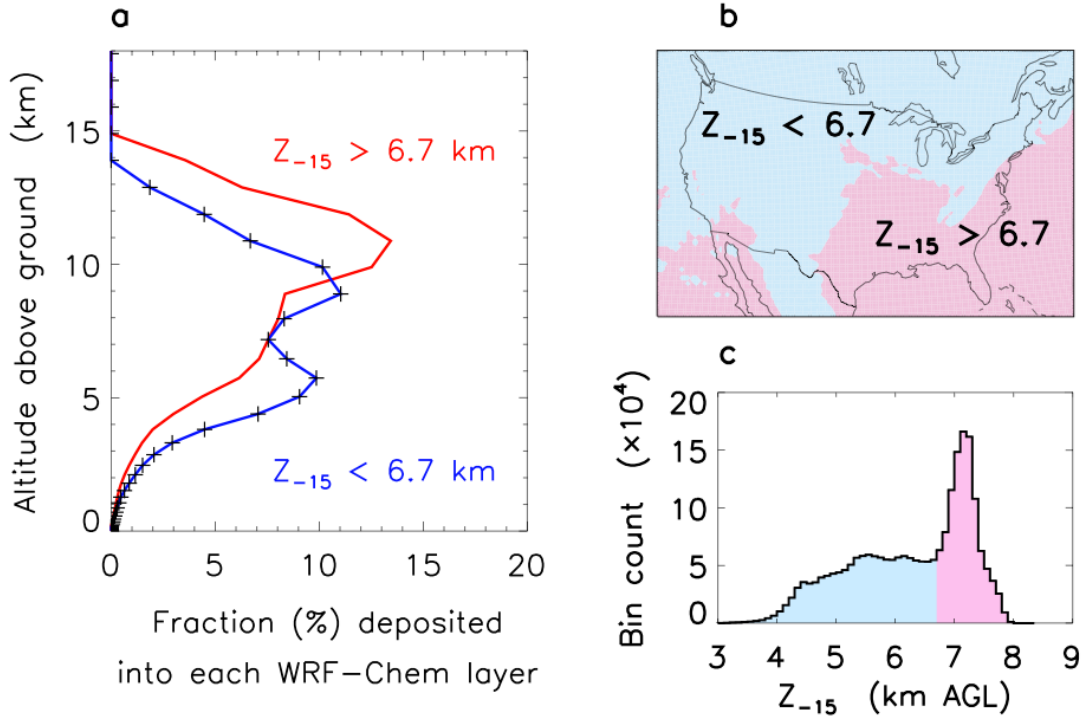


Figure 27. (a) Vertical distribution of lightning NO production (mass-like units) assumed in WRF-Chem simulations for locations with the height of -15°C isotherm (Z_{-15}) greater (red) and less (blue) than 6.7 km. These profiles were derived from the vertical distribution of VHF sources in the vicinity of the North Alabama lightning mapping array during the summers 2006 and 2007. Plus signs indicate the centers of the WRF-Chem layers. (b) Spatial mask for grid points with mean $Z_{-15} > 6.7 \text{ km}$ (red) and with $Z_{-15} < 6.7 \text{ km}$ (blue). (c) The histogram depicting the distribution of WRF-calculated Z_{-15} per 0.1 km bin over the modeling domain during July 2007 constructed from the grid boxes with deep convection. Corresponding parts of the distribution are color-coded.

4.2.4 Radiation Schemes in WRF

For air quality applications, WRF-Chem is most commonly configured with the Rapid Radiative Transfer Model (RRTM) longwave and Goddard shortwave radiation schemes [*Chapman et al.*, 2009]. For this configuration, the aerosol properties are fully coupled with WRF meteorology and chemistry when run with the MOZAIC aerosol model [*Fast et al.*, 2006; *Gustafson et al.*, 2007], which allows simulation of the localized cooling by sulfate aerosol and heating by black carbon. In the current version of WRF-Chem, O₃ calculated by WRF-Chem photochemistry in the troposphere is not used in radiation schemes (neither longwave nor shortwave). All radiation schemes in WRF use climatological profiles of O₃ throughout the atmospheric column. For instance, the RRTM longwave scheme assumes one climatological O₃ profile (the average of standard midlatitude summer and winter) each time the radiative transfer is calculated. The Goddard shortwave and longwave schemes use five climatological O₃ profiles (standard midlatitude and subarctic summer and winter profiles and tropical profile) to calculate the radiative heating rates. These standard ozone profiles come from the Air Force Geophysics Laboratory (AFGL) reference atmospheres [*Anderson et al.*, 1986]. The tropical profile is used for latitudes 0°–30°; the midlatitude profiles are used for latitudes 30°–60°, and the subarctic profiles are used for latitudes 60°–90°.

There are large differences in the UT/LS between these standard ozone profiles. For instance, the ozone concentration at 12 km is 80 ppbv, 220 ppbv and 520 ppbv for the tropical, midlatitude summer and midlatitude winter profiles, respectively. Figure 28 compares these standard profiles with mean simulated ozone

profiles averaged over the eastern two thirds of United States (110°W – 70°W , 25°N – 45°N) for July 2007. The model tropopause lies in between the standard tropical and midlatitude tropopause, and there is much less predicted O_3 in the UT/LS region compared to the standard midlatitude summer climatology used in the RRTM longwave radiation scheme.

In the next section, we explore the longwave radiative effects of these differences and ozone perturbations in the UT/LS. At this time the shortwave radiative effects will not be discussed further.

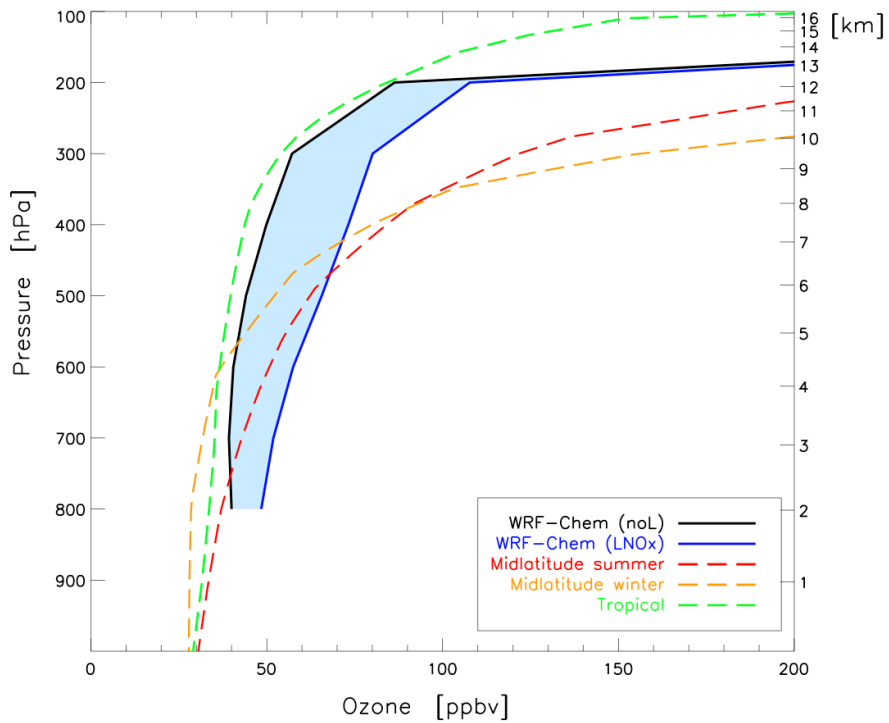


Figure 28. Mean vertical distribution of ozone during July 2007 averaged over the eastern two-thirds of the United States (110°W – 70°W , 25°N – 45°N) as calculated by WRF-Chem (solid blue) LNO_x simulation (Table 4). Mean profile from the sensitivity simulation with no LNO_x source averaged over the same area and time period is shown in black, and lightning enhancement is indicated by blue shaded area. Standard midlatitude summer (red), standard midlatitude winter (brown) and standard tropical (green) vertical profiles assumed in radiation schemes are shown as dashed lines. Please see text in section 4.2.4 for more details regarding these profiles.

4.3 Single Column Experiments With the Offline RRTM Longwave Model

The rapid radiative transfer model (RRTM) is an accurate and computationally fast model [*Mlawer et al.*, 1997] which uses the correlated-k method [*Fu and Liou*, 1992] to calculate fluxes and heating rates. The RRTM agrees well with calculations from the line-by-line radiative transfer model [*Clough and Iacono*, 1995] which has been and continues to be extensively validated against high quality radiometric measurements [*Clough et al.*, 2005; *Shephard et al.*, 2009].

The RRTM calculates fluxes and heating rates using water vapor and temperature profiles and cloud information obtained online from WRF. Ozone mixing ratios are interpolated from the average midlatitude reference profile (i.e., average of midlatitude summer and winter) onto model levels. Therefore in the standard WRF-Chem implementation, the ozone vertical distribution used in the RRTM does not vary in space or time.

We explore the impact of O₃ perturbations in the UT/LS region on radiative fluxes. We apply the stand-alone version of RRTM3.3 (available at <http://rtweb.aer.com>) to compute the OLR and heating rates for standard midlatitude summer and tropical atmospheric profiles in a single column for clear sky conditions. First, we compute the OLR difference between the standard midlatitude summer and tropical atmosphere. Outgoing longwave radiation for the standard midlatitude summer atmosphere is 281.4 W m⁻² and for the standard tropical atmosphere is 287.2 W m⁻². The difference of 5.8 W m⁻² is because of differences in the vertical

distribution of ozone, temperature and water vapor used in the radiative transfer calculation. Second, we compute the OLR difference between the mean O_3 profile predicted by WRF-Chem (the July 2007 average over the eastern two thirds of the United States, see Figure 28) and the average midlatitude O_3 profile (assumed climatology in RRTM), both with standard midlatitude summer temperature and water vapor profiles in order to separate the effects due to O_3 perturbations. The difference between the two is 3.6 W m^{-2} . Next, we explore the difference due to lightning enhancement as diagnosed from the WRF-Chem standard LNO_x simulation and simulation noL (Table 4) (the July 2007 average over the eastern two thirds of the United States, see Figure 28). The OLR due to enhanced O_3 from LNO_x is reduced by 0.36 W m^{-2} . These flux values represent a back of envelope calculation of the impact of changes in O_3 in the UT/LS region on OLR for a case with the standard midlatitude summer water vapor and temperature and clear sky conditions.

The impact of different O_3 distributions on heating rates is shown in Figure 29a. This figure depicts vertical profiles of the heating rates from the standard midlatitude summer and tropical profiles. Because of less ozone in the upper troposphere in the standard tropical ozone profile, ozone heating rates are smaller than for the standard midlatitude ozone profile. The upper troposphere at $\sim 200 \text{ hPa}$ (12 km) is the most sensitive to ozone perturbations, with a small impact below 5 km (Figure 29b). Ozone increments added in the UT/LS region have the largest impact on heating rates and fluxes because the temperature contrast between the radiation absorbed and emitted by an O_3 increment is the largest near the tropopause [Lacis *et al.*, 1990].

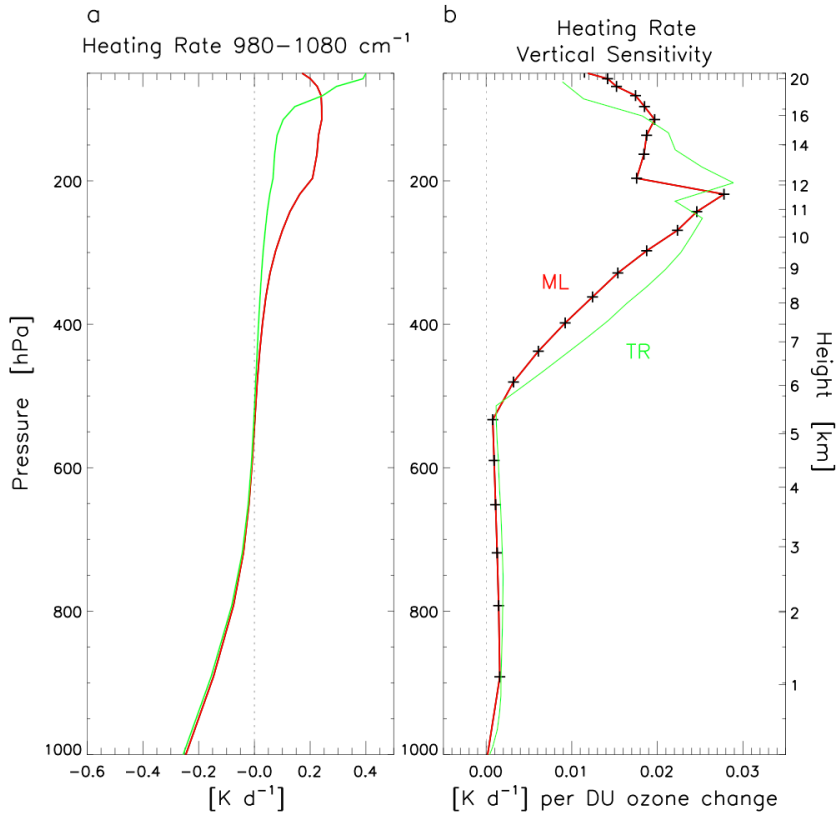


Figure 29. (a) Longwave radiative heating rates for the $9.6 \mu\text{m}$ ozone band ($980\text{--}1080 \text{ cm}^{-1}$), and (b) radiative heating rate sensitivity to changes in vertical ozone distribution for the standard midlatitude summer (green) and tropical (brown) ozone profiles from Figure 28. For vertical sensitivity in Figure 29b, 40-ppbv ozone increments were added to each atmospheric layer (layer centers are indicated by plus signs in the right panel), and the peak increase in heating rate (from the $9.6 \mu\text{m}$ ozone band) is then normalized to 1 Dobson unit ozone increment.

4.4 WRF-Chem Results

We start by analyzing the general features of the standard WRF-Chem simulation (Table 4). Figure 30 shows the NO_x and O_3 concentrations at the surface and upper troposphere averaged from hourly model output between 2 July and 30 July. NO_x concentrations are the largest at the surface because of large anthropogenic NO_x emissions, including areas such as the Ohio River Valley, Chicago, and Detroit (Figure 30c). In the upper troposphere, the largest concentrations are over Florida where lightning occurs most frequently (Figure 30a). The mean O_3 concentrations at the surface over the eastern two thirds of the United States is 41 ppbv with a standard deviation (σ) of 11 ppbv. The upper tropospheric values are a factor of 2 larger, but the variability for O_3 remains unchanged over the same region ($\sigma = 11$ ppbv, 68% of the O_3 distribution at 300 hPa is between 69 ppbv and 91 ppbv). The upper troposphere over the eastern United States has larger O_3 concentrations than over the western half, with a local maximum over Virginia and North Carolina. Figure 28 shows that the mean O_3 enhancement produced from LNO_x over this area, as diagnosed from the sensitivity simulation noL (Table 4) at 300 hPa, is 22 ppbv, which indicates that lightning contributes more than one quarter to the UT O_3 concentrations.

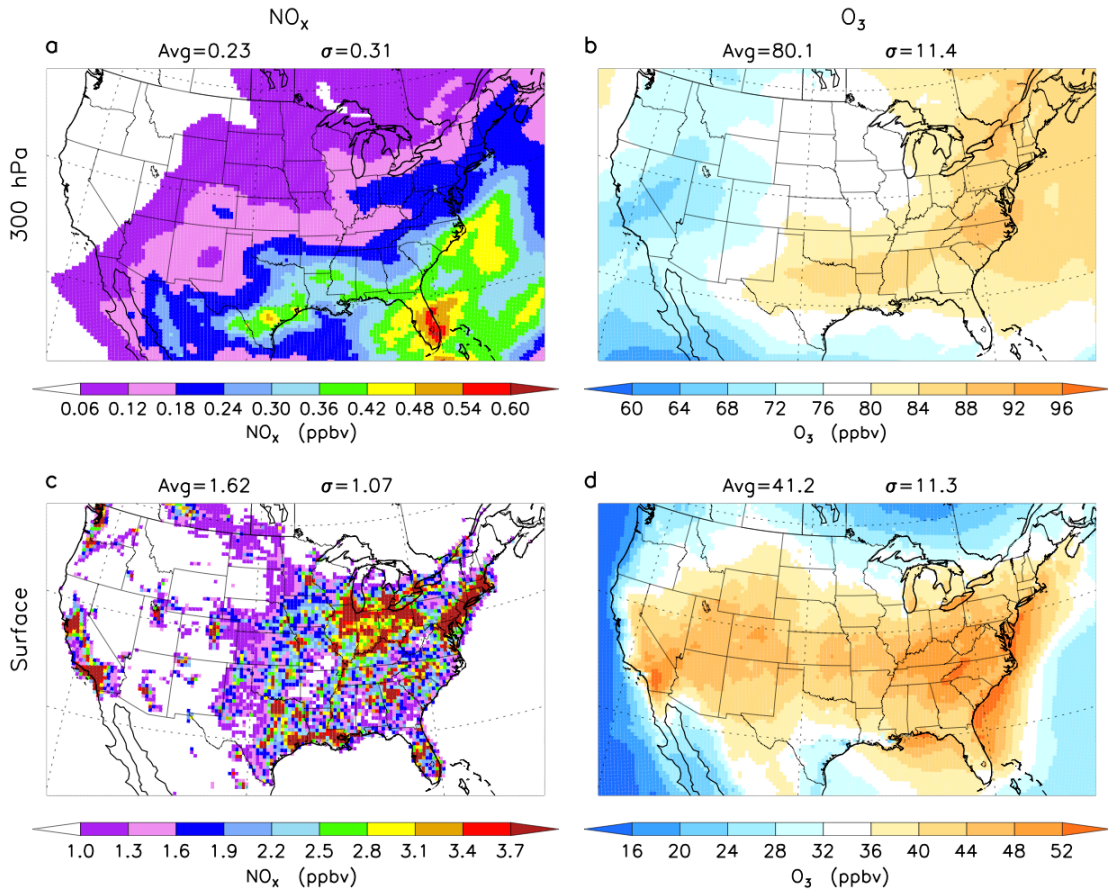


Figure 30. Mean (**a, c**) NO_x and (**b, d**) O_3 concentrations over the CONUS from standard simulation LNO_x (Table 4) averaged from 2 July to 30 July, 2007 at (top) 300 hPa and (bottom) surface. The average and the mean standard deviation (σ) of hourly time series over the eastern two thirds of the United States are indicated in the title of each plot.

4.4.1 Comparison With Surface NO_x and NO_y Measurements at Pinnacle State Park Research Site

In this section, we evaluate the WRF-Chem simulation using hourly NO_y and NO_x measurements at a remote site in Pinnacle State Park, New York, located at

42.1°N and 77.2°N with elevation of 504 m [Schwab *et al.*, 2009]. The WRF-Chem captures the diurnal and day-to-day variations in both NO_y and NO_x (Figure 31). Mean observed NO_y during July 2007 was 2.72 ppbv. Simulated NO_y is overestimated with respect to observations by 0.25 ppbv (9%), mainly because of nighttime overprediction (by 0.51 ppbv, 19%). Daytime NO_y overestimation is 0.12 ppbv (4%). Mean observed NO_x was 1.46 ppbv. Mean NO_x bias during day and night is small (-0.02 ppbv).

In general, both simulated NO_y and NO_x agree well with measured data at this rural location in the northeastern United States.

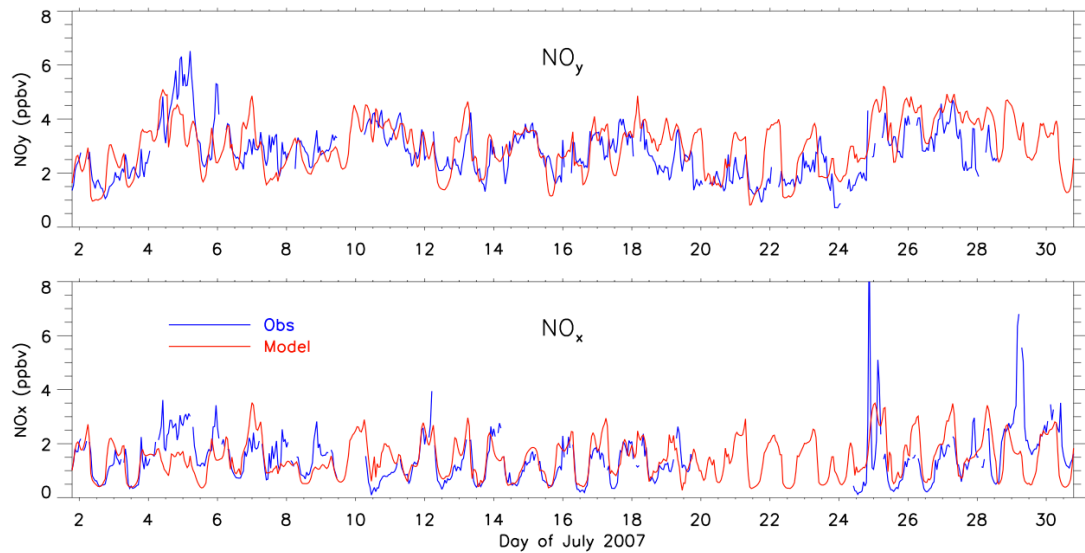


Figure 31. Time series of 1 h NO_y and NO_x as observed at Pinnacle State Park, New York, research site (blue line) and simulated with the WRF-Chem (red line) for July 2007. Measurements of NO_x between 19 and 24 July are missing. Missing data between 9 and 10 July are due to failure of air conditioning in the instrument unit.

4.4.2 Comparison With OMI NO₂ Columns

The Ozone Monitoring Instrument (OMI) aboard the NASA Aura satellite measures direct sunlight and backscattered light from the Earth's atmosphere in the ultraviolet-visible range. It retrieves NO₂ with a resolution of $13 \times 24 \text{ km}^2$ in nadir. We use the level 2 Dutch OMI NO₂ product (DOMINO) version 2 [Boersma *et al.*, 2007, 2011]. Similarly, as with SCIAMACHY data (section 3.3.2.3), pixels with cloud fractions exceeding 0.3 are excluded from analysis.

In order to compare satellite retrieved NO₂ columns to their WRF-Chem counterparts, we sample hourly WRF-Chem NO₂ profiles at the locations and times of OMI retrievals. Next, we interpolate these WRF-Chem profiles onto the TM4 vertical grid and then we apply the OMI averaging kernels for each OMI pixel. To obtain the tropospheric NO₂ columns, we integrate tropospheric layers up to the TM4 tropopause. Finally, we aggregate both OMI and WRF-Chem columns onto a $0.5^\circ \times 0.5^\circ$ grid. The mean value in each grid box is obtained by weighting the high quality retrievals using the algorithm of *Celarier and Retscher* [2009] by applying weights to both OMI and WRF-Chem columns. This algorithm gives more weighting to near-nadir pixels than to far-off-nadir pixels and to clear sky pixels than to partly cloudy pixels. This method of comparing OMI retrievals and model output is the same as in the work of *Allen et al.* [2012], who compared OMI with the CMAQ air quality model.

Figure 32 compares the tropospheric NO₂ columns from DOMINO with WRF-Chem simulated columns. The mean columns on the native 36 km grid are shown in Figure 32b. They were calculated using hourly model output at the time

closest to overpass time assuming the tropopause is at 150 hPa. Figure 32c shows the mean WRF-Chem columns after interpolation onto the TM4 vertical grid, applying averaging kernel and aggregating onto a $0.5^\circ \times 0.5^\circ$ grid. Figure 32d is the same except with the LNO_x source decreased by a factor of 2. This is consistent with previous analyses done with the UMD-CTM model in which we conducted two simulations, one with high LNO_x production and the other with the LNO_x source decreased by a factor of 2. The flashes over the southeastern United States may be more tropical in nature and therefore producing less NO moles than their midlatitude counterparts. Tropical thunderstorms have smaller vertical wind shear resulting in shorter flash lengths which may cause smaller NO production per flash [Huntrieser *et al.*, 2009].

Allen et al. [2012] showed that applying an averaging kernel improves the agreement with the satellite-retrieved DOMINO product. They analyzed CMAQ runs at 12 km and made a comparison on a $0.25^\circ \times 0.25^\circ$ grid for summer 2006 and found that their columns were underestimated. However, the application of an averaging kernel brings the model columns closer to satellite-retrieved columns. In our case, the application of the averaging kernel reduces columns over the urban areas (e.g., Chicago, Detroit, Atlanta, New York) too much, but the domain average remains unchanged. WRF-Chem columns over the eastern two thirds of the United States (110°W – 70°W , 25°N – 45°N) using the standard simulation are overestimated compared to the DOMINO data by ~16%. Model columns using the simulation with LNO_x decreased by a factor of 2 agree better, which indicates the sensitivity to lightning NO₂ amounts. The reasons for the high bias are likely due to

overestimations in any or all of the following: (1) NO production flash⁻¹, (2) NLDN-based total flash rate (Figure 8 shows a factor of 2 larger estimate compared to OTD/LIS), and (3) ANO_x emissions. The maxima due to lightning over Florida that are detected by the NLDN network are not present in the DOMINO product (Figure 24a), which may partially be due to the coarse resolution of the TM4 chemical transport model ($3^\circ \times 2^\circ$). These results indicate the challenges of comparing model columns with satellite-retrieved columns. The discrepancies may also arise from the differences in the vertical distribution of NO₂ in WRF-Chem and the a priori profiles used in the NO₂ retrieval.

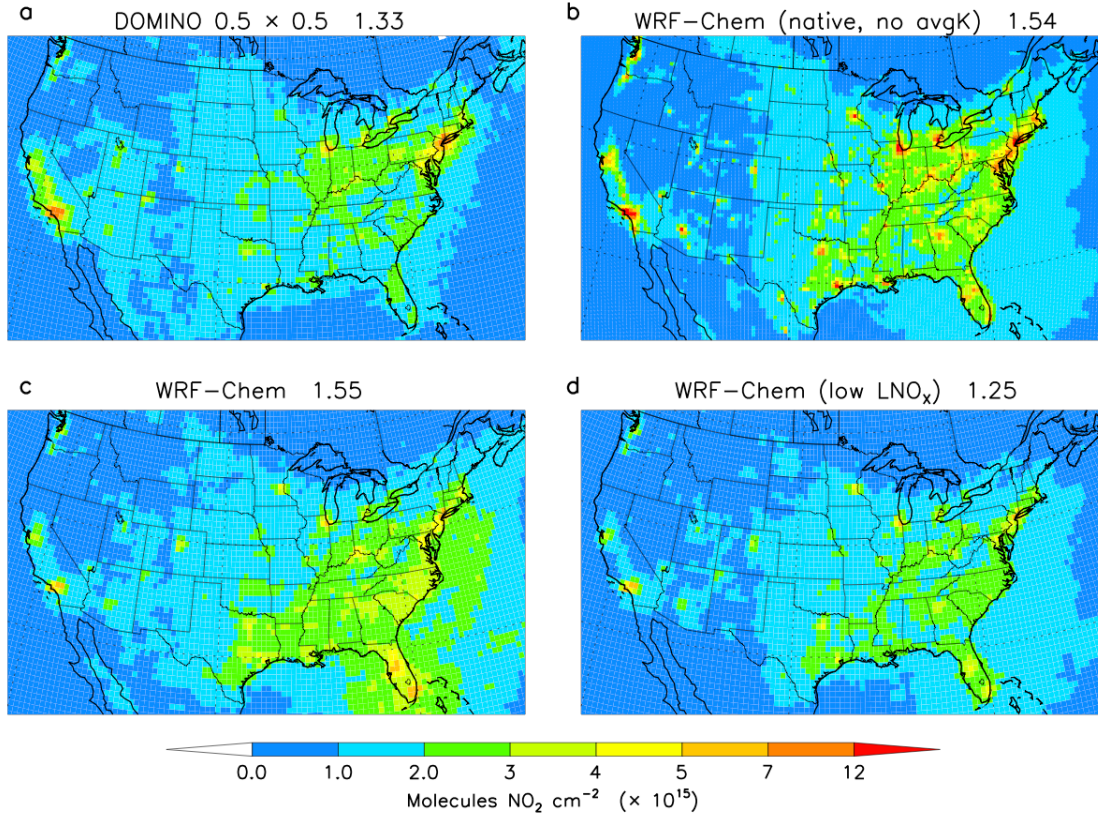


Figure 32. Mean tropospheric NO_2 column from 2 July to 30 July, 2007. (a) The mean version 2.0 DOMINO column on $0.5^\circ \times 0.5^\circ$ grid, (b) the mean WRF-Chem tropospheric column from the standard simulation LNO_x on the native 36-km grid. The mean WRF-Chem tropospheric column from the (c) standard LNO_x and (d) low LNO_x simulation on the $0.5^\circ \times 0.5^\circ$ grid after processing by the OMI averaging kernel.

4.4.3 Comparison With Ozonesonde Soundings

In this section, we evaluate the WRF-Chem simulation using twenty ozonesonde measurements made during July 2007 over three North American sites: Beltsville, Maryland located at 76°W and 39°N , Huntsville, Alabama located at 87°W

and 35°N and Wallops Island, Virginia located at 75°W and 38°. At Beltsville, as part of the NASA WAVES campaign (Water Vapor Validation Experiments) hosted at the Howard University Research Campus, two soundings were launched during the night at 06 UTC, and nine were launched in the early afternoon at 18 UTC to capture overpasses of the Aqua and Aura satellites. At Huntsville, soundings were launched weekly on Saturdays at 18 UTC. We use the data averaged over 100 meter intervals downloaded from http://nsstc.uah.edu/atmchem/about_ozonesonde.html. At Wallops Island, soundings were also launched at 18 UTC, and the data are provided by NASA-WFF (Wallops Island Flight Facility) from World Ozone and Ultraviolet Radiation Data Centre (WOUDC) from <http://www.woudc.org>.

Figure 33 compares mean modeled and observed ozone profiles at these three North American sites during July 2007. Lightning NO production ($500 \text{ mol flash}^{-1}$) increases model-calculated upper tropospheric (500–200 hPa) ozone by 21–23 ppbv over the Beltsville, Huntsville and Wallops Island sites. As expected, WRF-Chem simulated profiles with lightning NO emissions match the shape of the ozonesonde profiles better in the middle and upper troposphere and capture the concentrations in the UT/LS region better than the simulation without LNO_x emissions.

Next, we compare the biases of WRF-Chem LNO_x simulations with the UMD-CTM simulation (L2) in section 3.3.2.2 (Figure 11). Compared to UMD-CTM, WRF-Chem shows (1) better agreement throughout the vertical column at Huntsville, a site with frequent thunderstorms, (2) better agreement at the surface for all three sites, and (3) similar overestimation by as much as 14 ppbv at Wallops Island. *Allen et al.* [2012] noted overestimation of 23 ppbv in the upper troposphere

using the CMAQ air quality model during summer 2006 at Huntsville and Wallops Island.

4.4.3.1 Uncertainty Analysis

The uncertainty of the simulated vertical distribution of O₃ depends on the uncertainty of ozone precursor emissions and on the uncertainty of ozone and precursor transport and chemistry. The most important precursor of ozone is NO_x. Because the lifetime of NO_x is much shorter than the lifetime of ozone, both emissions (ANO_x and LNO_x) and vertical transport (boundary layer venting, warm conveyor belts and deep convection) impact the vertical distribution of O₃ and its precursors [e.g., *Pickering et al.*, 1992; *Cooper et al.*, 2006]. The largest source of ANO_x emissions uncertainty is representation of mobile sources (about one third of total ANO_x emissions); uncertainty can be 30% or more. In addition to this uncertainty, our ANO_x emissions may be biased high by 5%–15% in the eastern United States, since we use 2005 NEI emissions. Figure 34 shows an estimate of the decrease in ANO_x emissions from the United States between summer 2005 and 2007 as derived from OMI observations of NO₂ columns and using the GEOS-Chem model [*Lamsal et al.*, 2011]. The comparison with measurements at a rural location in Pinnacle State Park, New York (section 4.4.1), suggests that errors in boundary layer concentrations are not a large contributor to biases in the free troposphere.

To estimate the uncertainty of boundary layer venting and deep convection, we conducted a sensitivity simulation with the new Kain Fritsch (KFEta) convective parameterization [*Kain*, 2004]. Compared to the standard simulation with Grell 3-D

convective parameterization, the impact on upper tropospheric (500–200 hPa) ozone at three ozonesonde sites was less than ± 1.3 ppbv (<2%). Of course, differences between model simulations are usually smaller than differences between models and observations.

Emissions of NO_x directly into the UT are primarily due to lightning and aircraft traffic. Lightning NO emissions are a function of flash rate, vertical partitioning of NO and NO production per flash. The main contributor to uncertainty due to LNO_x emissions is the NO production per flash. For example, when the LNO_x source is changed from 240 to 480 NO mol flash⁻¹, the UT ozone increases by 5 ppbv (6%) [Allen *et al.*, 2010]. Production per flash for individual storms may be outside of this range adding additional uncertainty. In addition, our flash rates may be overestimated (Figure 34 shows a factor of 2 discrepancy between NLDN-based and LIS-based total flash rates south of 35°N during 2002–2005). Including aircraft emissions increases O₃ concentrations by 0.7 ppbv (1%) [Allen *et al.*, 2012].

Imprecisions in photolysis and chemical reaction rates also contribute to overall uncertainty. For example, uncertainty in the photolysis rate of NO₂ (an important reaction for ozone production) used in the photochemical mechanism is 20% [JPL, 2006]. Noteworthy is the study by *Thompson and Stewart* [1991] who using a Monte Carlo technique, showed that the combined effects of rate constant uncertainties in a photochemical model are 16% for O₃. Another unaccounted source of uncertainty may be the rate at which NO₂ oxidizes to HNO₃. Allen *et al.* [2012], in a chemistry sensitivity simulation based on the recommendations of *Henderson et al.* [2011], showed an impact of 2 ppbv (3%) on O₃ concentrations due to known

uncertainties in the NO_2 conversion rate to HNO_3 . In addition, the lifetime of alkyl nitrates is overestimated in the model [Saylor and Stein, 2012]. While this likely leads to an overestimation of concentrations of alkyl nitrates in the boundary layer, we expect that in the upper troposphere, the contribution to ozone biases is relatively small compared to the effect in the boundary layer. Further research is needed to improve the understanding of NO_x lifetime (including the understanding of alkyl and isoprene nitrate chemistry) and its impacts on ozone concentrations.

In order to estimate uncertainty due to possible HO_2 biases [Wennberg *et al.*, 1998], we sample simulated HO_2 concentrations at hours and locations of DC-8 measurements during the INTEX-A campaign. We use only the measurements from nine flights that were over the CONUS. Model HO_2 is approximately the same or slightly less than the observed HO_2 in the upper troposphere (model shows <5% low bias for four flights and <20% low bias for five flights), so it does not appear that HO_2 biases contribute to O_3 biases. However, definitive results are not possible because this comparison is between July 2004 and July 2007.

In addition to the uncertainties of NO_x , transport errors also contribute to ozone errors (the ozone loss in the UT/LS is small). Although stratosphere to troposphere exchange contributes to UT concentrations, it is most important in the springtime. For summertime conditions, the dominant transport-related factor is the specification of lateral boundary conditions [Tang *et al.*, 2008].

Despite these uncertainties mentioned above, simulated O_3 profiles compare well with vertical soundings and well capture UT/LS concentrations (ozone

tropopause), which is important for investigating the radiative effects of interactive ozone and ozone produced from lightning.

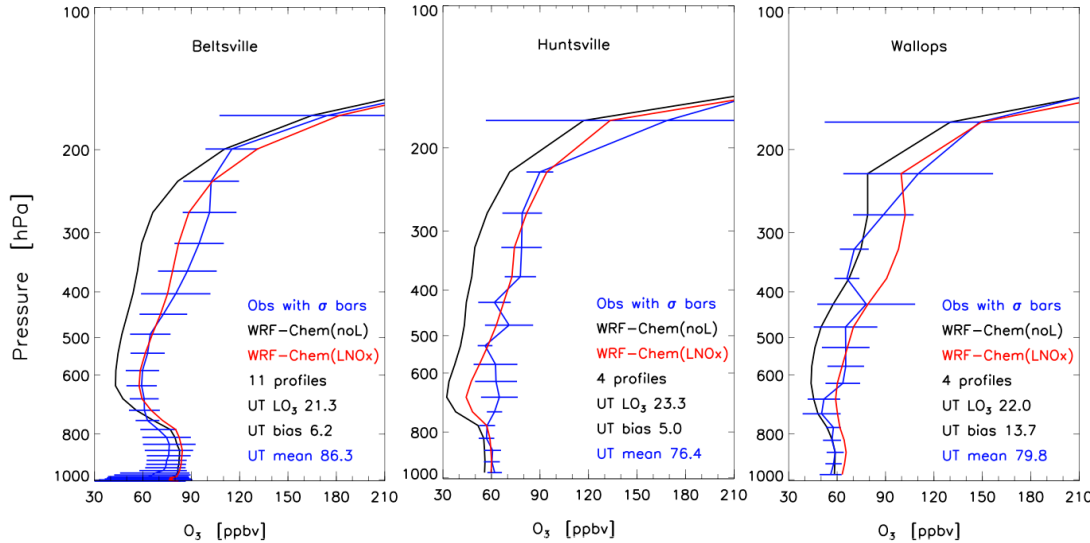


Figure 33. Mean profiles as observed from ozonesondes (blue) and simulated with WRF-Chem at (left) Beltsville, Maryland (left), Huntsville, Alabama (middle) and Wallops Island, Virginia (right) during July 2007. WRF-Chem simulation noL (LNO_x) is shown in black (red). Horizontal bars around the mean ozonesonde-measured values indicate standard deviations (σ) in each model layer for Beltsville and in each 50-hPa bin for Huntsville and Wallops. Numbers in the lower right corner show the number of soundings available, the lightning NO contribution to upper tropospheric (500–200 hPa) ozone (LO_3), the upper tropospheric absolute values of the bias (model minus measurement), and the mean measured upper tropospheric ozone.

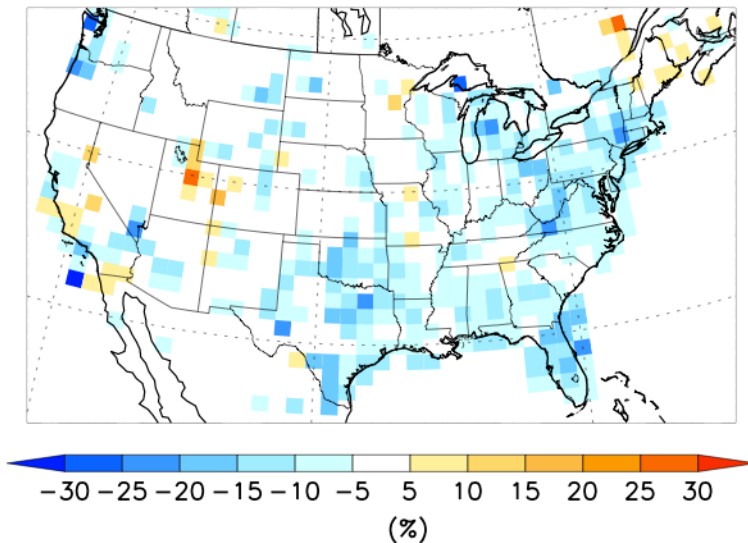


Figure 34. Decrease in anthropogenic NO_x emissions from the United States between summer 2005 and 2007 as derived from OMI observations of NO₂ columns and using the GEOS-Chem model [Lamsal *et al.*, 2011].

4.4.4 Ozone Enhancements From Lightning and Impact on Surface Ozone

We analyze O₃ enhancements generated from global lightning NO sources for July 2007, focusing on the upper troposphere of the continental United States. Although not strictly true, because of the nonlinear response of O₃ to NO_x emissions, the lightning enhancement is diagnosed as the difference between simulations with and without the LNO_x source. We complement results from WRF-Chem simulations by including the results from GMI-CTM, which provides two sets of boundary conditions for trace gases, one with global source of LNO_x and one without. It should be noted that here we shut off global source, whereas in chapter 3 using the UMD-CTM, LNO_x sources are turned off only from the North American continent.

Figure 35 shows mean ozone enhancements due to LNO_x in the upper troposphere (at 300 hPa) as diagnosed by the global GMI-CTM and regional WRF-Chem models (both with 500 NO mol flash⁻¹). Although most thunderstorms were over the southeastern United States and very few over the northwest, a significant portion of ozone generated from LNO_x in the upper troposphere enters the WRF-Chem domain from GMI-CTM through western boundary. Similarly, the results from the global UMD-CTM (Figure 15) simulations showed that O₃ enhancements from lightning NO emissions from North America influence O₃ concentrations considerably throughout the tropospheric column in remote locations downwind (North Atlantic, North Africa, southern Europe). Over the continental United States both GMI-CTM and WRF-Chem have consistent O₃ concentrations with maximum (30 ppbv) over Florida.

During July 2007, lightning NO₂ represented 25% of the simulated tropospheric NO₂ column over the eastern United States (Figure 32). The mean contribution of LNO_x to surface layer ozone over the same area was 4.7 ppbv (Figure 36). The mean increase in 8 h O₃ due to LNO_x reaches high values in some locations in the western United States because of sunny conditions and deep boundary layer in these regions (Colorado, Nevada show 8–9 ppbv enhancements in 8 h O₃).

A number of studies have analyzed the impact of lightning NO at the surface. *Kaynak et al.* [2008] and *Allen et al.* [2012] analyzed the summers of 2004 and 2006 and found that lightning NO increased 8 h O₃ over the CONUS by less than 2–2.5 ppbv on 70% of days. In this study, we find that the 70% percentile reaches the

value of 5.6 ppbv over the CONUS. The median over the CONUS is 4.2 ppbv for all days and 3.8 ppbv for poor air quality days (with 8 h O₃ > 60 ppbv).

It is unclear why our results show larger 8 h O₃ values compared to other investigators. This may be because of the differences between the representation of boundary layer mixing in CMAQ (other investigators) and WRF-Chem (this study).

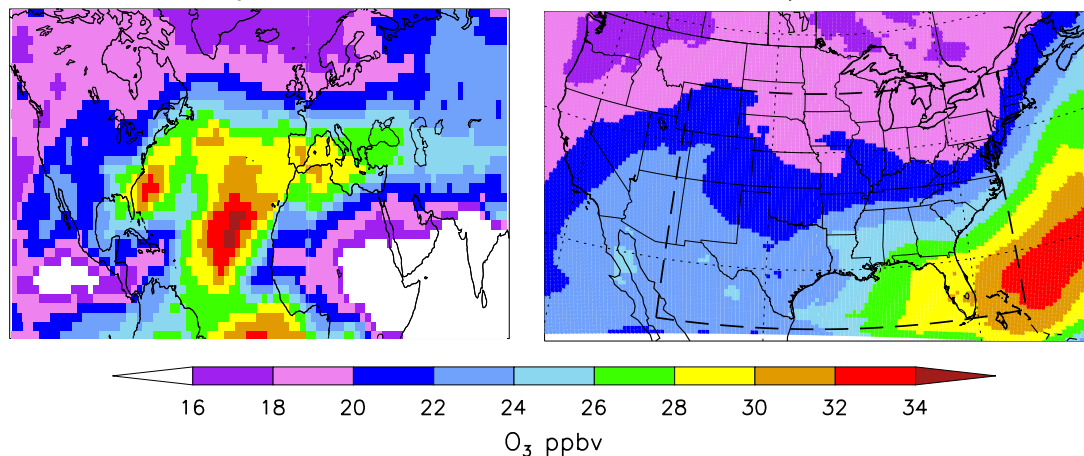


Figure 35. Mean ozone enhancements at 300 hPa for July 2007 from LNO_x source as diagnosed by (left) global GMI-CTM over the North America and downwind and as diagnosed by (right) WRF-Chem over the United States and western North Atlantic. GMI-CTM provided initial and boundary conditions of longer-lived trace gases for WRF-Chem simulations.

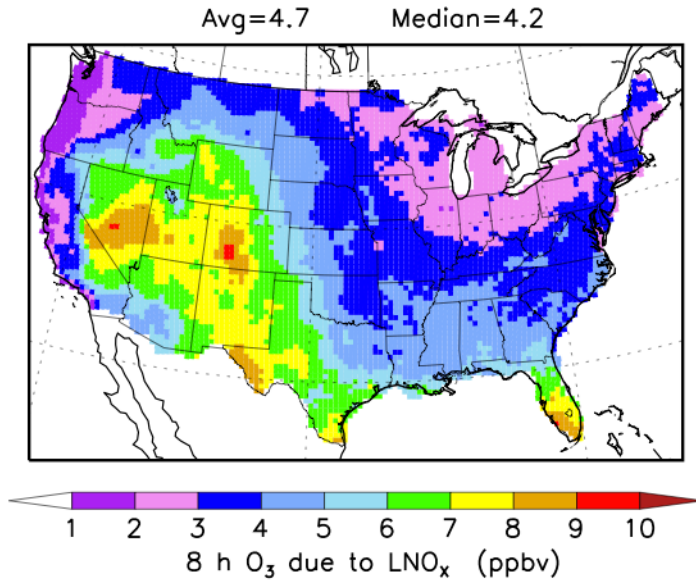


Figure 36. Increase in 8 h O_3 due to LNO_x averaged over July 2007 at surface as diagnosed from the difference between standard LNO_x simulation and sensitivity simulation with LNO_x source turned off.

4.4.5 Impact on OLR and Radiative Effects

In this section, we first compare model OLR with NOAA-18 satellite observations. We investigate the impact of using model O_3 in the radiation scheme (i.e., the impact of interactive O_3) on OLR. These results are then compared to OLR reduction due to O_3 generated from LNO_x (i.e., the radiative forcing of lightning enhanced O_3).

Estimates of outgoing longwave radiation from National Oceanic and Atmospheric Administration (NOAA) polar-orbiting satellites are often used to locate deep convection and estimate the earth's radiation budget. The NOAA-18 satellite crosses the equator at 0155 and 1355 LST. We use the daily OLR data available at http://www.esrl.noaa.gov/psd/data/gridded/data.interp_OLR.html. This data set is the

daily average computed from the twice-daily fields gridded at $2.5^\circ \times 2.5^\circ$ resolution. For details on how the OLR data set is constructed (i.e., data screening and filling gaps with interpolations in time and space) see Note by *Liebmann and Smith* [1996].

Figure 37 compares OLR data from the NOAA-18 satellite with model output sampled at satellite overpass times. The mean predicted OLR from the standard WRF-Chem simulation agrees with NOAA-18 measurements with relatively small biases (Figure 37c). For the standard LNO_x simulation over the eastern two thirds of the United States, the mean OLR difference with respect to satellite observations in regions with a low bias is -5.4% , and the mean difference in regions with a high bias is $+2.6\%$. The overall bias is -2.8% or -7.1 W m^{-2} . We compare our results to *Choi et al.* [2009], who analyzed summer 2005 using the regional chemical transport model REAM. In contrast to our results, *Choi et al.* overestimated OLR with respect to satellite observations over most of the CONUS with mean high biases of $4.7\%-5.7\%$.

If model O₃ is incorporated in the radiation scheme (interactive O₃ simulation), we see that low bias over the most of the CONUS (65% of grid boxes) decreases and high bias seen over the north central United States increases (Figure 37d). This is because of less model O₃ in the UT than the assumed O₃ climatology (see Figure 28). The root mean square error decreases from 14.6 W m^{-2} to 13.3 W m^{-2} over the CONUS; however, there is no significant improvement regionally (i.e., the root mean square error of values adjusted for the mean bias between mean observed and simulated OLR is the same for both simulations with and without

interactive ozone). Mean OLR increase due to interactive ozone is 3.1 W m^{-2} (Figure 38). The impact of LNO_x on OLR biases is smaller and not shown.

We complement the OLR results by analyzing the cloud top pressure data from the Moderate Resolution Imaging Spectroradiometer (MODIS) also onboard the Aqua satellite. We are interested in all types of high clouds (cirrus, cirrostratus and deep convective clouds) as they are most effective in altering the top-of-atmosphere longwave radiative fluxes [Chen *et al.*, 2000]. We use the level 2 cloud data collection 5 with a spatial footprint of $\sim 5 \text{ km}$ [Menzel *et al.*, 2008]. We composite the observed and simulated columns onto a $0.3905^\circ \text{ longitude} \times 0.3237^\circ \text{ latitude}$ grid, which corresponds to $36 \times 36 \text{ km}^2$ at latitude 34°N . The ISCCP (International Satellite Cloud Climatology Project) classifies high clouds as those whose cloud top pressure is less than 440 hPa. The WRF simulation indicates that there were, on average, 17.4 days out of 29 with high cloud occurrence, whereas MODIS observations indicate 16.3 high cloud days (Figure 39). The spatial distribution of high cloud frequency corresponds closely to the spatial distribution of OLR (Figure 37).

We extend our analysis by comparing the OLR changes due to interactive O₃ for all sky and clear sky conditions (Figure 40). For clear sky conditions, the impact on OLR is larger (4.2 W m^{-2} for clear versus 3.1 W m^{-2} for all sky conditions). The value of 4.2 W m^{-2} is close to the single column calculation (3.6 W m^{-2}) done for standard midlatitude summer and clear sky conditions in section 4.3.

The magnitude of this impact is nearly as large as the expected value of radiative forcing from a doubling of CO₂ (i.e., $+3.7 \text{ W m}^{-2}$ with clouds, stratospheric

adjustment and solar absorption included) [IPCC, 2007]. This suggests that inclusion of interactive ozone in the model radiation could be important for the regional climate simulations (with long simulation times). Climate simulations indicate the 3.7 W m^{-2} forcing can result in a 3–5 K increase in global surface temperature.

Next, we investigate the impact of O_3 perturbations due to LNO_x on radiative forcing. The mean lightning enhancement in the upper troposphere (500–200 hPa) is 22 ppbv as diagnosed from the simulation with 500 NO mol flash $^{-1}$ (Figure 28). The single column calculations (section 4.3) suggested that the OLR reduction due to this 22-ppbv enhancement is 0.36 W m^{-2} . Figure 41 shows the mean geographic distribution of radiative forcing due to ozone generated from LNO_x . Mean OLR reduction due to lightning over the eastern two thirds of the United States is 0.25 W m^{-2} for all sky and 0.37 W m^{-2} for clear sky conditions. The clear sky value is close to the value of 0.36 W m^{-2} determined from the single column calculations (section 4.3). The radiative forcing due to lightning for clear sky conditions found here is in the middle of the range of $0.20\text{--}0.50 \text{ W m}^{-2}$ for summer 2004 reported by *Martini et al.* [2011], who used UMD-CTM offline calculations (see Figure 19). In contrast to offline calculations, we see larger spatial variability and also some values of opposite sign due to changes in vertical distributions of temperature and water vapor, which are a result of the ozone-radiative feedback.

Figure 42a shows that the interactive ozone has a small cooling effect of -0.15°C on monthly mean UT temperatures. This cooling is because of less simulated UT ozone than in the standard climatological ozone profile. Figure 42b shows that ozone generated from LNO_x has an even smaller positive effect on monthly mean UT

temperature (0.01°C) with a mean standard deviation of 0.14°C (i.e., 68% of the distribution is within -0.13°C and $+0.15^{\circ}\text{C}$).

To summarize, the single column calculations for clear sky conditions with assumed standard midlatitude summer temperature and water vapor profiles showed that the impact of interactive O₃ was a factor of 10 larger than the impact of LNO_x on OLR. Applying the fully interactive WRF-Chem model for the entire month of July, including the whole range of meteorological conditions, the impact of interactive O₃ on OLR is a factor of 12 larger than that of LNO_x. We have shown that the inclusion of interactive ozone in radiative transfer improves the predicted OLR. The impact of interactive ozone on meteorology (upper tropospheric temperature) is small when averaged over a month's series of 4-day simulations.

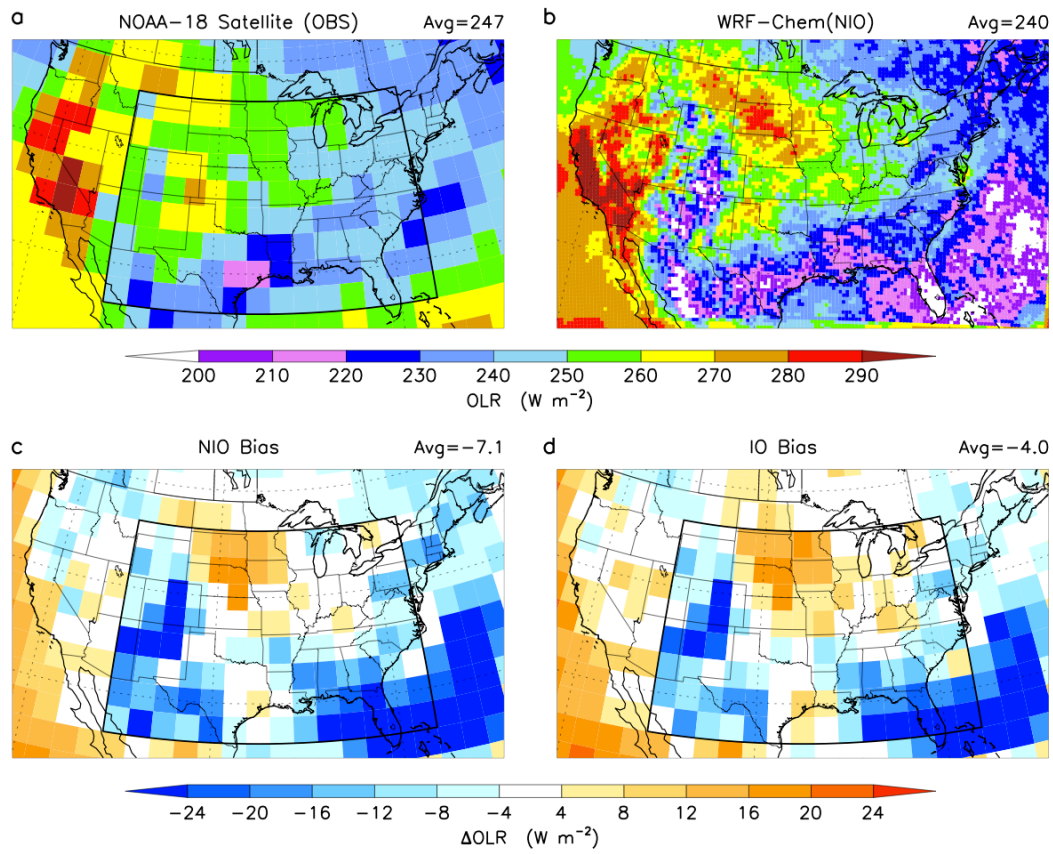


Figure 37. (a) Mean OLR over the United States from 2 July to 30 July, 2007 observed by the NOAA-18 satellite and (b) WRF-Chem standard simulation with noninteractive ozone (Table 4). (c) Difference between the WRF-Chem standard simulation with noninteractive ozone (NIO) and NOAA-18 OLR mapped at $2.5^\circ \times 2.5^\circ$ resolution. (d) Difference between the WRF-Chem standard simulation with interactive ozone (IO) and NOAA-18 OLR mapped at $2.5^\circ \times 2.5^\circ$ resolution. The value in the title of each plot is the average from the eastern two thirds of the United States indicated by the black box in Figure 37a.

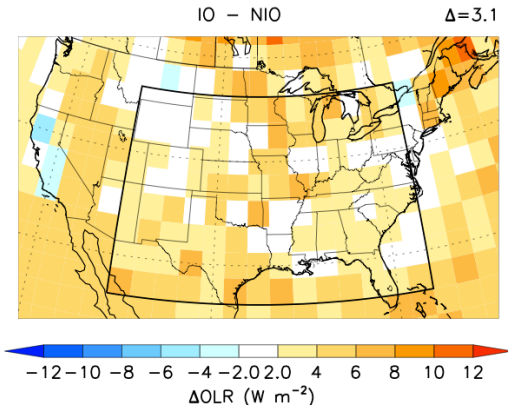


Figure 38. Same as Figure 37 except the impact of interactive O₃ on the OLR (the difference between simulation with and without interactive ozone) is shown.

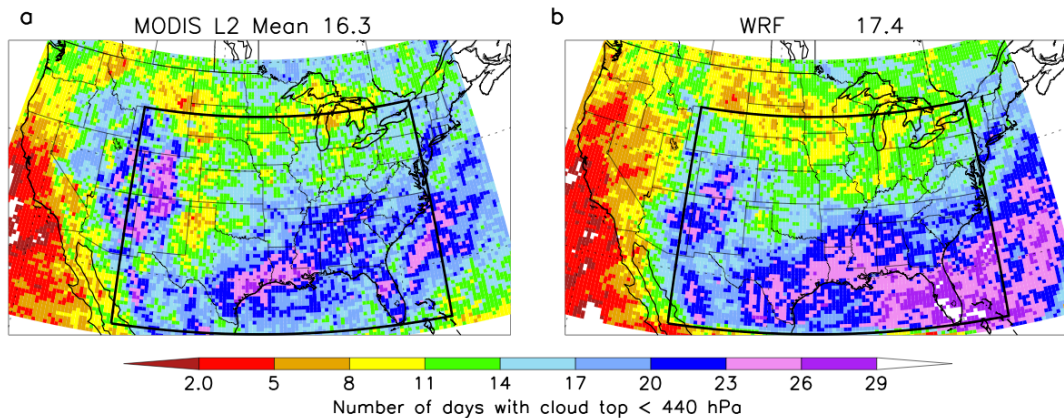


Figure 39. Comparison between (a) MODIS-retrieved and (b) WRF-calculated mean high-cloud frequency (the number of days with cloud top pressure < 440 hPa during the period 2 July to 30 July, 2007) constructed from all Aqua daytime overpasses over the CONUS. WRF is sampled at each MODIS pixel. Observed tops are composited onto a 0.3905° longitude $\times 0.3237^\circ$ latitude grid, which is close to the native resolution of WRF ($36 \times 36 \text{ km}^2$). Each grid box in Figure 39a includes on average 19 level 2 MODIS pixels. The value in the title of each plot is the mean over the eastern two thirds of the CONUS (indicated by the box).

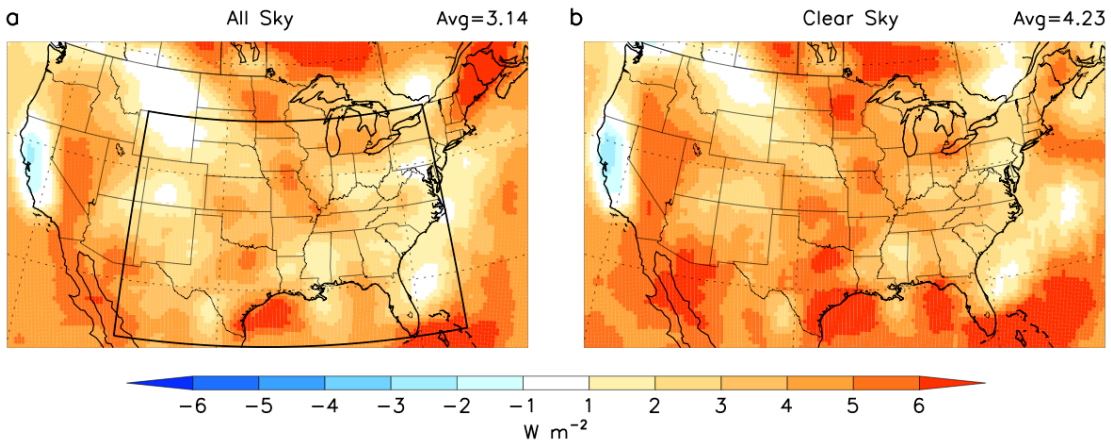


Figure 40. Difference between predicted OLR from WRF-Chem simulation with interactive O_3 and from WRF-Chem simulation with climatological O_3 in longwave radiation scheme. The values are averaged between 2 July and 30 July, 2007 for (a) all sky and (b) clear sky conditions and smoothed spatially (360-km boxcar). The mean value over the eastern two thirds of the United States (indicated by the box in Figure 40a) for each plot is top right.

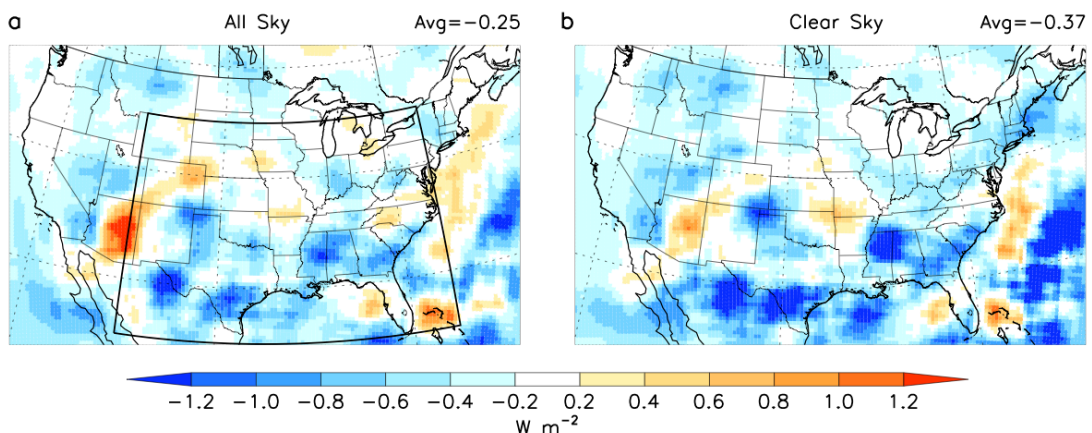


Figure 41. Same as Figure 40 except OLR change due to O_3 produced from LNO_x is shown (the difference between LNO_x -IO simulation and noL-IO simulation).

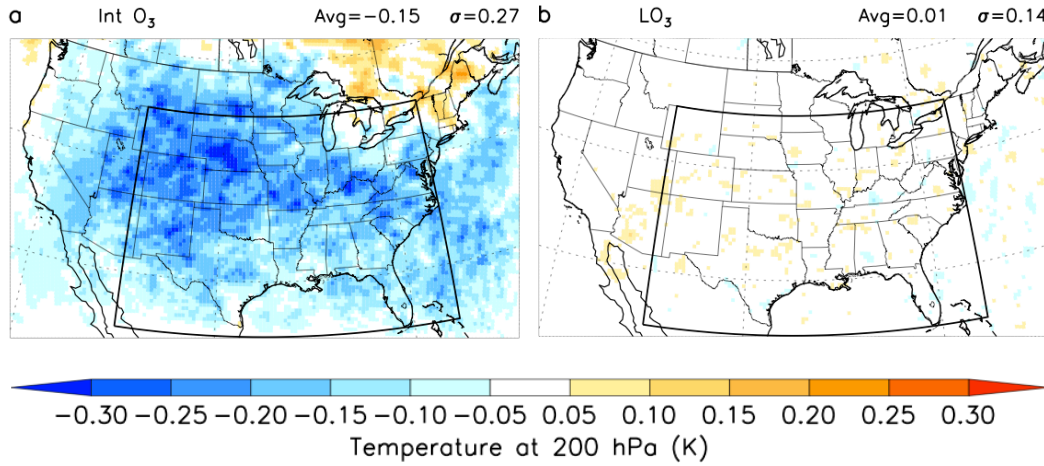


Figure 42. The impact of (a) interactive ozone and (b) ozone due to LNO_x on temperature at 200 hPa for early afternoon (17 UTC) averaged from 29 daily values between 2 July to 30 July 2007. The average and the mean standard deviation (σ) of daily time series at each grid box averaged over the eastern two thirds of the United States (depicted by the box) is top right.

4.4.6 Impact on Daily Fields

The analysis in previous section is focused on the mean impact of interactive ozone because the metric in the IPCC for radiative forcing is the mean over time and space. In this section, we present individual snapshots from four selected simulations to highlight the variations in instantaneous radiative forcing due to interactive ozone on a day-to-day basis.

First, we analyze the impact of interactive ozone on OLR. For brevity, we refer to the simulation with interactive ozone as IO and to the standard simulation

with noninteractive as NIO. Figures 43 and 44 show the OLR impact at the 42-hour and 90-hour simulation times for four selected simulations. As the simulation time increases, the differences between IO and NIO grow. The radiative impacts and feedbacks are the largest at the end of the simulations (i.e., after 90 hours of run time, which is a typical length of simulations by operational mesoscale models). Although one third of grid boxes are clear sky, showing increased OLR (by about 4 W m^{-2}), the changes in OLR are dominated by the changes in cloud distributions (horizontal and vertical). We see great spatial variability with most of the values within the range of $4 \text{ W m}^{-2} \pm 39 \text{ W m}^{-2}$. Large negative values can be explained by (1) cloudy skies in IO that are clear skies in NIO and (2) higher cloud tops in IO compared to NIO. Large positive values can be explained by (1) clear skies in IO that are cloudy skies in NIO and (2) lower cloud tops in IO compared to NIO. Table 5 summarizes the changes in horizontal (cloud cover) and vertical cloud distributions (cloud tops) and resulting OLR changes at the 90-hour simulation times.

The results in Figure 44 and Table 5 indicate that the simulated cloud distributions are sensitive to decreased heating in the upper troposphere due to less O_3 in IO compared to NIO. In general, we see a large spatial variability in OLR because of horizontal cloud displacements and differences in cloud cover and cloud tops between IO and NIO simulations. This suggests that changes seen in Figure 40 showing the impact of interactive ozone on OLR are coupled with changed cloud distributions (vertical and spatial). The same is true for Figure 41 showing the impact of O_3 produced from LNO_x on OLR. At the same time, the changes in cloud distributions are a result of ozone perturbations in the radiation schemes. In order to

calculate the radiative forcing due only to O₃ enhancement, the cloud distributions and other meteorological parameters (i.e., temperature, water vapor profiles and skin temperature) would have to be held constant.

Next, we analyze the impact of interactive ozone on upper tropospheric temperatures. Similar to OLR, the impact is the largest at the end of the simulations. We see that decreased heating due to less O₃ in the UT results in a small cooling effect with most of the temperatures at the 90-hour simulation times within the range of $-0.21^{\circ}\text{C} \pm 0.31^{\circ}\text{C}$ (Figure 45). Figure 46 shows the impact of interactive ozone incorporated only in the longwave radiation scheme. The overall cooling and spatial variability is decreased with most of the values within the range of $-0.14^{\circ}\text{C} \pm 0.21^{\circ}\text{C}$ when compared to combined longwave and shortwave effects of interactive ozone in Figure 45. Shifting our focus to the impact of ozone enhancements due to LNO_x, we see that ozone enhancements from LNO_x result in a small warming of 0.02°C with standard deviation of 0.18°C (Figure 47). As in the case of OLR, the changes in temperature are coupled with altered cloud distributions. Therefore, we see both cooling and warming effect.

The temperature changes drive changes in geopotential heights. The impact of interactive ozone on 200 hPa geopotential heights is small with values mostly <12 m, which is 0.1% of typical 200 hPa geopotential height. However, horizontal gradients of the geopotential heights, important for geostrophic winds, increase by about 25 m (e.g., from Ohio to New York on July 22) resulting in a 3 m s^{-1} change in geostrophic wind.

To summarize, the instantaneous changes of OLR due to interactive ozone are dominated by altered cloud distributions (vertical and horizontal) with large spatial variability and grow as the simulation time increases with the largest effect at the end of the simulation times. Because of less O₃ in interactive simulations, the temperatures in the upper troposphere show a cooling of -0.21°C at the end of the simulation times. The impact of ozone enhancements due to LNO_x on upper troposphere temperature is a factor of 10 smaller warming.

Table 5. Cloud statistics between the simulation with interactive ozone and the standard simulation (noninteractive ozone) at the 90-hour simulation times

Fraction of Grid Boxes	Cloud Cover and Cloud Top Pressure Change	Median OLR change in W m ⁻²
34%	Clear sky in both IO and NIO ^a	4.0
17%	Cloudy sky in IO but clear sky in NIO	-21.0
12%	Clear sky in IO but cloudy sky in NIO	29.0
37%	Cloudy sky in both IO and NIO	3.0
19%	± 5 hPa change in cloud top pressure (IO versus NIO)	2.7
10%	> 5 hPa increase in cloud top pressure (IO versus NIO, with median of +38 hPa)	10.4
8%	< -5 hPa decrease in cloud top pressure (IO versus NIO, with median of -34 hPa)	-3.7
100%	All grid boxes	3.7

^a The simulation with interactive ozone is referred as IO and the simulation with noninteractive ozone is referred as NIO.

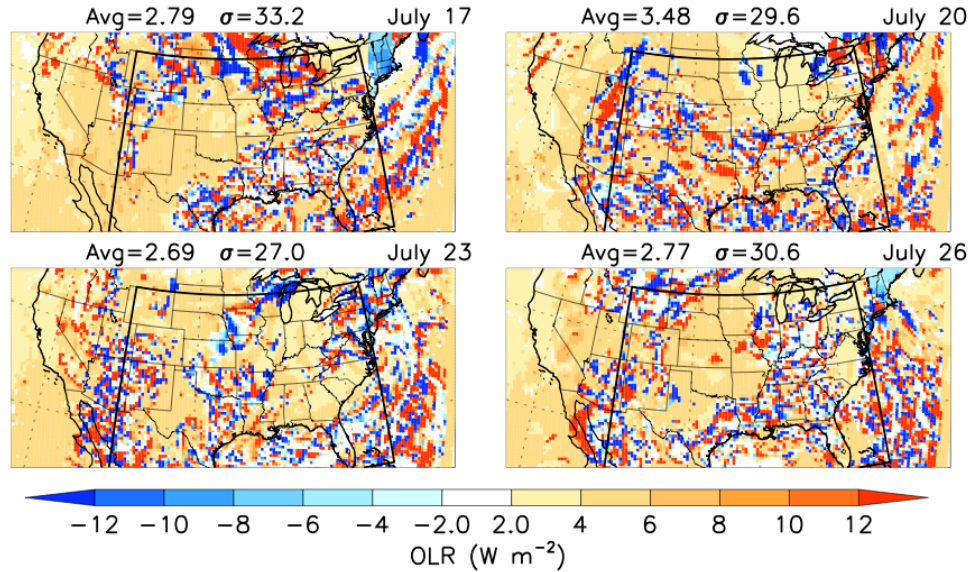


Figure 43. The impact of interactive ozone on OLR (the difference between the simulations with and without interactive ozone) after a 42-hour simulation on July 17 (top left), July 20 (top right), July 23 (bottom left), and July 26 (bottom right). The average and the standard deviation from the eastern two thirds of the United States (depicted by the box) are above.

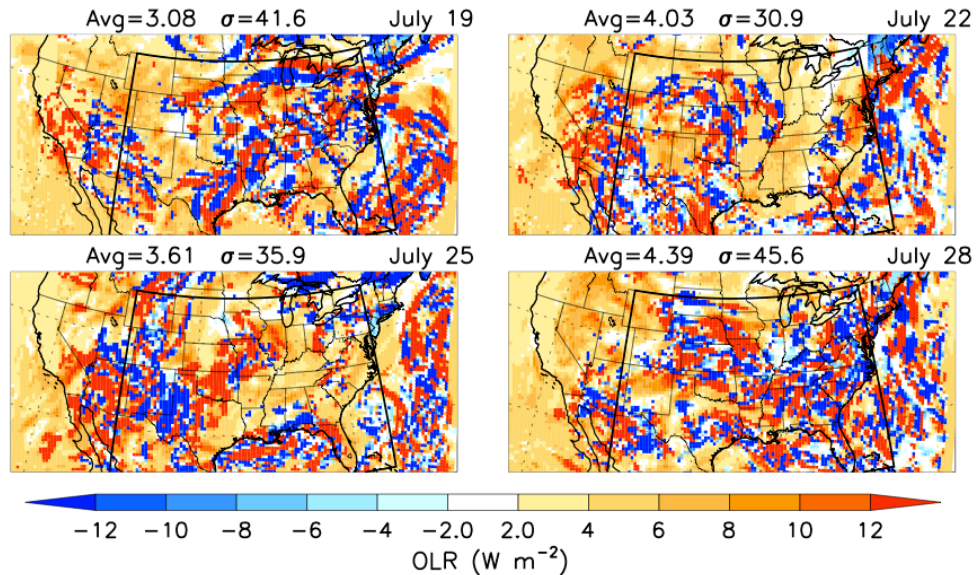


Figure 44. Same as Figure 43 except after a 90-hour simulation on July 19 (top left), July 22 (top right), July 25 (bottom left), and July 28 (bottom right) are shown.

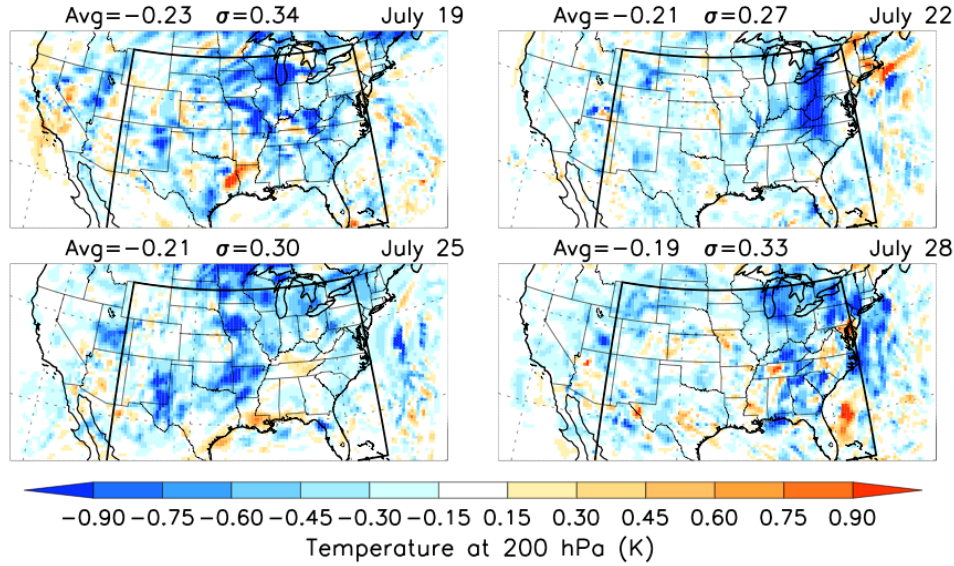


Figure 45. The impact of interactive ozone on temperature at 200 hPa (the difference between the simulations with and without interactive ozone) after a 90-hour simulation on July 17 (top left), July 20 (top right), July 23 (bottom left), and July 26 (bottom right). The average and the standard deviation from the eastern two thirds of the United States (depicted by the box) are above.

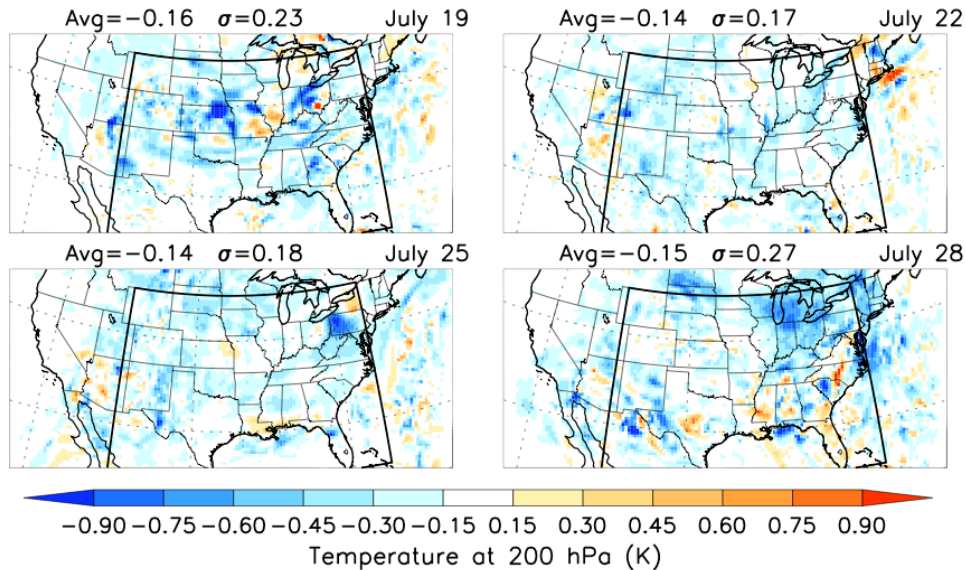


Figure 46. Same as Figure 45 except interactive ozone is only included in the longwave radiation scheme, whereas Figure 45 shows the impact of interactive ozone from both longwave and shortwave radiation.

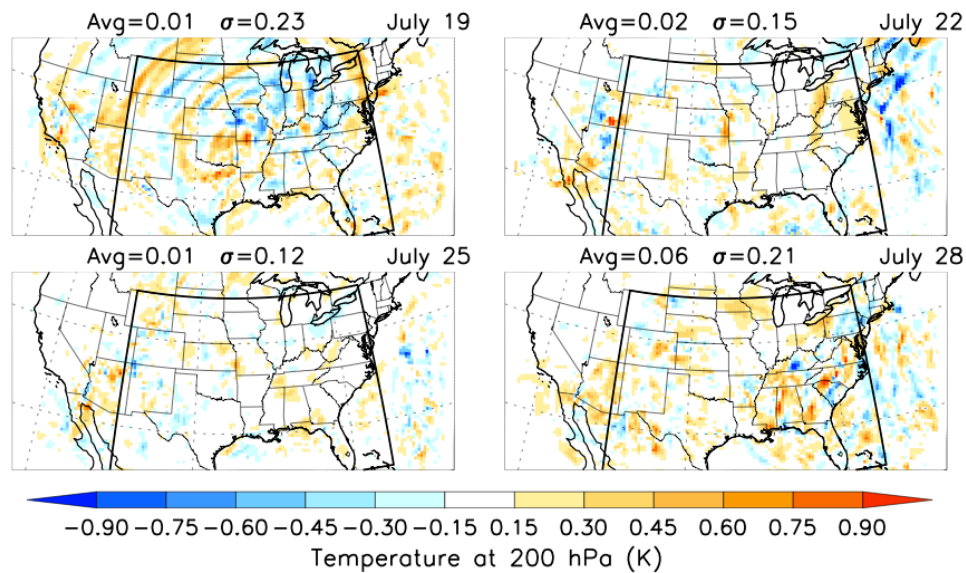


Figure 47. Same as Figure 45 except the impact of ozone due to LNO_x is shown.

4.4.7 Export of Reactive Nitrogen From the Contiguous United States

The sum of oxidized nitrogen compounds, referred to as NO_y, represent not just the key precursor to O₃ but also an important source of nutrients for many ecosystems. Increased anthropogenic emissions have caused excessive deposition of nitrogen to ecosystems leading to eutrophication. The role of deposition from the atmosphere remains uncertain [Reactive Nitrogen in the United States: An Analysis of Inputs, Flows, Consequences and Management Options, A Report of the EPA Science Advisory Board (EPA-SAB-11-013)].

Global chemistry transport models have estimated that 65%–75% of the NO_y emitted over the United States is deposited, and 25%–35% is exported [e.g., Horowitz

et al., 1998; *Park et al.*, 2004b]. In this section, we estimate the export fluxes of NO_y across the western and eastern boundaries of the United States. We define the CONUS boundary layer as the region extending horizontally from 30°N to 50°N with the eastern and western boundaries located about 250 km from the coast. We estimate NO_y as the sum of the following oxidation products: NO_x, NO₃, 2 × N₂O₅, HONO, HNO₃, HNO₄, PAN, and lumped organic nitrates (NTR, called ONIT in *Zaveri and Peters*, [1999]).

Figure 48 shows a vertical cross section of NO_y export fluxes at the east coast of the United States averaged from 6 hour fields over July 2007. The fluxes shown are normalized by the area of the grid box. First, we analyze the fluxes from the simulation with no LNO_x source (Figure 48a). The exports reach a maximum between 40°N and 43°N, downwind of the highly populated region between Washington, D.C. and Boston, Massachusetts. Although a large amount of NO_y is exported below 2.5 km (0.11 Gmol d⁻¹), most of it (0.24 Gmol d⁻¹) is vented out of the boundary layer and exported through the east boundary in the free troposphere (see Table 6).

If we assume that NO_y entering at the west coast is transported directly across the region and exported eastward through the east wall (with no deposition) as is often assumed in the literature [e.g., *Park et al.*, 2004b], the net export flux of NO_y, considering the entire depth of troposphere, is 0.29 Gmol d⁻¹ (the flux of 0.35 Gmol d⁻¹ across the eastern boundary decreased by the flux of 0.06 Gmol d⁻¹ across the western boundary). Our emission into the CONUS boundary layer is 1.25 Gmol d⁻¹. This indicates that 23% of the emission from the boundary layer is exported. If we assume that all NO_y entering at the west coast is deposited within the United States,

the NO_y export is 28% of the boundary layer emission. This range of 23%–28% is likely overestimated due to the fact that the lifetime of NTR in the model is overestimated resulting in higher amounts of NO_y [Saylor and Stein, 2012]. Decreasing the lifetime of NTR would lead to a small increase of HNO₃ deposition, resulting in lower NO_y exports through the eastern boundary. In the current simulation, the export of NTR contributes about 14% to NO_y export (0.05 Gmol d⁻¹ from 0.35 Gmol d⁻¹).

Lightning NO_x greatly enhances NO_y exports through the eastern boundary (Figure 48b) because most of the LNO_x is injected in the upper troposphere (above 8 km) where wet deposition rates are smaller than in the boundary layer. NO_y exports are increased by about 42% to 0.60 Gmol d⁻¹ when the LNO_x source (0.35 Gmol d⁻¹) is included. For a simulation with low LNO_x source, NO_y exports increased by about 24% to 0.46 Gmol d⁻¹ due to lightning. Fang *et al.* [2010], using a different model but similar emissions, reported an increase of 24%–43% of the total United States NO_y export due to lightning. A similar increase due to lightning was seen in the UMD-CTM (section 3.3.4). We estimate that 38% (0.35 Gmol d⁻¹ from 1.6 Gmol d⁻¹) of the total CONUS emissions including LNO_x are exported. For the simulation with low LNO_x source, this percentage is reduced to 26% (net export of 0.37 Gmol d⁻¹ divided by emission of 1.42 Gmol d⁻¹).

To summarize, the NO_y export of 23%–28% of the boundary layer emission and 26%–38% of the total NO_x emission over the CONUS is similar to literature estimates of 25%–35% obtained from using different CTMs in the EPA Report [EPA-SAB-11-013].

Table 6. NO_y Import and Export Fluxes From the Contiguous United States (Gmol d⁻¹)

Simulation	Tropospheric column ^a		Boundary layer (<2.5 km)	
	Import	Export	Import	Export
noL	0.06	0.35	0.00	0.11
LNO _x	0.09	0.60	0.00	0.12
Low LNO _x	0.09	0.46	0.00	0.11

^a The fluxes are calculated for the model levels below the approximate tropopause determined as the level where O₃ concentration reaches 120 ppbv.

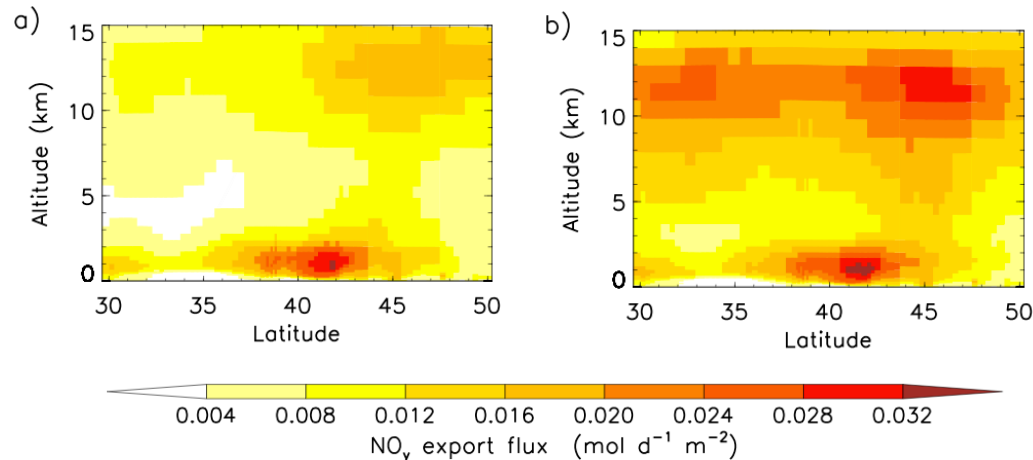


Figure 48. Vertical cross section of NO_y fluxes across the eastern boundary of the contiguous United States (the boundary follows the United States coast and is located 250 km east of the coastline) as a function of latitude during July 2007. Fluxes from the simulation without LNO_x source are shown on the left, fluxes from the simulation with LNO_x source are shown on the right. Positive values indicate eastward fluxes.

4.5 Summary and Conclusions

This study investigates the radiative effects of ozone perturbations in the upper troposphere. We have conducted several sensitivity simulations of July 2007 with the regional scale, fully coupled WRF-Chem driven by meteorological fields from NASA's MERRA reanalysis. The initial and boundary conditions for trace gases are interpolated from NASA's global chemical transport model GMI, which includes combined tropospheric and stratospheric chemistry.

The WRF-Chem model, most commonly configured with the RRTM radiation scheme, assumes one climatological profile of ozone for all latitudes in the longwave radiation scheme, which is the average of standard midlatitude summer and winter ozone profiles. The mean model tropopause is located at higher altitudes than the assumed climatology, so there is much less model ozone between 350 and 200 hPa than in the assumed climatology. Comparisons with ozonesonde measurements confirm that WRF-Chem well captures the ozone concentrations near the tropopause.

In July 2007, the NLDN detected the largest flash rates over the southeastern United States with a clear peak over Florida. This lightning signal over Florida detected by the NLDN network is not as clearly seen in the satellite-retrieved NO₂ columns (DOMINO v2 product). When comparing the model flash rates, this peak was better captured by the new lightning parameterization, which uses mixed phase depth as a flash rate predictor in addition to the standard approach of using convective precipitation. However, the impact of using mixed phase depth on day-to-day variations between model and observed flash rate is small overall, and therefore, there

does not appear to be a benefit to using mixed phase depth as an additional predictor for interactive ozone simulations.

We explore the radiative effects of model ozone by incorporating it into the longwave radiation scheme, thus allowing heating rates from ozone to affect the simulated meteorological and chemical quantities. The mean predicted outgoing longwave radiation (OLR) agrees well with satellite observations. When the climatological ozone profile is used in the longwave radiation scheme, the predicted OLR is 7.1 W m^{-2} lower than the mean satellite-observed OLR (247 W m^{-2}) over the eastern two thirds of the United States. The predicted OLR is 3.1 W m^{-2} closer to satellite observations when the model ozone is incorporated into the longwave radiation scheme due to high bias in climatological ozone profile. The fully coupled interactive ozone framework of the WRF model allows to quantify the OLR changes due to ozone perturbations. The standard simulation with production of $500 \text{ NO mol flash}^{-1}$ resulted in a 22 ppbv ozone enhancement in the upper troposphere. Due to this lightning enhancement, the OLR amounts are reduced by 0.25 W m^{-2} for all sky and 0.37 W m^{-2} for clear sky conditions. The interactive ozone framework allows ozone heating rates to affect the simulated meteorological and chemical quantities. The impact of the interactive O_3 on upper tropospheric temperatures is small (0.15°C averaged over ten 4-day simulations). The monthly mean impact of ozone from LNO_x on temperature is even smaller.

Our WRF-Chem results have been used to estimate the export fluxes of reactive nitrogen at the eastern coast of the United States. We estimate the export of

reactive nitrogen to be 23%–28% of the boundary layer emissions and 26%–38% of the total emissions including LNO_x.

5 Summary and Future Work

5.1 Summary of Global Modeling With the UMD-CTM

We have conducted several simulations of summers 2002 and 2004 with the global chemistry transport model UMD-CTM driven by meteorological fields from the GEOS-4 CERES reanalysis.

Week-to-week variations of lightning flash rates had a much larger impact on ozone tropospheric columns over North America and downwind relative to the large emission reductions that took place between 2002 and 2004 (the NO_x SIP Call). Over the North Atlantic, changes in the ozone column between early summer 2002 and 2004 due to changes in lightning and meteorology exceeded the change due to emission reductions by a factor of 7. Late summer changes in lightning were smaller and had a much smaller impact on ozone columns. Unlike North American anthropogenic emissions, which continue to show a downward trend over recent years, there is no clear trend in lightning flash rate. Therefore this factor of 7 cannot be generalized to other time periods and is derived primarily to demonstrate that the effect of week-to-week lightning variability can be large compared to emission reductions. In the second half of the summer, we see a large impact from lightning after the onset of the North American Monsoon reinforced by the upper level anticyclone centered over Mexico.

In summer 2004, instantaneous radiative forcing (RF) due to ozone produced from anthropogenic emissions ranged from 0.15 to 0.30 W m⁻² across the North Atlantic, while that due to ozone produced from lightning NO emissions ranged from

0.20 to 0.50 W m^{-2} . A 50% increase in flash rate between early summer 2002 and 2004 over the United States corresponds to a 30% increase in RF due to LNO_x. The mean normalized RF per unit of added O₃ column, over the areas with enhancements exceeding 5 DU, was $0.027 \text{ W m}^{-2} \text{ DU}^{-1}$ due to North American anthropogenic enhancements and $0.047 \text{ W m}^{-2} \text{ DU}^{-1}$ due to lightning enhancements. This is because of the larger radiative efficiency of upper tropospheric ozone perturbations.

5.2 Summary of Regional Modeling With the WRF-Chem

We have conducted several month long simulations (each comprised of ten 4-day simulations) of July 2007 with the regional model WRF-Chem driven by meteorological fields from the MERRA reanalysis.

We have tested a new lightning parameterization developed by *Hansen* [2012]. This scheme uses mixed phase depth as a flash rate predictor in addition to the standard approach of using convective precipitation, but for our specific time period it does not significantly improve the model flash rate compared to the standard approach.

Interactive ozone in radiation schemes allows quantifying the changes in outgoing longwave radiation (OLR) due to ozone perturbations. Interactive ozone in WRF-Chem brings the predicted outgoing longwave radiation closer to satellite observations. The mean OLR bias of 7.1 W m^{-2} over the eastern two thirds of the United States is reduced by 3.1 W m^{-2} . The mean OLR reduction due to ozone produced from LNO_x (22 ppbv) over the same region is 0.25 W m^{-2} for all sky and 0.37 W m^{-2} for clear sky conditions.

The impact of using interactive ozone versus climatological ozone on upper tropospheric temperatures is 0.15°C (determined as an average of ten 4-day simulations). The impact of ozone due to LNO_x is small on a monthly mean basis.

5.3 Future Work

The research discussed in this dissertation has left several unanswered questions, which are worth examining in the future. These include the following:

5.3.1 Offline Calculations of Radiative Forcing

In the first part of the dissertation, we showed that ozone enhancements produced from LNO_x are radiatively more efficient (per 1 Dobson unit ozone increment) than ozone enhancements due to ANO_x. These calculations were done offline and for clear skies, where all meteorological parameters were held constant except for ozone. Therefore no temperature and water vapor feedbacks were allowed thus isolating the forcing due only to ozone enhancement.

The ozone distributions were calculated from two UMD-CTM simulations: one that included LNO_x source and one with LNO_x source turned off. These ozone distributions were used as input for the radiative forcing calculation using the Goddard radiative transfer model [Chou *et al.*, 2001]. Future work could include performing an offline calculation of radiative forcing using the ozone distributions calculated by WRF-Chem and the same radiative transfer model. In addition, the radiative forcing could be calculated offline using the RRTM [Mlawer *et al.*, 1997] to provide another estimate of radiative forcing thus accounting for some of the

uncertainty associated with radiative transfer calculations. Results from the online calculations, which also included temperature and water vapor feedbacks were discussed in sections 4.4.4 and 4.4.5.

5.3.2 Short Term Impacts of Interactive Ozone

Using an ensemble of ten simulations, we have shown that the importance of interactive ozone on the UT temperature at the national scale is cooling on the order of 0.2°C with standard deviation of 0.3°C with some increases in cloud cover. As the simulation times were increasing, the impact of interactive ozone grew. The differences at individual locations did not exceed 2°C on the time scale of our experiments (4 days, which is a typical length of regional scale operational forecasting). Reduced heating rate due to less ozone in interactive versus noninteractive simulation is responsible for the increasing magnitude of cooling in time, suggesting that this cooling effect is an important consideration at climate time scales.

The use of interactive ozone enables feedback mechanisms: for example from chemistry (additional ozone due to LNO_x) through radiation (changes in heating rate) to dynamics (changes in atmospheric instability and storm structure) and back to lightning (via convective updrafts and microphysics). The differences in simulations with and without interactive ozone may be explained by both improving the assumed ozone climatology in radiation schemes (with spatial and seasonal variability) as well as enabling these types of feedbacks.

Our 4-day simulations showed that temperature changes due to the additional ozone from LNO_x were smaller than those due to inclusion of interactive ozone. We have not yet tested the impact of interactive ozone in cloud resolving simulations, which is beyond the scope of this project. With explicit convection the feedback mechanisms may play larger role.

Our ensembles demonstrated that the UT cooling resulted in a 5% increase in cloud cover between the two simulations, due to increases in relative humidity in the UT. While interesting, this increase was obtained from simulations with relatively coarse resolution. Confirmation of this result with an ensemble of cloud resolving simulations would be worth exploring since the convection would be explicit rather than parameterized. Results from cloud resolving simulations could then be compared to cloud vertical profiles from the Cloud-Aerosol Lidar and Infrared Pathfinder Satellite Observation (CALIPSO).

5.3.3 Temperature Response of Ozone due to LNO_x in Climate Simulations

Our simulations showed 22 ppbv increase in UT ozone due to LNO_x. On our time scale the temperature response was mainly seen in the UT. We have shown that the instantaneous radiative forcing due to LNO_x is about the same as the instantaneous radiative forcing since preindustrial times shown by *Mickley et al.* [2004]. They conducted climate equilibrium simulations (spun-up for 25 years and ran for 75 years) using a coarse resolution GISS model ($4^\circ \times 5^\circ$ and 9 vertical levels) and found that \sim 18 ppbv increase in ozone throughout the troposphere resulted in a temperature increase of 0.25°C – 0.30°C throughout the troposphere when averaged

globally. It would be worth conducting climate simulations similar to *Mickley et al.*, but with a high resolution global or regional chemistry climate model, to investigate the long term temperature response due to ozone resulting from LNO_x. Further analysis could explore whether the flash rate has changed since preindustrial times and whether it will be different as climate changes.

5.3.4 Wind Shear Climatology and New Lightning Scheme

The maxima in lightning flash rates over Florida that are detected by the NLDN network are not as clearly seen in the satellite-retrieved NO₂ columns (DOMINO v2 product) indicating that the flashes over the southeastern United States may be more tropical in nature and therefore producing less NO moles than their midlatitude counterparts. Most tropical thunderstorms have smaller vertical wind shear resulting in shorter flash lengths, which may lead to smaller NO production per flash [*Huntrieser et al.*, 2009]. Further studies could investigate whether there is a significant difference between the wind shear of the storms in Florida and parts of the southeastern United States compared to more continental storms. If so, a new lightning algorithm could include wind shear as a predictor of NO production per flash. This could potentially result in better agreement with NO₂ columns observed from space.

5.3.5 Impact of Boundary Conditions on Surface Layer

Mean regional ozone biases at the surface, as well as in the free troposphere, can be increased if a high O₃ bias is introduced from a global CTM to lateral

boundary conditions [*Tang et al.*, 2008; *Yegorova et al.*, 2011]. The WRF-Chem community usually uses the output from the MOZART model when preparing initial and boundary conditions for trace gases. As part of this dissertation, we have developed new software that prepares initial and boundary conditions from the GMI CTM. Trace gases from the GMI CTM have not been used to drive regional air quality models before. This software can serve as a useful tool to investigate the impact of boundary conditions on air quality model performance and regional ozone biases.

In order to drive WRF-Chem simulations with GMI-CTM trace gases, the GMI-CTM output needs to be provided at least a 6-hour frequency. The WRF-Chem community would benefit if the GMI-CTM output were to be archived at this frequency. I have run the GMI-CTM using a graphical user interface on a computing facility at NASA; however, this is not an option for those who do not have access to the NASA computing facility. Ideally, the users would be able to run the GMI-CTM interactively on a website employing a similar graphical user interface.

Acronyms and Abbreviations

AGL	above ground level
ANO _x	anthropogenic NO _x
AQS	Air Quality System sites
BEIS	Biogenic Emissions Inventory System
BL	boundary layer
CASA	Carnegie-Ames-Stanford Approach biogeochemical model
CBM-Z	Carbon Bond Mechanism modified by Zaveri and Peters [1999]
CEMS	Continuous Emission Monitoring System
CERES	Clouds and the Earth's Radiant Energy System (reanalysis)
CMAQ	Community Multiscale Air-Quality model
CG	cloud to ground
CH ₄	methane
CO	carbon monoxide
CONUS	Contiguous United States
CRYSTAL-FACE	Cirrus Regional Study of Tropical Anvils and Cirrus Layers-Florida Area Cirrus
CTM	Chemistry Transport Model
DOMINO	Dutch OMI NO ₂ product
EDGAR	Emission Database for Global Atmospheric Research
EPA	United States Environmental Protection Agency
EULINOX	European Lightning Nitrogen Oxides
GEOS	Goddard Earth Observing System
GEOS-Chem	A global 3-D chemical transport model (driven by GEOS meteorology)
GISS	Goddard Institute for Space Studies General Circulation Model
GMI	Global Modeling Initiative CTM
HNO ₃	nitric acid
IC	intracloud or intercloud
IC/BC	initial and boundary conditions
INTEX	Intercontinental Chemical Transport Experiment aircraft campaign
IONS	INTEX Ozonesonde Network Study
IPCC	Intergovernmental Panel on Climate Change
LIS	Lightning Imaging Sensor
LMA	Lightning Mapping Array
LNOM	Lightning Nitrogen Oxides Model
LNO _x	lightning NO _x
LS	lower stratosphere
LST	Local Standard Time
MERRA	Modern Era Retrospective-Analysis for Research and Applications (NASA's reanalysis)
MODIS	Moderate-resolution Imaging Spectroradiometer
MOVES	Motor Vehicle Emission Simulator
MOZAIC	Model for Simulating Aerosol Interactions and Chemistry
MOZART	Model for Ozone and Related chemical Tracers

NA	North American
NAAQS	National Ambient Air Quality Standard
NASA	National Aeronautics and Space Administration agency
NARR	North American Regional Reanalysis
NEI	EPA's National Emissions Inventory
NCAR/ACD	NCAR's Atmospheric Chemistry Division
NCEP	National Center for Environmental Prediction, U.S.
NLDN	National Lightning Detection Network
NOAA	National Oceanic and Atmospheric Administration agency
NO	nitrogen oxide
NO ₂	nitrogen dioxide
NO _x	nitrogen oxides (NO + NO ₂)
NO _y	total reactive nitrogen
O ₃	ozone
OH	hydroxyl radical
OLR	outgoing longwave radiation
OMI	Ozone Monitoring Instrument
ORV	Ohio River Valley (Pennsylvania, Ohio, West Virginia, Kentucky, Indiana and Illinois)
OTD	Optical Transient Detector (detects lightning from space)
PAN	peroxyacetyl nitrate
REAM	A regional chemical transport model
RF	Longwave contribution of the net downward Radiative Flux at the tropopause for clear-sky conditions (instantaneous radiative forcing)
RRTM	Rapid Radiative Transfer Model
SAD	segment altitude distribution
SCIAMACHY	Scanning Imaging Absorption Spectrometer for Atmospheric Chartography/Chemistry
SMOKE	Sparse Matrix Operator Kernel Emissions modeling system
SIP	State Implementation Plan
STERAO	Stratosphere-Troposphere Experiment—Radiation, Aerosols, Ozone
Synoz	Synthetic O ₃ scheme
TES	Tropospheric Emission Spectrometer
TM4	A global 3-D chemical transport model (driven by ECMWF meteorology)
U.S.	United States
UMD-CTM	University of Maryland CTM
UT	upper troposphere
UT/LS	upper troposphere and lower stratosphere
UTC	Coordinated Universal Time
VHF	Very High Frequency
VOC	volatile organic compound
WRF	Weather Research and Forecasting model
WRF-Chem	WRF with online chemistry

Bibliography

- van der A, R. J., D. H. M. U. Peters, H. J. Eskes, K. F. Boersma, M. V. Roozendael, I. De Smedt, and H. M. Kelder (2006), Detection of the trend and seasonal variation in tropospheric NO₂ over China, *J. Geophys. Res.*, 111(D12317), doi:10.1029/2005JD006594. J
- Aghedo, A. M., K. W. Bowman, H. M. Worden, S. S. Kulawik, D. T. Shindell, J. F. Lamarque, G. Faluvegi, M. Parrington, D. B. A. Jones, and S. Rast (2011), The vertical distribution of ozone instantaneous radiative forcing from satellite and chemistry climate models, *Journal of Geophysical Research*, 116(D1), doi:10.1029/2010JD014243. J
- Allen, D. J., R. B. Rood, A. M. Thompson, and R. D. Hudson (1996), Three-dimensional radon 222 calculations using assimilated meteorological data and a convective mixing algorithm, *J. Geophys. Res.*, 101(3), 6871–6881. J
- Allen, D. J., K. E. Pickering, B. N. Duncan, and M. R. Damon (2010), Impact of lightning NO emissions on North American photochemistry as determined using the Global Modeling Initiative (GMI) model, *J. Geophys. Res.*, 115, doi:201010.1029/2010JD014062. J
- Allen, D. J., K. E. Pickering, R. W. Pinder, B. H. Henderson, K. W. Appel, and A. Prados (2012), Impact of lightning-NO on eastern United States photochemistry during the summer of 2006 as determined using the CMAQ model, *Atmospheric Chemistry and Physics*, 12(4), 1737–1758, doi:10.5194/acp-12-1737-2012. J
- Anderson, G. P., S. A. Clough, F. X. Kneizys, J. H. Chetwynd, and E. P. Shettle (1986), *AFGL Atmospheric Constituent Profiles (0-120 km)*, Air Force Geophys. Lab., Bedford, MA. X
- Andreae, M. O., and P. Merlet (2001), Emission of trace gases and aerosols from biomass burning, *Global Biogeochem. Cycles*, 15(4), 955–966. J
- Bertram, T. H. et al. (2007), Direct measurements of the convective recycling of the upper troposphere, *Science*, 315(5813), 816–820. J
- Bey, I., D. J. Jacob, J. A. Logan, and R. M. Yantosca (2001), Asian chemical outflow to the Pacific in spring: Origins, pathways, and budgets, *J. Geophys. Res.*, 106(D19), 23097–23113. J
- Biagi, C. J., K. L. Cummins, K. E. Kehoe, and E. P. Krider (2007), National Lightning Detection Network (NLDN) performance in southern Arizona,

- Texas, and Oklahoma in 2003-2004, *Journal of Geophysical Research-Atmospheres*, 112(D5), doi:10.1029/2006jd007341. J
- Bian, H., and M. J. Prather (2002), Fast-J2 Accurate Simulation of Stratospheric Photolysis in Global Chemical Models, *J. Atmos. Chem.*, 41, 281–296. J
- Blitz, M. A., D. E. Heard, M. J. Pilling, S. R. Arnold, and M. P. Chipperfield (2004), Pressure and temperature-dependent quantum yields for the photodissociation of acetone between 279 and 327.5 nm (vol 31, art no L07110, 2004), *Geophysical Research Letters*, 31(9), doi:10.1029/2004gl020182. J
- Bloom, S. et al. (2005), Documentation and validation of the Goddard Earth Observing System (GEOS) data assimilation system – version 4, *Tech. Report Series on Global Modeling and Data Assimilation*, 104606(26). T. Report
- Boccippio, D. J., K. L. Cummins, H. J. Christian, and S. J. Goodman (2001), Combined satellite- and surface-based estimation of the intracloud-cloud-to-ground lightning ratio over the continental United States, *Monthly Weather Review*, 129(1), 108–122. J
- Boccippio, D. J., W. J. Koshak, and R. J. Blakeslee (2002), Performance assessment of the optical transient detector and lightning Imaging sensor. Part I: Predicted diurnal variability, *Journal of Atmospheric and Oceanic Technology*, 19(9), 1318–1332. J
- Boersma, K. F. et al. (2007), Near-real time retrieval of tropospheric NO₂ from OMI, *Atmos. Chem. Phys.*, 7(8), 2103–2118. J
- Boersma, K. F. et al. (2011), An improved tropospheric NO₂ column retrieval algorithm for the Ozone Monitoring Instrument, *Atmospheric Measurement Techniques Discussions*, 4, 2329–2388, doi:10.5194/amtd-4-2329-2011. J
- Bosilovich, M. G., F. R. Robertson, and J. Chen (2011), Global Energy and Water Budgets in MERRA, *Journal of Climate*, 24(22), 5721–5739, doi:10.1175/2011JCLI4175.1. J
- Bousserez, N. et al. (2007), Evaluation of the MOCAGE chemistry transport model during the ICARTT/ITOP experiment, *Journal of Geophysical Research-Atmospheres*, 112(D10s42), doi:10.1029/2006jd007595. J
- Büker, M. L., M. H. Hitchman, G. J. Tripoli, R. B. Pierce, E. V. Browell, and J. A. Al-Saadi (2008), Long-range convective ozone transport during INTEX, *J. Geophys. Res.*, 113(D14S90), doi:10.1029/2007JD009345. J
- Celarier, E., and C. Retscher (2009), *OMNO2e data product readme file*. [online] Available from: http://toms.gsfc.nasa.gov/omi/no2/OMNO2e_DP_Readme.pdf X

- Chapman, E. G., W. I. Gustafson Jr., R. C. Easter, J. C. Barnard, S. J. Ghan, M. S. Pekour, and J. D. Fast (2009), Coupling aerosol-cloud-radiative processes in the WRF-Chem model: Investigating the radiative impact of elevated point sources, *Atmos. Chem. Phys.*, 9(3), 945–964, doi:10.5194/acp-9-945-2009. J
- Chen, T., W. B. Rossow, and Y. Zhang (2000), Radiative Effects of Cloud-Type Variations, *Journal of Climate*, 13(1), 264–286, doi:10.1175/1520-0442(2000)013<0264:REOTV>2.0.CO;2. J
- Choi, Y., Y. Wang, T. Zeng, D. Cunnold, E.-S. Yang, R. Martin, K. Chance, V. Thouret, and E. Edgerton (2008), Springtime transitions of NO₂, CO, and O₃ over North America: Model evaluation and analysis, *J. Geophys. Res.*, 113, doi:10.1029/2007JD009632. J
- Choi, Y., J. Kim, A. Eldering, G. Osterman, Y. L. Yung, Y. Gu, and K. N. Liou (2009), Lightning and anthropogenic NO_x sources over the United States and the western North Atlantic Ocean: Impact on OLR and radiative effects, *Geophysical Research Letters*, 36, L17806, doi:10.1029/2009gl039381. J
- Chou, M.-D., and M. J. Suarez (1999), A solar radiation parameterization for atmospheric studies, *NASA Tech. Rep. NASA/TM-1999-10460*, 15, 38 pp. T. Report
- Chou, M.-D., M. J. Suarez, X. Z. Liang, and M. M.-H. Yan (2001), A thermal infrared radiation parameterization for atmospheric studies, *NASA Tech. Rep. NASA/TM-2001-104606*, 19, 56 pp. NASA Goddard Space Flight Cent., Greenbelt, MD. T. Report
- Christian, H. J. et al. (2003), Global frequency and distribution of lightning as observed from space by the Optical Transient Detector, *Journal of Geophysical Research-Atmospheres*, 108(D1), doi:10.1029/2002jd002347. J
- Clough, S. A., and M. J. Iacono (1995), Line-by-line calculation of atmospheric fluxes and cooling rates 2. Application to carbon dioxide, ozone, methane, nitrous oxide and the halocarbons, *Journal of Geophysical Research*, 100(D8), 16519–16535, doi:10.1029/95JD01386. J
- Clough, S. A., M. W. Shephard, E. J. Mlawer, J. S. Delamere, M. J. Iacono, K. Cady-Pereira, S. Boukabara, and P. D. Brown (2005), Atmospheric radiative transfer modeling: a summary of the AER codes, *Journal of Quantitative Spectroscopy and Radiative Transfer*, 91(2), 233–244, doi:10.1016/j.jqsrt.2004.05.058. J
- Cooper, O. R. et al. (2006), Large upper tropospheric ozone enhancements above midlatitude North America during summer: In situ evidence from the IONS and MOZAIC ozone measurement network, *Journal of Geophysical Research-Atmospheres*, 111(D24s05), doi:10.1029/2006jd007306. J

- Cooper, O. R. et al. (2009), Summertime buildup and decay of lightning NO_x and aged thunderstorm outflow above North America, *Journal of Geophysical Research-Atmospheres*, 114, doi:10.1029/2008jd010293. J
- Cummins, K. L., M. J. Murphy, E. A. Bardo, W. L. Hiscox, R. B. Pyle, and A. E. Pifer (1998), A combined TOA/MDF Technology Upgrade of the US National Lightning Detection Network, *Journal of Geophysical Research-Atmospheres*, 103(D8), 9035–9044. J
- Cummins, K. L., J. A. Cramer, C. J. Biagi, E. P. Krider, J. Jerauld, M. A. Uman, and V. A. Rakov (2006), The U.S. National Lightning Detection Network: Post-Upgrade Status, *2nd Conference on Meteorological Applications of Lightning Data*. C
- Dahlmann, K., V. Grewe, M. Ponater, and S. Matthes (2011), Quantifying the contributions of individual NO_x sources to the trend in ozone radiative forcing, *Atmospheric Environment*, 45(17), 2860–2868, doi:10.1016/j.atmosenv.2011.02.071. J
- DeCaria, A. J., K. E. Pickering, G. L. Stenchikov, J. R. Scala, J. L. Stith, J. E. Dye, B. A. Ridley, and P. Laroche (2000), A cloud-scale model study of lightning-generated NO_x in an individual thunderstorm during STERAO-A, *J. Geophys. Res.*, 105(D9), 11601–11616. J
- DeCaria, A. J., K. E. Pickering, G. L. Stenchikov, and L. E. Ott (2005), Lightning-generated NO_x and its impact on tropospheric ozone production: A three-dimensional modeling study of a Stratosphere-Troposphere Experiment: Radiation, Aerosols and Ozone (STERAO-A) thunderstorm, *J. Geophys. Res.*, 110(D14). J
- Derwent, R. G., D. S. Stevenson, R. M. Doherty, W. J. Collins, M. G. Sanderson, and C. E. Johnson (2008), Radiative forcing from surface NO_x emissions: spatial and seasonal variations, *Climatic Change*, 88(3-4), 385–401, doi:10.1007/s10584-007-9383-8. J
- Dickerson, R. R. et al. (1987), Thunderstorms: An important mechanism in the transport of air pollutants, *Science*, 235(4787), 460–464. P
- Douglass, A. R., R. S. Stolarski, S. E. Strahan, and P. S. Connell (2004), Radicals and reservoirs in the GMI chemistry and transport model: Comparison to measurements, *Journal of Geophysical Research-Atmospheres*, 109(D16302), doi:10.1029/2004jd004632. J
- Duncan, B. N., S. E. Strahan, Y. Yoshida, S. D. Steenrod, and N. Livesey (2007), Model study of the cross-tropopause transport of biomass burning pollution, *Atmos. Chem. Phys.*, 7, 3713–3736. J

- Duncan, B. N., J. J. West, Y. Yoshida, A. M. Fiore, and J. R. Ziemke (2008), The influence of European pollution on ozone in the Near East and northern Africa, *Atmospheric Chemistry and Physics*, 8(8), 2267–2283. J
- Dunlea, E. J., and A. R. Ravishankara (2004), Kinetic studies of the reactions of O(1D) with several atmospheric molecules, *Physical Chemistry Chemical Physics*, 6(9), 2152, doi:10.1039/b400247d. J
- Emmons, L. K. et al. (2010), Description and evaluation of the Model for Ozone and Related chemical Tracers, version 4 (MOZART-4), *Geosci. Model Dev.*, 3(1), 43–67. J
- Environmental Protection Agency (2005), *Evaluating ozone control programs in the eastern United States: Focus on the NO_x budget trading program, 2004*, Washington, D.C. [online] Available from: http://epa.gov/airtrends/2005/ozonenbpwww.smoke-model.org/version2.7/SMOKE_v27_manual.pdf X
- Fang, Y., A. M. Fiore, L. W. Horowitz, H. Levy II, Y. Hu, and A. G. Russell (2010), Sensitivity of the NO_x budget over the United States to anthropogenic and lightning NO_x in summer, *Journal of Geophysical Research-Atmospheres*, 115(D18312), 16, doi:10.1029/2010jd014079. J
- Fast, J. D., W. I. Gustafson, R. C. Easter, R. A. Zaveri, J. C. Barnard, E. G. Chapman, G. A. Grell, and S. E. Peckham (2006), Evolution of ozone, particulates, and aerosol direct radiative forcing in the vicinity of Houston using a fully coupled meteorology-chemistry-aerosol model, *Journal of Geophysical Research-Atmospheres*, 111(D21), doi:10.1029/2005jd006721. J
- Fehr, T., H. Höller, and H. Huntrieser (2004), Model study on production and transport of lightning-produced NO_x in a EULINOX supercell storm, *Journal of Geophysical Research*, 109(D9), doi:10.1029/2003JD003935. J
- Fehsenfeld, F. C. et al. (2006), International Consortium for Atmospheric Research on Transport and Transformation (ICARTT): North America to Europe - Overview of the 2004 summer field study, *J. Geophys. Res.*, 111(D23). J
- Friedl, M. A. et al. (2002), Global land cover mapping from MODIS: algorithms and early results, *Remote Sens. Environ.*, 83, 287–302. J
- Frost, G. J. et al. (2006), Effects of changing power plant NO_x emissions on ozone in the eastern United States: Proof of concept, *J. Geophys. Res.*, 111(D12). J
- Fu, Q., and K. N. Liou (1992), On the Correlated k-Distribution Method for Radiative Transfer in Nonhomogeneous Atmospheres, *Journal of the Atmospheric Sciences*, 49(22), 2139–2156, doi:10.1175/1520-0469(1992)049<2139:OTCDMF>2.0.CO;2. J

- Fuelberg, H. E., M. J. Porter, C. M. Kiley, J. J. Halland, and D. Morse (2007), Meteorological conditions and anomalies during the Intercontinental Chemical Transport Experiment–North America, *J. Geophys. Res.*, 112(D12S06), doi:10.1029/2006JD007734. J
- Gao, X., J. Li, and S. Sorooshian (2007), Modeling intraseasonal features of 2004 North American monsoon precipitation, *Journal of Climate*, 20(9), 1882–1896, doi:10.1175/jcl14100.1. J
- Gauss, M. et al. (2003), Radiative forcing in the 21st century due to ozone changes in the troposphere and the lower stratosphere, *Journal of Geophysical Research-Atmospheres*, 108(D9), doi:10.1029/2002jd002624. J
- Giglio, L., G. R. van der Werf, J. T. Randerson, G. J. Collatz, and P. Kasibhatla (2006), Global estimation of burned area using MODIS active fire observations, *Atmos. Chem. Phys.*, 6, 957–974. J
- Gilliland, A. B., C. Hogrefe, R. W. Pinder, J. M. Godowitch, K. L. Foley, and S. T. Rao (2008), Dynamic evaluation of regional air quality models: Assessing changes in O₃ stemming from changes in emissions and meteorology, *Atmospheric Environment*, 42(20), 5110–5123, doi:10.1016/j.atmosenv.2008.02.018. J
- Godowitch, J. M., A. B. Gilliland, R. R. Draxler, and S. T. Rao (2008), Modeling assessment of point source NO_x emission reductions on ozone air quality in the eastern United States, *Atmospheric Environment*, 42, 87–100, doi:10.1016/j.atmosenv.2007.09.032. J
- Grell, G. A., S. E. Peckham, R. Schmitz, S. A. McKeen, G. Frost, W. C. Skamarock, and B. Eder (2005), Fully coupled “online” chemistry within the WRF model, *Atmospheric Environment*, 39(37), 6957–6975, doi:10.1016/j.atmosenv.2005.04.027. J
- Guenther, A., T. Karl, P. Harley, C. Wiedinmyer, P. I. Palmer, and C. Geron (2006), Estimates of global terrestrial isoprene emissions using MEGAN (Model of Emissions of Gases and Aerosols from Nature), *Atmospheric Chemistry and Physics*, 6, 3181–3210. J
- Gustafson, W. I., E. G. Chapman, S. J. Ghan, R. C. Easter, and J. D. Fast (2007), Impact on modeled cloud characteristics due to simplified treatment of uniform cloud condensation nuclei during NEAQS 2004, *Geophysical Research Letters*, 34(19), doi:10.1029/2007GL030021. J
- Hack, J. J. (1994), Parameterization of moist convection in the National Center for Atmospheric Research community climate model (CCM2), *J. Geophys. Res.*, 99, 5551–5568. J

- Hansen, A. E. (2012), Development of a Regional Lightning NO_x Parameterization for the Weather and Research Forecast Chemistry Model, *Ph.D. dissertation*, 105 pp., The Florida State University. *thesis*
- Hansen, M. C., R. S. Defries, J. R. G. Townshend, and R. Sohlberg (2000), Global land cover classification at 1km spatial resolution using a classification tree approach, *Int. J. Remote Sensing*, 21, 1331–1364. *J*
- Heald, C. L., D. J. Jacob, P. I. Palmer, M. J. Evans, G. W. Sachse, H. B. Singh, and D. R. Blake (2003), Biomass burning emission inventory with daily resolution: Application to aircraft observations of Asian outflow, *J. Geophys. Res.*, 108, doi:10.1029/2002JD003082. *J*
- Henderson, B. et al. (2010), Evaluation of simulated photochemical partitioning of oxidized nitrogen in the upper troposphere, *Atmos. Chem. Phys. Discuss.*, 10, 20125–20165, doi:10.5194/acpd-10-20125-2010. *J*
- Henderson, B. H. et al. (2011), Evaluation of simulated photochemical partitioning of oxidized nitrogen in the upper troposphere, *Atmospheric Chemistry and Physics*, 11(1), 275–291, doi:10.5194/acp-11-275-2011. *J*
- Hogrefe, C., B. Lynn, K. Civerolo, J. Y. Ku, J. Rosenthal, C. Rosenzweig, R. Goldberg, S. Gaffin, K. Knowlton, and P. L. Kinney (2004), Simulating changes in regional air pollution over the eastern United States due to changes in global and regional climate and emissions, *J. Geophys. Res.*, 109(D22), doi:10.1029/2004JD004690. *J*
- Horowitz, L. W., J. Y. Liang, G. M. Gardner, and D. J. Jacob (1998), Export of reactive nitrogen from North America during summertime: Sensitivity to hydrocarbon chemistry, *J. Geophys. Res.*, 103(D11), 13451–13476. *J*
- Hudman, R. C. et al. (2007), Surface and lightning sources of nitrogen oxides over the United States: Magnitudes, chemical evolution, and outflow, *J. Geophys. Res.*, 112(D12), doi:10.1029/2006JD007912. *J*
- Hudman, R. C., L. T. Murray, D. J. Jacob, S. Turquety, S. Wu, D. B. Millet, M. Avery, A. H. Goldstein, and J. Holloway (2009), North American influence on tropospheric ozone and the effects of recent emission reductions: Constraints from ICARTT observations, *Journal of Geophysical Research-Atmospheres*, 114(D07302), 9, doi:10.1029/2008JD010126. *J*
- Huntrieser, H. et al. (2009), NO_x production by lightning in Hector: first airborne measurements during SCOUT-O3/ACTIVE, *Atmospheric Chemistry and Physics*, 9(21), 8377–8412, doi:10.5194/acp-9-8377-2009. *J*

- Hyer, E. J., E. S. Kasischke, and D. J. Allen (2007), Effects of source temporal resolution on transport simulations of boreal fire emissions, *J. Geophys. Res.*, 112, D01302. J
- Intergovernmental Panel on Climate Change (IPCC) (2007), *Climate Change 2007: The Physical Science Basis. Contribution of Working Group I to the Fourth Assessment Report of the Intergovernmental Panel on Climate Change*, Cambridge, United Kingdom and New York, NY, USA. B
- Jacobson, M. Z. (1995), Computation of global photochemistry with SMVGEAR II, *Atmospheric Environment*, 29(18), 2541–2546, doi:10.1016/1352-2310(95)00194-4. J
- Jet Propulsion Laboratory (2006), Chemical kinetics and photochemical data for use in atmospheric studies, *JPL Publ.*, 06-2, Pasadena, Calif. J
- Jourdain, L., S. S. Kulawik, H. M. Worden, K. E. Pickering, J. Worden, and A. M. Thompson (2010), Lightning NO_x emissions over the USA constrained by TES ozone observations and the GEOS-Chem model, *Atmospheric Chemistry and Physics*, 10(1), 107–119, doi:10.5194/acp-10-107-2010. J
- Justice, C. O., L. Giglio, S. Korontzi, J. Owens, J. T. Morissette, D. Roy, J. Descloitres, S. Alleaume, F. Petitcolin, and Y. Kaufman (2002), The MODIS Fire Products, *Remote Sens. Environ.*, 83, 244–262. J
- Kain, J. S. (2004), The Kain–Fritsch Convective Parameterization: An Update, *Journal of Applied Meteorology*, 43(1), 170–181, doi:10.1175/1520-0450(2004)043<0170:TKCPAU>2.0.CO;2. J
- Kasischke, E. S., E. J. Hyer, P. C. Novelli, L. P. Bruhwiler, N. H. F. French, A. I. Sukhinin, J. H. Hewson, and S. B. J. (2005), Influences of boreal fire emissions on Northern Hemisphere atmospheric carbon and carbon monoxide, *Global Biogeochem. Cycles*, 19(GB1012), doi:10.1029/2004GB002300. J
- Kaynak, B., Y. Hu, R. V. Martin, A. G. Russell, Y. Choi, and Y. Wang (2008), The effect of lightning NOx production on surface ozone in the continental United States, *Atmospheric Chemistry and Physics*, 8(17), 5151–5159. J
- Kiley, C. M., and H. E. Fuelberg (2006), An examination of summertime cyclone transport processes during Intercontinental Chemical Transport Experiment (INTEX-A), *J. Geophys. Res.*, 111(D24S06), doi:10.1029/2006JD007115. J
- Kim, S. W., A. Heckel, S. A. McKeen, G. J. Frost, E. Y. Hsie, M. K. Trainer, A. Richter, J. P. Burrows, S. E. Peckham, and G. A. Grell (2006), Satellite-observed US power plant NOx emission reductions and their impact on air quality, *Geophys. Res. Lett.*, 33(22). J

- Koo, B., C.-J. Chien, G. Tonnesen, R. Morris, J. Johnson, T. Sakulyanontvittaya, P. Piyachaturawat, and G. Yarwood (2010), Natural emissions for regional modeling of background ozone and particulate matter and impacts on emissions control strategies, *Atmospheric Environment*, 44(19), 2372–2382, doi:10.1016/j.atmosenv.2010.02.041. J
- Koshak, and H. S. Peterson (2011), *A summary of the NASA Lightning Nitrogen Oxides Model (LNOM) and recent results*, 10th Annual CMAS Conference, Chapel Hill, 6 pp. C
- Koshak, W. J., H. S. Peterson, E. W. McCaul, and A. Bazar (2010), Estimates of the Lightning NO_x Profile in the Vicinity of the North Alabama Lightning Mapping Array, *21st International Lightning Detection Conference (ILDC)/Vaisala, 18-22 Apr. 2010, Orlando, FL, United States*, 54. C
- Labrador, L. J., R. von Kuhlmann, and M. G. Lawrence (2005), The effects of lightning-produced NO_x and its vertical distribution on atmospheric chemistry: sensitivity simulations with MATCH-MPIC, *Atmospheric Chemistry and Physics*, 5, 1815–1834. J
- Lacis, A. A., D. J. Wuebbles, and J. A. Logan (1990), Radiative Forcing of Climate By Changes In the Vertical-Distribution of Ozone, *Journal of Geophysical Research-Atmospheres*, 95(D7), 9971–9981. J
- Lamsal, L. N., R. V. Martin, A. Padmanabhan, A. van Donkelaar, Q. Zhang, C. E. Sioris, K. Chance, T. P. Kurosu, and M. J. Newchurch (2011), Application of satellite observations for timely updates to global anthropogenic NO_x emission inventories, *Geophysical Research Letters*, 38(5), doi:10.1029/2010GL046476. J
- Lelieveld, J., and P. J. Crutzen (1994), Role of deep cloud convection in the ozone budget of the troposphere, *Science*, 264, 1759–1761. J
- Li, J., X. Gao, R. A. Maddox, and S. Sorooshian (2004), Model study of evolution and diurnal variations of rainfall in the north American monsoon during June and July 2002, *Monthly Weather Review*, 132(12), 2895–2915. J
- Li, Q. B. et al. (2002), Transatlantic transport of pollution and its effects on surface ozone in Europe and North America, *Journal of Geophysical Research-Atmospheres*, 107(D13), 4166, doi:10.1029/2001jd001422. J
- Li, Q. B., D. J. Jacob, R. Park, Y. X. Wang, C. L. Heald, R. Hudman, R. M. Yantosca, R. V. Martin, and M. Evans (2005), North American pollution outflow and the trapping of convectively lifted pollution by upper-level anticyclone, *Journal of Geophysical Research-Atmospheres*, 110(D10301), doi:10.1029/2004jd005039. J

- Liebmann, B., and C. A. Smith (1996), Description of a complete (interpolated) outgoing longwave radiation dataset, *Bull. Amer. Meteorol. Soc.*, 77(6), 1275–1277. J
- Lin, X., M. Trainer, and S. C. Liu (1988), On the nonlinearity of tropospheric ozone production, *J. Geophys. Res.*, 93, 15879–15888. J
- Liu, H. Y., D. J. Jacob, I. Bey, and R. M. Yantosca (2001), Constraints from Pb-210 and Be-7 on wet deposition and transport in a global three-dimensional chemical tracer model driven by assimilated meteorological fields, *J. Geophys. Res.-Atmos.*, 106(D11), 12109–12128. J
- Liu, S. C., M. Trainer, F. C. Fehsenfeld, D. D. Parrish, E. J. Williams, D. W. Fahey, G. Huebler, and P. C. Murphy (1987), Ozone production in the rural troposphere and the implications for regional and global ozone distributions, *J. Geophys. Res.*, 92(4), 4191–4207. J
- Mach, D. M., H. J. Christian, R. J. Blakeslee, D. J. Boccippio, S. J. Goodman, and W. L. Boeck (2007), Performance assessment of the Optical Transient Detector and Lightning Imaging Sensor, *Journal of Geophysical Research-Atmospheres*, 112(D9), doi:10.1029/2006jd007787. J
- Martini, M., D. J. Allen, K. E. Pickering, G. L. Stenchikov, A. Richter, E. J. Hyer, and C. P. Loughner (2011), The impact of North American anthropogenic emissions and lightning on long-range transport of trace gases and their export from the continent during summers 2002 and 2004, *J. Geophys. Res.*, 116, doi:201110.1029/2010JD014305. J
- McLinden, C. A., S. C. Olsen, B. Hannegan, O. Wild, M. J. Prather, and J. Sundet (2000), Stratospheric ozone in 3-D models: A simple chemistry and the cross-tropopause flux, *J. Geophys. Res. - Atmos.*, 105(D11), 14653–14665. J
- Mesinger, F. et al. (2006), North American Regional Reanalysis, *Bulletin of the American Meteorological Society*, 87(3), 343–360, doi:10.1175/BAMS-87-3-343. J
- Mickley, L. J., D. J. Jacob, B. D. Field, and D. Rind (2004), Climate response to the increase in tropospheric ozone since preindustrial times: A comparison between ozone and equivalent CO₂ forcings, *Journal of Geophysical Research-Atmospheres*, 109(D5), doi:10.1029/2003jd003653. J
- Mlawer, E. J., S. J. Taubman, P. D. Brown, M. J. Iacono, and S. A. Clough (1997), Radiative transfer for inhomogeneous atmospheres: RRTM, a validated correlated-k model for the longwave, *Journal of Geophysical Research*, 102(D14), 16663–16682, doi:10.1029/97JD00237. J

MOVES (2010), *Motor Vehicle Emission Simulator (MOVES) 2010 User Guide*, U.S. Environmental Protection Agency, Assessment and Standards Division, Office of Transportation and Air Quality, 150 pp. [online] Available from: www.epa.gov/oms/models/moves/420b09041.pdf

Nolte, C. G., A. B. Gilliland, C. Hogrefe, and L. J. Mickley (2008), Linking global to regional models to assess future climate impacts on surface ozone levels in the United States, *Journal of Geophysical Research-Atmospheres*, 113(D14), doi:10.1029/2007jd008497.

Olivier, J. G. J., and J. J. M. Berdowski (2001), Global emissions sources and sinks, in *The Climate System*, pp. 33–78, A.A. Balkema Publishers/Swets & Zeitlinger Publishers, Lisse, The Netherlands.

Olivier, J. G. J., J. A. van Aardenne, F. Dentener, L. Ganzeveld, and J. A. H. W. Peters (2005), Recent trends in global greenhouse gas emissions: regional trends and spatial distribution of key sources, in *Non-CO₂ Greenhouse Gases (NCGG-4)*, pp. 325–330, Millpress, Rotterdam.

Orville, R. E., and G. R. Huffines (2001), Cloud-to-ground lightning in the United States: NLDN results in the first decade, 1989–98, *Monthly Weather Review*, 129(5), 1179–1193.

Ott, L. E., K. E. Pickering, G. L. Stenchikov, H. Huntrieser, and U. Schumann (2007), Effects of lightning NO_x production during the 21 July European Lightning Nitrogen Oxides Project storm studied with a three-dimensional cloud-scale chemical transport model, *Journal of Geophysical Research*, 112(D5), doi:10.1029/2006JD007365.

Ott, L. E., K. E. Pickering, G. L. Stenchikov, D. J. Allen, A. J. DeCaria, B. A. Ridley, R.-F. Lin, S. Lang, and W.-K. Tao (2010), Production of lightning NO and its vertical distribution calculated from three-dimensional cloud-scale chemical transport model simulations, *J. Geophys. Res.*, 115(D4), doi:10.1029/2009JD011880.

Pacifico, F., S. P. Harrison, C. D. Jones, and S. Sitch (2009), Isoprene emissions and climate, *Atmospheric Environment*, 43(39), 6121–6135, doi:10.1016/j.atmosenv.2009.09.002.

Park, R. J., K. E. Pickering, D. J. Allen, G. L. Stenchikov, and M. S. Fox-Rabinovitz (2004a), Global simulation of tropospheric ozone using the University of Maryland Chemical Transport Model (UMD-CTM): 1. Model description and evaluation, *J. Geophys. Res.*, 109(D9).

Park, R. J., K. E. Pickering, D. J. Allen, G. L. Stenchikov, and M. S. Fox-Rabinovitz (2004b), Global simulation of tropospheric ozone using the University of Maryland Chemical Transport Model (UMD-CTM): 2. Regional transport and

- chemistry over the central United States using a stretched grid, *J. Geophys. Res.*, 109(D9). J
- Pfister, G. G., L. K. Emmons, P. G. Hess, J.-F. Lamarque, A. M. Thompson, and J. E. Yorks (2008), Analysis of the Summer 2004 ozone budget over the United States using Intercontinental Transport Experiment Ozonesonde Network Study (IONS) observations and Model of Ozone and Related Tracers (MOZART-4) simulations, *Journal of Geophysical Research*, 113(D23), doi:10.1029/2008JD010190. J
- Pfister, G. G. et al. (2011), Characterizing summertime chemical boundary conditions for airmasses entering the US West Coast, *Atmospheric Chemistry and Physics*, 11(4), 1769–1790, doi:10.5194/acp-11-1769-2011. J
- Pickering, K. E., A. M. Thompson, J. R. Scala, W. K. Tao, R. R. Dickerson, and J. Simpson (1992), Free tropospheric ozone production following entrainment of urban plumes into deep convection, *J. Geophys. Res.*, 97(16), 17985–18000. J
- Pickering, K. E., A. M. Thompson, W. K. Tao, R. B. Rood, D. P. McNamara, and A. M. Molod (1995), Vertical transport by convective clouds: Comparisons of three modeling approaches, *Geophys. Res. Lett.*, 22(9), 1089–1092. J
- Pickering, K. E., Y. S. Wang, and W. K. Tao (1998), Vertical distributions of lightning NO_x for use in regional and global chemical transport models, *J. Geophys. Res.*, 103(23), 31203–31216. J
- Ramanathan, V., R. D. Cess, E. F. Harrison, P. Minnis, B. R. barkstrom, E. Ahmad, and D. Hartmann (1989), Cloud-radiative forcing and climate: Results from the earth radiation budget experiment, *Science*, 243, 57–63. J
- Ramaswamy, V. et al. (2001), Radiative forcing of climate change, *Climate Change 2001: The Scientific Basis. Contribution of Working Group I to the Third Assessment Report of the Intergovernmental Panel on Climate Change*, (edited by J. T. Houghton et al.), pp. 349–416, Cambridge Univ. Press, Cambridge, U.K. in-B
- Reidmiller, D. R. et al. (2009), The influence of foreign vs. North American emissions on surface ozone in the US, *Atmospheric Chemistry and Physics*, 9(14), 5027–5042. J
- Ren, X. R. et al. (2008), HO_x chemistry during INTEX-A 2004: Observation, model calculation, and comparison with previous studies, *J. Geophys. Res.*, 113(D5). J
- Richter, A., J. P. Burrows, H. Nuss, C. Granier, and U. Niemeier (2005), Increase in tropospheric nitrogen dioxide over China observed from space, *Nature*, 437(7055), 129–132. J

- Ridley, B. A., J. G. Walega, J. E. Dye, and F. E. Grahek (1994), Distribution of NO, NO_x, NO_y, and O₃ to 12 km altitude during the summer monsoon season over New Mexico, *J. Geophys. Res.*, 99(12), 25519–25534. J
- Rienecker, M. M. et al. (2008), *The GEOS-5 Data Assimilation System - Documentation of Versions 5.0.1, 5.1.0, and 5.2.0*, NASA GSFC, Greenbelt, MD. J
- Rienecker, M. M. et al. (2011), MERRA: NASA's Modern-Era Retrospective Analysis for Research and Applications, *Journal of Climate*, 24(14), 3624–3648, doi:10.1175/JCLI-D-11-00015.1. J
- Roy, B., G. A. Pouliot, A. Gilliland, T. Pierce, S. Howard, P. V. Bhave, and W. W. Benjey (2007), Refining fire emissions for air quality modeling with remotely sensed fire counts: A wildfire case study, *Atmos. Environ.*, 41, 655–665. J
- Saylor, R. D., and A. F. Stein (2012), Identifying the causes of differences in ozone production from the CB05 and CBMIV chemical mechanisms, *Geoscientific Model Development*, 5(1), 257–268, doi:10.5194/gmd-5-257-2012. J
- Schumann, U., and H. Huntrieser (2007), The global lightning-induced nitrogen oxides source, *Atmospheric Chemistry and Physics*, 7(14), 3823–3907. J
- Schwab, J. J., J. B. Spicer, and K. L. Demerjian (2009), Ozone, trace gas, and particulate matter measurements at a rural site in southwestern New York state: 1995–2005, *J Air Waste Manag Assoc*, 59(3), 293–309. J
- Shephard, M. W., S. A. Clough, V. H. Payne, W. L. Smith, S. Kireev, and K. E. Cady-Pereira (2009), Performance of the line-by-line radiative transfer model (LBLRTM) for temperature and species retrievals: IASI case studies from JAIVEx, *Atmospheric Chemistry and Physics*, 9(19), 7397–7417, doi:10.5194/acp-9-7397-2009. J
- Sillman, S. (1999), The relation between ozone, NO_x and hydrocarbons in urban and polluted rural environments, *Atmospheric Environment*, 33(12), 1821–1845, doi:10.1016/S1352-2310(98)00345-8. J
- Sillman, S., J. A. Logan, and S. C. Wofsy (1990), Regional Scale Model for Ozone in the United States With Subgrid Representation of Urban and Power Plant Plumes, *Journal of Geophysical Research-Atmospheres*, 95(D5), 5731–5748. J
- Singh, H. B., W. H. Brune, J. H. Crawford, D. J. Jacob, and P. B. Russell (2006), Overview of the summer 2004 intercontinental chemical transport experiment - North America (INTEX-A), *J. Geophys. Res.*, 111(D24). J
- Singh, H. B. et al. (2007), Reactive nitrogen distribution and partitioning in the North American troposphere and lowermost stratosphere, *J. Geophys. Res.*, 112(D12). J

- SMOKE (2010), *SMOKE v2.7 User's Manual*, The Institute for the Environment, University of North Carolina, Chapel Hill, 532 pp. [online] Available from: http://www.smoke-model.org/version2.7/SMOKE_v27_manual.pdf X
- Tang, Y. H. et al. (2008), The impact of chemical lateral boundary conditions on CMAQ predictions of tropospheric ozone over the continental United States, *Environmental Fluid Mechanics*, 9(1), 43–58, doi:10.1007/s10652-008-9092-5. J
- Thompson, A. M., and R. W. Stewart (1991), Effect of Chemical-Kinetics Uncertainties on Calculated Constituents in a Tropospheric Photochemical Model, *J. Geophys. Res.*, 96(D7), 13089–13108. J
- Thompson, A. M. et al. (2007a), Intercontinental Chemical Transport Experiment Ozonesonde Network Study (IONS) 2004: 1. Summertime upper troposphere/lower stratosphere ozone over northeastern North America, *J. Geophys. Res.*, 112(D12). J
- Thompson, A. M. et al. (2007b), Intercontinental Chemical Transport Experiment Ozonesonde Network Study (IONS) 2004: 2. Tropospheric ozone budgets and variability over northeastern North America, *J. Geophys. Res.*, 112(D12). J
- Tyndall, G. S., R. A. Cox, C. Granier, R. Lesclaux, G. K. Moortgat, M. J. Pilling, A. R. Ravishankara, and T. J. Wallington (2001), Atmospheric chemistry of small organic peroxy radicals, *J. Geophys. Res.*, 106(D11), 12157–12,182, doi:10.1029/2000JD900746. J
- Wennberg, P. O. et al. (1998), Hydrogen radicals, nitrogen radicals, and the production of O₃ in the upper troposphere, *Science*, 279(5347), 49.
- van der Werf, G. R., J. T. Randerson, G. J. Collatz, and L. Giglio (2003), Carbon Emissions from fires in tropical and subtropical ecosystems, *Global Change Biol.*, 9(4), 547–562.
- van der Werf, G. R., J. T. Randerson, L. Giglio, G. J. Collatz, P. S. Kasibhatla, and A. F. Arellano Jr. (2006), Interannual variability in global biomass burning emissions from 1997 to 2004, *Atmos. Chem. Phys.*, 6, 3423–3441. J
- Wild, O., X. Zhu, and M. J. Prather (2000), Fast-j: Accurate simulation of in- and below-cloud photolysis in tropospheric chemical models, *J. Atmos. Chem.*, 37(3), 245–282, doi:10.1023/A:1006415919030. J
- Worden, H. M., K. W. Bowman, J. R. Worden, A. Eldering, and R. Beer (2008), Satellite measurements of the clear-sky greenhouse effect from tropospheric ozone, *Nature Geoscience*, doi:10.1038/ngeo182.
- Worden, H. M., K. W. Bowman, S. S. Kulawik, and A. M. Aghedo (2011), Sensitivity of outgoing longwave radiative flux to the global vertical

distribution of ozone characterized by instantaneous radiative kernels from Aura-TES, *Journal of Geophysical Research*, 116(D14), doi:10.1029/2010JD015101. ↗

Wu, S. L., B. N. Duncan, D. J. Jacob, A. M. Fiore, and O. Wild (2009), Chemical nonlinearities in relating intercontinental ozone pollution to anthropogenic emissions, *Geophysical Research Letters*, 36, doi:10.1029/2008gl036607.

Zaveri, R. A., and L. K. Peters (1999), A new lumped structure photochemical mechanism for large-scale applications, *Journal of Geophysical Research-Atmospheres*, 104(D23), 30387–30415. ↗

Zaveri, R. A., R. C. Easter, J. D. Fast, and L. K. Peters (2008), Model for Simulating Aerosol Interactions and Chemistry (MOSAIC), *Journal of Geophysical Research*, 113(D13), doi:10.1029/2007JD008782. ↗

Zel'dovich, Y. B., and Y. P. Razier (1967), *Physics of Shock Waves and High-Temperature Hydrodynamic Phenomena*, 566-571, Academic, San Diego, Calif.,.

Zhang, G. J., and N. A. McFarlane (1995), Sensitivity of climate simulations to the parameterization of cumulus convection in the Canadian Climate Centre general circulation model, *Atmos. & Ocean*, 33, 407–446.

Zhang, R., T. Xuexi, and D. Bond (2003), Impacts of anthropogenic and natural NO_x sources over the U.S. on tropospheric chemistry, *PNAS*, 100(4), 1505–1509.

Zhang, Y. (2008), Online-coupled meteorology and chemistry models: history, current status, and outlook, *Atmospheric Chemistry and Physics*, 8(11), 2895–2932. ↗